DEVELOPMENT OF $Mg_xZn_{1-x}O$-GROWN MOCVD FOR UV PHOTONIC APPLICATIONS

KHAROUNA TALLA

Submitted in fulfilment of the requirements

for the degree of

PHILOSOPHIAE DOCTOR

In the Faculty of Science at the

Nelson Mandela Metropolitan University

(NMMU)

January 2011

Promoter: Professor J. R. Botha

Co-promoter: Professor M. C. Wagener

Acknowledgements

I would like to thank:

My promoter, Prof J. R. Botha for his support, enthusiasm, inspiration, guidance and the opportunity to work in his group

My co-promoter, Prof A. C. Wagener for his guidance throughout this study

Prof A. C. Beye at UCAD for his support and for opening the door to this great journey

Prof J. Weber at the TU Dresden, for allowing me to use the PL setup in his group

The National Research Foundation (NRF) and the Nelson Mandela Metropolitan University (NMMU) for financial assistance

The members of the Physics Department for measurements, friendly support, constructive criticism and helpful discussions

Ms. J. Ferreira and Ms. L. Kritzinger for their administrative assistance

Mr William Goossen and Dr. Jaco Olivier for SEM and TEM measurements

Messrs Len Compton, Dan O'Connor (rest in peace), Johan Wessels and Christopher Matshobongwana for their technical assistance and help with maintenance of the equipment used in this study

My "brother" J. K. Dangbegnon and his wife O. R. L. Coffi, for their great support throughout this journey

My fellow graduate students Nashwa Eassa, Zelalem Urgessa, Megersa Shura, S. Miya, D. Murape, M. Godbole and others, whose names are too numerous to mention, who have been generous with their time, knowledge and friendship

A. L. A. Ndri for her endless patience and continuous support

My friends Thierno Birahim Diokhané, Cheikh Wade, Cheikh Tidiane Thiam, Fatoumata Ndiaye and Serigne Fallou Niang

My parents (Talla family) for their interest and encouragement throughout my education

Abstract

$Mg_xZn_{1-x}O$ has emerged as a material of great technological importance. Having a direct energy band gap that is tunable throughout much of the ultraviolet (UV) region of the spectrum from the near-UV (~370 nm) to the deep-UV (~176 nm), this compound is of interest for a variety of optoelectronic devices operating in this part of the electromagnetic spectrum. $Mg_xZn_{1-x}O$ offers advantages over the more mature compound semiconductor AlGaN which stem mainly from the unusually high exciton binding energy (60 meV in ZnO).

In this study the growth of ZnO and $Mg_xZn_{1-x}O$ thin films using metal organic chemical vapour deposition (MOCVD) is systematically investigated. The films are mainly grown on c-Al_2O_3 and Si (100) and characterized using various techniques, such as photoluminescence (PL), x-ray diffraction (XRD), scanning electron microscopy (SEM), transmission electron microscopy (TEM) and auger electron spectroscopy (AES). The optical and the structural properties are essentially inspected in order to improve their quality.

In this thesis the optimisation of ZnO grown using oxygen gas as a new oxidant in our reactor is investigated. The growth temperature and VI/II ratio are varied in order to find optimum parameters giving high quality layers. The effects of Si (100), Si (111), c- and r-sapphire, glass, GaAs and ZnO substrates on the optical, structural and morphological properties of ZnO thin films grown with tert-butanol (TBOH) is examined. Similar morphologies are observed for all substrates, with the films comprising hexagonal columns having cone shaped ends. The photoluminescence spectra are similar, but the various transitions have different relative intensities. It is clear that the different substrates influence neither the orientation of the films, nor the surface morphology, significantly. The photoluminescence hints at larger stacking fault densities in films grown on silicon and glass, however, as evidenced by stronger basal plane stacking fault-related luminescence at ~3.319 eV in the relevant low temperature photoluminescence spectra.

The morphology changes with Mg incorporation, from hexagonal columnar structures to cubic faceted columns. From PL, the full with at half maximum is found to gradually increase with Mg content due to alloy broadening. The deep level emission (DLE) is observed to shift with Mg content. By changing the Mg content, the band gap of $Mg_xZn_{1-x}O$ film is tuned by ~450 meV, which provides an excellent opportunity for band gap engineering for optoelectronic applications. The c-lattice constant of ZnO (5.205 Å) decreases by only 0.6% when the Mg content reaches x=0.39. The introduction of Mg into ZnO is shown to increase

the relative PL intensity of stacking fault-related transitions (at 3.314 eV for ZnO). This becomes the dominant near band edge emission. Using TEM a thin Mg rich layer is observed at the interface between the film and the Si or Al_2O_3.

Temperature dependent PL measurements on layers with low Mg concentration (x=0.05 and 0.1) show that the main bound exciton peak exhibits an "s-shaped" temperature dependence, characteristic of localization in a disordered alloy. The origin of the PL line broadening of $Mg_xZn_{1-x}O$ ($x \leq 0.04$) is also analyzed with respect to alloy broadening, taking into account a random cation distribution and alloy clustering.

The influence of various MOCVD growth parameters such as growth temperature and VI/II ratio is studied. Varying the temperature from 280 ˚C to 580 ˚C reveals strong morphological changes and optical degradation of the films. Low (<280 ˚C) and high (>580 ˚C) growth temperatures reduce the Mg incorporation. High VI/II ratios also decrease the Mg incorporation, as evidenced by the red-shift of the donor bound exciton (D°X) line. This is ascribed to a stronger premature reaction between $(MeCp)_2Mg$ and the oxidant or a preferential heterogeneous interaction between the Mg and oxygen species on the growth front. For both oxidizing agents (O_2 and TBOH), the growth at 420 ˚C and a VI-II ratio of 60 on c-Al_2O_3 gave optimal quality layers in terms of their optical and structural quality.

A comparison of films grown using TBOH and O_2 gas as oxidizing agent shows no major difference in terms of Mg incorporation. The effect of annealing, the inclusion of a buffer layer and the influence of growth rate on the properties $Mg_xZn_{1-x}O$ thin films are also reported.

Table of contents

List of figures

List of tables

Chapter 1 Introduction

For decades, zinc oxide (ZnO) has been studied and developed for various optoelectronic and photonic applications. This group II-VI semiconductor has several favourable properties: good transparency (about 90% in the visible range), a high electron mobility (1000–1200 $cm^2V^{-1}s^{-1}$), good thermal conductivity (0.54 $Wcm^{-1}K^{-1}$ compared with 0.5 $Wcm^{-1}K^{-1}$ for GaAs), a wide band gap (3.37 eV compared to 2.70 eV for ZnSe), and strong room temperature (RT) luminescence [1] compared to III-V semiconductors. Investigations of the properties of ZnO began around 1950-1960 [2], but the real interest in this material started around 1990, following the huge demand for optoelectronic devices. A ZnO transparent thin film transistor is another recent and important development in the emerging field of transparent electronics. One of the important advantages of ZnO is the large excitonic binding energy of 60 meV [3], two times larger than that of GaN and three times that of ZnSe, which renders the free excitonic transition still stable at RT. This is one of its key properties that enable its application for UV laser diodes and other exciton-related light emitting devices operating at RT [4]. Besides the above-mentioned properties of ZnO, there are additional properties, which make it preferable over other wide band gap materials: its high energy radiation stability and amenability to wet chemical etching, for example [5]. In addition to its large excitonic binding energy, one can also add its high melting point (2248 K) and large shear modulus (the shear modulus of ZnO has been found to be ~45.5 GPa). By comparison, the shear modulus of ZnSe is 18.35 GPa, that of GaAs 32.60 GPa, and that of Si 51.37 GPa), large cohesive energy and hardness are advantages that make ZnO useful for applications other than optoelectronic, such as vulcanisation activator in the rubber industry, as a flux in the ceramics industry, for the desulphuration of gases in the chemical industry, the fabrication of stearates, phosphates, etc. [6].

Most of the recent interest in ZnO has been focused on its potential for UV-blue light emitting devices (LED) and UV-blue lasers [7]. Kalinina *et al.* [8] demonstrated for the first time, using hydride vapour phase epitaxy (HVPE), bright ultraviolet light emitting diodes based on *n*-ZnO/*p*-$Al_{0.12}Ga_{0.88}N$ heterojunctions. They observed diode-like, rectifying I-V characteristics, with a turn-on voltage of ~3.2 V and a low reverse leakage current of $\sim 10^{-7}$ A at RT. Furthermore, Alivov *et al.* [9] have reported on the growth, processing, and fabrication of n-ZnO/ *p*-GaN heterojunction LED devices, where the 1 μm thick CVD-grown n-ZnO (Ga-doped) and the MBE-grown *p*-GaN (Mg-doped) layers had carrier concentrations of

$\sim 4.5 \times 10^{18}$cm^{-3}and $\sim 3 \times 10^{17}$ cm^{-3}, respectively. These results show that ZnO is a good candidate for fabricating efficient heterostructure LEDs.

In order to extend ZnO applications, one needs to engineer the band gap. It can be alloyed with BeO [10-12], CdO [13] and MgO [14, 15] to form $Be_xZn_{1-x}O$, $Cd_xZn_{1-x}O$ and $Mg_xZn_{1-x}O$, respectively. The energy gap $E_g(x)$ of a ternary semiconductor $A_xZn_{1-x}O$ (where A=Mg, Be or Cd) is determined by the following empirical equation [16]:

$$E_g(x) = (1-x)E_{ZnO} + xE_{AO} + bx(1-x) \qquad (1.1)$$

where b is the bowing parameter and E_{AO} and E_{ZnO} are the band gap energies of compounds AO (MgO, CdO, and BeO) and ZnO, respectively. Although each of these ternary semiconductors has useful applications, they show some limitations (difficulties) during growth and device fabrication. For $Be_xZn_{1-x}O$, although its band gap can be modulated from 3.37 eV to 10.8 eV without any phase segregation (because BeO and ZnO have the same structure [17]), it is quite complicated to engineer the $Be_xZn_{1-x}O$ safely due to the toxicity of beryllium [18]. Furthermore, $Be_xZn_{1-x}O$ shows a large band gap bowing parameter. Also, the difference in ionic radius of Zn (0.60 Å) and Be (0.27 Å) will generate a large lattice mismatch between $Be_xZn_{1-x}O$ and ZnO when heterostructures are needed [19]. For $Cd_xZn_{1-x}O$, the band gap is shifted to lower energies (compared to ZnO) with increasing incorporation of Cd. Due to the similar ionic radius of Cd^{2+} (0.74 Å) and Zn^{2+} (0.60), the lattice constants *a* and *c* of $Cd_xZn_{1-x}O$ do not change significantly compared to those of ZnO. This material is therefore a suitable candidate for optoelectronic devices operating in the visible spectral range, since the band gap can be decreased, in principle, from 3.37 eV to 2.0 eV [20]. With increasing Cd mole fraction up to 7%, $Cd_xZn_{1-x}O$ ($x \leq 0.07$), the band-gap decreases from 3.3 eV to 3.0 eV [21]. For higher Cd content (~8%), segregation of CdO (cubic structure) is observed due to the difference in crystal structure.

The incorporation of Mg into ZnO has been found to widen the band gap. In principle, the band gap of $Mg_xZn_{1-x}O$ can be tuned from 3.37 eV to 7.8 eV by varying the Mg mole fraction in the range $0 \leq x \leq 1$ [22]. Indeed, $Mg_xZn_{1-x}O$ is one of the most promising barrier materials for ZnO-based heterostructures, providing both carrier and optical confinement [23]. Furthermore, the modulation of the band gap in the ternary alloy allows the fabrication of superlattice heterostructures with low lattice mismatch such as $ZnO/Cd_xZn_{1-x}O/ZnO$ [24], $Mg_xZn_{1-x}O/Cd_xZn_{1-x}O/Mg_xZn_{1-x}O$ and $Mg_xZn_{1-x}O/ZnO/Mg_xZn_{1-x}O$ [25]. Due to the

piezoelectric effect, superlattices and quantum wells will, however, have strong internal electric fields if grown on polar surfaces [26]. $Mg_xZn_{1-x}O$ alloys may also be considered as suitable insulating spacers in magnetoelectronic devices, in particular, in magnetic tunnel junctions [27]. There are huge obstacles to growing $Mg_xZn_{1-x}O$, however. From the phase diagram of the ZnO–MgO system, the thermodynamic solid solubility of MgO in ZnO is less than 4 mol% [28]. This low solubility causes phase segregation, which affects the crystal quality as well as the optical quality of the films. The main complication in the application of ternary alloys is the nearly linear relationship between the lattice constant and the band gap, which imposes constraints upon the choice of material combinations, since it is notoriously difficult to grow high quality layers of lattice mismatched semiconductors [29].

ZnO and related alloys suffer from a lack of reproducible and low-resistivity *p*-type material, which hamper their application in optoelectronic devices. Notwithstanding all the methods and dopants (N, P, As and Sb) tried to date, the difficulty remains. This difficulty can arise from a variety of causes. Dopants may be compensated by low energy native defects, such as Zn_i or V_o [30]. Low solubility of the dopant in the host material is another possibility. Deep impurity levels can also be a source of the doping problem, causing significant resistance to the formation of shallow acceptors.

The growth of ZnO and its alloys has been demonstrated using many techniques, such as metal organic chemical vapour deposition (MOCVD) [31], pulsed laser deposition (PLD) [32], RF-magnetron sputtering [33], spray pyrolysis [34], ion-beam assisted deposition [35], sol-gel method [36], molecular beam epitaxy (MBE) [37], oxidation of metallic zinc [38] and atomic layer deposition [39]. Among these techniques, MOCVD is attractive for achieving devices on a commercial scale since high deposition rates and high quality layers are possible, in particular at low pressure. MOCVD is a technique suitable for the growth and doping of ZnO, as it is established to offer high quality layers.

The growth of $Mg_xZn_{1-x}O$ was demonstrated first by Ohtomo *et al.* [15] in 1998, using MBE at a growth temperature at 550 ˚C. They varied the band gap from 3.36 eV (x=0) to 3.87 eV (x=0.33). They successfully fabricated ZnO/$Mg_{0.20}Zn_{0.80}O$ superlattices. In 1999, Sharma *et al.* [40], using PLD at 700-750 ˚C, produced high quality, epitaxial single crystal $Mg_xZn_{1-x}O$ films with very strong UV photoluminescence at RT. They were able to vary the band gap from 3.3 eV to 4.0 eV by adjusting the Mg content. The preparation of $Mg_xZn_{1-x}O$ by RF-magnetron sputtering was reported in 2000 [41]. Two sources, ZnO and MgO were used

and phase segregation was demonstrated at x=0.58. A band gap value of 4.20 eV for x=0.46 with the crystallographic structure of ZnO, was reported. From these results, it was concluded that the application of $Mg_xZn_{1-x}O$ as a window layer in solar cells can improve their performance. Makino *et al.* [21], in 2006, fabricated ZnO/(Mg,Zn)O multiple quantum wells on lattice-matched $ScAlMgO_4$ substrates by laser molecular beam epitaxy (LMBE). They also reported RT optically stimulated emission in ZnO/$Mg_{0.12}Zn_{0.88}O$ multi-quantum well heterostructures and measured thresholds below 22 kW/cm^2 for well widths in the range of 7–47 Å, with a minimum of 11 kW/cm^2 for a 47 Å thick quantum well. Shukla [42] reported a ZnO/$Mg_xZn_{1-x}O$ *p-n* junction light-emitting diode employing ZnO/$Mg_{0.1}Zn_{0.9}O$ multi-quantum well active layers, fabricated on c-plane sapphire substrate by PLD, with efficient electroluminescence at RT for bias voltages ≥7 V. In 2002, Choopun *et al.* [43] realized by PLD cubic $Mg_xZn_{1-x}O/Al_2O_3$ films having band gap above 5.0 eV grown on sapphire. They obtained highly (111) oriented and single-phase films for the entire range of growth temperature from RT to 750 ˚C. The fabrication of cubic $Mg_xZn_{1-x}O$ on lattice-mismatched substrate at relatively low growth temperatures creates another opportunity for the manufacturing of optoelectronic devices. Wang *et al.* [44], using cubic $Mg_xZn_{1-x}O$, realised a solar-blind deep ultraviolet photodetector with a maximum responsivity of 396 mA/W at 10 V bias, which is almost three orders of magnitude larger than the highest value ever reported for $Mg_xZn_{1-x}O$-based photodetectors. Further, Hullavarad *et al.* [45] reported the realisation of a $Mg_xZn_{1-x}O$-based UV detector on quartz by PLD.

The aim of this study is a systematic investigation of $Mg_xZn_{1-x}O$ thin films by MOCVD. The bulk of this work emphasizes the influence of the main growth parameters (VI/II ratio, temperature, growth rate, buffer layer and annealing temperature) on the structural, morphological and optical properties. Special emphasis is placed on the photoluminescence of the grown films.

The thesis is organised as follows: In Chapter 2, basic properties of ZnO and $Mg_xZn_{1-x}O$ are presented. A detailed description of the crystal structure and the band structure of ZnO and $Mg_xZn_{1-x}O$ is given. Important bulk properties of ZnO are also discussed. Chapter 3 describes the growth technique used in this work and includes also a brief theoretical treatment of MOCVD. Chapter 4 is an introduction to the techniques used for the characterization of the $Mg_xZn_{1-x}O$ films. In Chapter 5 the influence of the two main growth parameters, i.e. the growth temperature and the VI/II molar ratio (the ratio between the oxygen and zinc precursors in the reactor), on the optical and structural properties of ZnO films grown by

MOCVD is studied. This chapter is a preamble to the growth of $Mg_xZn_{1-x}O$ using oxygen as oxidizing agent, but also an opportunity to investigate an appropriate substrate for ZnO growth and for wurtzite $Mg_xZn_{1-x}O$. Chapter 6 presents the results of the effect of Mg incorporation into ZnO on the optical and structural properties of the films. Detailed PL results are also given. Chapter 7 is a systematic study of the effect of various growth parameters (growth temperature, the effect of VI/II ratio, growth rate, annealing, and the inclusion of a buffer layer) on the optical and structural properties of $Mg_xZn_{1-x}O$. Finally in Chapter 8, a summary of the results obtained in this work and a proposed direction for future work is presented.

Chapter 2 Literature background: ZnO and $Mg_xZn_{1-x}O$

In this chapter, the basic properties of ZnO and $Mg_xZn_{1-x}O$ are presented. A detailed description of the crystal structure, the band structure and important bulk properties of ZnO and $Mg_xZn_{1-x}O$ are also given, as well as brief overviews of previous $Mg_xZn_{1-x}O$ growth studies and potential applications.

2.1 Literature on ZnO

ZnO has been the subject of intensive investigation since 1935. It continues to be intensively investigated today as shown by the activities of many research groups that are still exploring its basic properties and potential applications. Compared to other semiconductor materials like GaN, GaAs and ZnSe, ZnO has many potential applications in the ultraviolet (UV) region, which makes it very attractive in fields like physics, chemistry and biology. Its large band gap (3.37 eV at RT) and large exciton binding energy of 60 meV (much higher than that of GaN (21–25 meV)) could lead to lasing action based on excitonic recombination even above RT [46, 47]. However, GaN device technology is much more mature, as GaN-based high performance electronic and optical devices have already been demonstrated. ZnO has potential applications such as UV light emitters, transparent electrodes in solar cells and gas sensors [48]. The main obstacle to ZnO-based electronic applications is the difficulty in producing *p*-type epitaxial layers. Nitrogen doped ZnO has been tried in many research groups in an attempt to produce *p*-type ZnO [49-52], but due to the narrow processing window and low hole concentration, it has not been fully successful. In general a low acceptor impurity solubility, high acceptor ionization energies and compensation mechanisms are the three main factors that make *p*-type doping of ZnO difficult. Despite considerable effort, no reproducible high quality *p*-type layer has been reported yet.

ZnO is a II-VI compound, which has the hexagonal wurtzite structure, in which each anion is surrounded by four cations at the corners of a tetrahedron, and vice versa (Figure 2-1). The crystal has the stacking sequence …AaBbAaBb…. as compared to …AaBbCcAaBbCc…. in the diamond cubic (silicon) and sphalerite (GaAs) structures. Although ZnO can assume the zincblende and rock salt structure, both under high pressures [5], the thermodynamically stable phase is the hexagonal wurtzite structure. Based on the values of ionic radii of cation (0.6 Å) and anion (1.34 Å), the structure is relatively open. Indeed, the zinc and oxygen

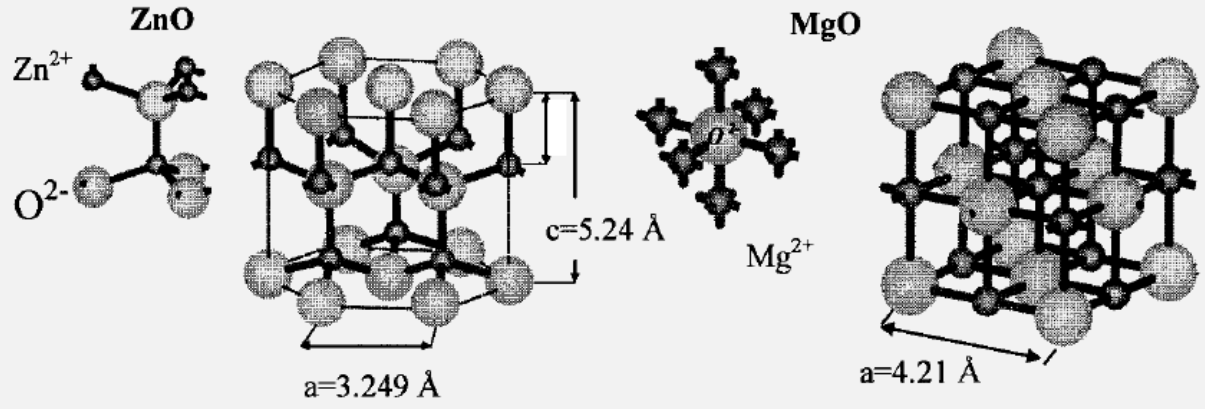

Figure 2-1 Crystal structure of hexagonal wurtzite ZnO and cubic rock salt MgO [54]

atoms occupy only 40% of the volume of the crystal, leaving empty spaces of radius of 0.95 Å. It is possible that under certain conditions, excess zinc atoms can be accommodated in these spaces to form interstitial zinc. This explains some of the peculiar properties related to the conductivity, photoconductivity, luminescence, and catalytic and chemical properties of this solid [53].

The O-Zn distance of the nearest neighbours is 1.992 Å in the direction parallel to the c-axis of the hexagonal unit cell and 1.973 Å in the other three directions of the tetrahedral arrangement [55]. The reported lattice constants range from 3.2475 Å to 3.2501 Å for the a parameter and from 5.2042 Å to 5.2075 Å for the c parameter [5, 56]. Their ratio $\frac{c}{a} \sim 1.60$ is close to the ideal value for the hexagonal cell, $\frac{c}{a} = 1.633$. Like other II-VI semiconductors, wurtzite ZnO can be transformed to the rocksalt NaCl structure at relatively modest external hydrostatic pressures. The Zn-O bond has a substantial ionic character (ionicity of f_i=0.616 on the Phillips ionicity scale [57]) which implies that the bottom of the conduction band is formed essentially of the 4s levels of Zn^{2+} and the top of the valence band of the 2p levels of O^{2-}. The gap between the conduction band and the highest valence band is around 3.437 eV at low temperatures [26]. The fact that ZnO has partial ionic bonding and lacks a center of inversion is partly responsible for the piezoelectricity of ZnO. The three coefficients of the piezoelectric tensor d_{15}, d_{31}, and d_{33} have values of –10, –5, and 12×10^{-12}m/V, respectively and are rather large [5, 26, 58].

Figure 2-2 shows the band structure of hexagonal ZnO near the Γ point of the Brillouin zone. The valence band (VB) is split by the crystal field and spin orbit interaction into three bands

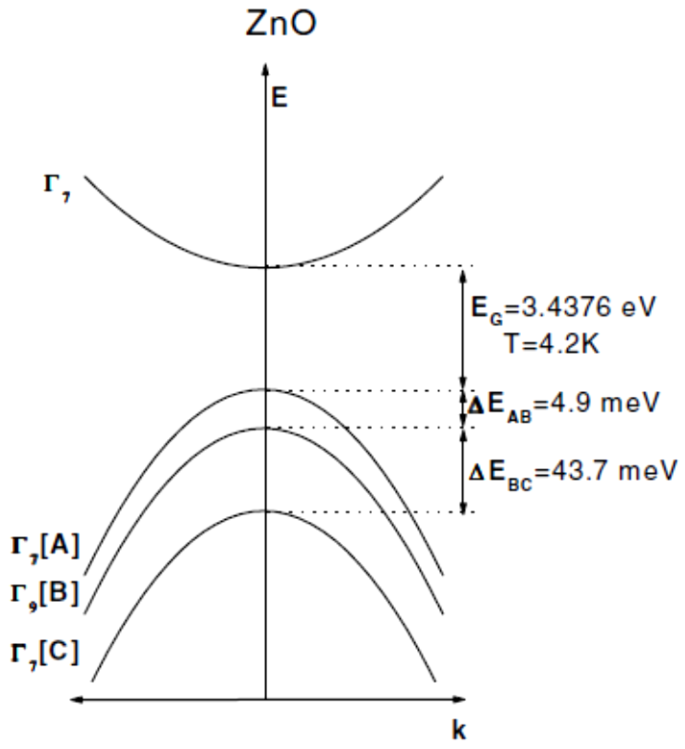

Figure 2-2 Band structure and symmetries of hexagonal ZnO. The splitting into three valence bands (A, B, C) is caused by crystal field and spin-orbit interaction [59]

named A (referred to as the heavy hole), B (referred to as the light hole) and C (referred to as the crystal-field split-off band). The lowest conduction band (CB) is formed from the empty 4s states of Zn^{2+}or the antibonding sp^3-hybrid states. The valence band maximum (VBM) originates from the occupied 2p orbitals of O^{2-} or the sp^3 bonding orbitals [26]. The lowest conduction band has two-fold degeneracy and Γ_7-symmetry. The A, B and C valence bands have symmetries Γ_7, Γ_9 and Γ_7, respectively.

The electron effective mass is $0.24m_o$ and the hole effective mass is $0.59m_o$, but these effective masses are still debated. For example, from cyclotron resonance on bulk ZnO grown by the vapour-phase reaction method, electron effective masses of $0.3m_o$ and $0.34m_o$ are obtained from Zeemann splitting measurements for $m^*_{e\perp}$ and $m^*_{e\parallel}$, respectively [60]. Also Dietz *et al.* [61] found that the effective masses of electrons and holes are $0.38m_o$ and $1.80m_o$, respectively.

The thermal expansion coefficient of a material describes the lattice deformation as a function of temperature. For ZnO, these coefficients are $\alpha_a=4.31\times10^{-6}$ K^{-1} and $\alpha_c=2.49\times10^{-6}$ K^{-1} at 300K. The mismatch caused by thermal expansion is given by $\varepsilon_{th} = (\alpha_{ZnO} - \alpha_{substrate})(T_g - 300K)$ [62] and Zhang *et al.* [63] found experimentally that

the mismatch along the a-axis is ε_{th}=0.2% at a growth temperature of *T*g=500 ˚C using sapphire as substrate. The specific heat capacity of ZnO at constant pressure is C*p*=40.3 J mol^{-1} K^{-1}.

Unintentionally doped ZnO shows *n*-type conductivity due to the presence of point defects such as oxygen vacancies (V_o) and zinc interstitials (Zn_i). The latter in particular acts as a shallow donor in ZnO with an ionisation energy of ~30±5 meV [64]. However, it has been argued that the *n*-type conductivity of unintentionally doped ZnO films is only due to hydrogen (H), which is treated as a shallow donor with activation energies of 35 meV and 42 meV [56, 65]. These two ionisation energies are due to the possible involvement of hydrogen in two shallow donor levels. Doping ZnO with group III elements (B, Al, In, Ga) leads to stable *n*-type conductivity in ZnO films [66], resulting in high-quality, highly conductive films. Doping ZnO with group IA elements (Li, Na, K) typically results in semi-insulating films, instead of the *p*-type behaviour that might be expected [67]. *P*-type ZnO may be possible with group V elements (N, P, As, Sb). Of these dopants, nitrogen (N) appears to be a good candidate as theoretical studies propose N_O to create a shallow acceptor with an estimated ionization energy of ~200 meV [49]. However, N has a very low solubility in ZnO [49]. Compared to N, substitutional P on an O site has a higher ionization energy (about 0.62 eV), which makes it difficult to achieve p-type ZnO. The origin of p-type conduction when using group V elements is likely to be defect complexes consisting of one dopant atom (P, As and Sb) and two Zn vacancies. From a simple viewpoint of chemical bonding, the substitution of O^{2-}anions in ZnO by P^{3-}, As^{3-} or Sb^{3-} should create fully ionized acceptors. However, due to the large mismatch of the ionic radii of P^{3-} (2.12 Å), As^{3-} (2.22 Å), and Sb^{3-} (2.45 Å) with the ionic radius of O^{2-} (1.38 Å), it was argued that those impurities should have a low solubility substituting for O [68]. Moreover, theory suggests that the energy levels of P, As, and Sb replacing O are located deep in the band gap of ZnO. In order to explain the *p*-type character of ZnO following As and Sb doping it was suggested that the acceptor action is actually due to As_{Zn}-$2V_{Zn}$ or Sb_{Zn}-$2V_{Zn}$ complexes, where an As or Sb atom occupies a Zn site and is decorated with two Zn vacancies [69, 70].

There is a huge interest in the green band emission in ZnO, which can be traced back to the 1990's. Unfortunately, the mechanisms responsible for this emission band are still unclear. The green emission band was first attributed to an excess of zinc [71]. Almost all the proposed mechanisms about the green emission involve native lattice defects, except one which is based on divalent Cu impurities. These models can be listed as follows [72]:

- ✓ Zn-excess related transitions ($Zn^{+}$to Zn^{2+});

- ✓ Oxygen vacancies (V_o);
- ✓ Transitions at Cu^{2+}
- ✓ Zn interstitial to Zn vacancy ($Zn_i$to V_{Zn});
- ✓ Singly ionized oxygen vacancies (transitions from $V_o^+$to VB);
- ✓ Transitions from shallow traps to doubly-ionized oxygen vacancies (V_o^{++});
- ✓ DA pair (V_o^+ to V_{Zn});

Thin films have been grown by various techniques as mentioned in the introduction. Each of these methods offers various advantages over the others, albeit cost, speed, film quality or scalability. For this reason, no single method of growth should be disqualified. Each growth technique has been reviewed by authors like Ozgur *et al.* [5], Triboulet *et al*. [66], Klingshirn [26], Janotti *et al.* [56], etc. The main techniques used for the growth of ZnO thin films are PLD, MBE and MOCVD. However, MOVCD has given the best homoepitaxial layers to date. The interest in MOCVD is primarily from an industrial point of view for large-scale production [66], and the technology for ZnO growth is strongly driven by the choice of precursors, their availability, and the growth rates that can be achieved.

ZnO is a versatile functional material that has a diverse group of growth morphologies. A variety of ZnO nanostructures including nanowires, nanoneedles, nanorods, nanohelices, and nanobelts have been synthesized [73]. A large amount of ZnO is used in the rubber and concrete industries [6]. There are several other applications of ZnO based on its excellent piezoelectric properties. Some examples are surface-acoustic wave (SAW) devices and piezoelectric sensors, transducers and actuators [73]. A field-effect transistor based on zinc oxide has been reported, opening the opportunity to design microelectronic devices that are transparent and/or work at high temperatures [74]. Optically pumped lasing has also been reported in ZnO [6].

To enhance the versatility as an optoelectronic compound of ZnO, band gap engineering is a key issue. The ternary system CdO-ZnO-MgO {from 2.0 eV (CdO) to 7.8 eV (MgO)} covers a larger band gap range than the nitrides {from 1.9 eV (InN) to 3.4 eV (GaN), to 6.2 eV (AlN)} with a much smaller lattice constant variation [75].

2.2 Literature on $Mg_xZn_{1-x}O$

In recent years several papers on $Mg_xZn_{1-x}O$ have been published by various groups, using different growth techniques to synthesize thin films. These reports focus on the effect of Mg

incorporation on the optical properties, the phase evolution from hexagonal-phase to cubic-phase upon an increase in the Mg concentration, the thermal stability of $Mg_xZn_{1-x}O$ films, the fabrication of $ZnO/Mg_xZn_{1-x}O$ heterostructures like quantum wells or superlattices and the application of $Mg_xZn_{1-x}O$ in optoelectronic devices. Many growth techniques such as PLD [15], MOCVD, MBE [76], RF magnetron sputtering [77], reactive electron evaporation deposition (REBED) [78], etc, have been used to grow and fabricate high quality thin films, $Mg_xZn_{1-x}O/ZnO$ quantum wells and other heterostructures.

From the phase diagram of the ZnO-MgO binary system (Figure 2-3), the thermodynamic solid solubility of MgO in ZnO is less than 8 mol.% at 1000 ˚C [79]. But there are different values reported for the solubility limit of MgO in ZnO. For example, Segnit *et al.* [80] reported that the solubility of ZnO in MgO is 39 mol.% at 1600 ˚C, while Kondrashev *et al*. [81] reported solubility limits for ZnO in MgO and MgO in ZnO at 1100 ˚C as 25.5 mol.% and 12 mol.%, respectively. Kenny *et al.* [82] derived the activity-composition relation in the MgO-ZnO system from the direction of the conjugation lines between oxide and spinel phases in the ternary system $ZnO-MgO-Al_2O_3$, at 1205 ˚C in air, assuming that the spinel phase behaves ideally. These authors reported the solubility of ZnO in MgO and MgO in ZnO as 29 mol.% and 3 mol.%, respectively, at 1205 ˚C [80-83]. Ohtomo *et al.* [15] have reported the solid solubility of MgO in ZnO to be 33 mol.% for thin films grown under metastable conditions. It is clear that non-equilibrium growth enhances the solubility limit.

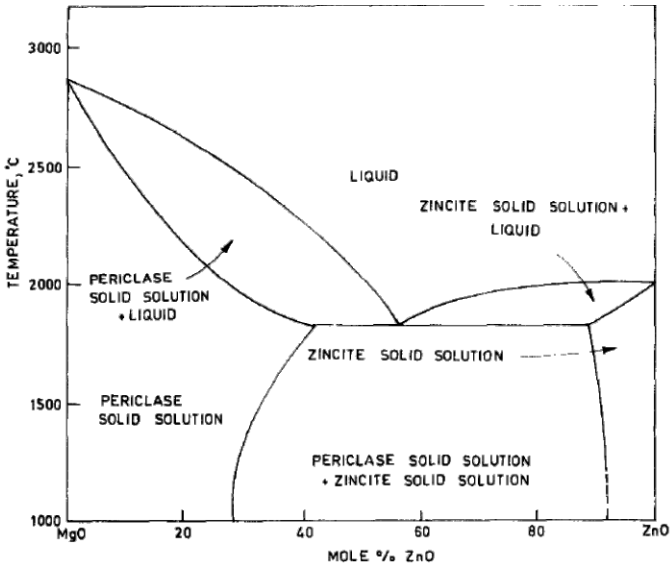

Figure 2-3 Phase diagram of the ZnO-MgO system [79]

$Mg_xZn_{1-x}O$ films have been grown on different types of substrates such as silicon [84], quartz [85], sapphire [86], ZnO [87], $ScAlMgO_4$ [21] and MgO [88]. Sapphire substrate is most commonly used for $Mg_xZn_{1-x}O$ films, despite the large lattice mismatch (~18%) with ZnO. Some researchers justify the growth of $Mg_xZn_{1-x}O$ on sapphire in terms of the low energy oxide–oxide interface between the substrate and the film [89].

Since the crystal structures of ZnO and MgO are wurtzite (hexagonal, $a = 3.24$ Å and $c = 5.20$ Å) and NaCl-type (cubic, $a = 4.24$ Å), respectively, and the ionic radius of Zn^{2+} (0.60 Å) is quite close to Mg^{2+} (0.57 Å), alloying ZnO with MgO can result in the structure evolving from the hexagonal-phase to the cubic-phase. In addition, an increase in the band gap energy from 3.3 eV to 7.7 eV is expected. It should be pointed out that there is a lack of information in literature for $Mg_xZn_{1-x}O$ on the variation in physical parameters as a function of Mg mole fraction.

MgO belongs to the space group Fm3m and crystallizes in the cubic rocksalt structure (Figure 2-1). Each atom is six-fold coordinated with the Mg-O distance being 2.107 Å. The lattice consists of interpenetrating face centered cubic lattices, separated along the unit cell edge by $u = 0.5$ (fractional coordinates) [90]. While oxygen (by convention) occupies the (0,0,0) and (0.5,0.5,0) positions, magnesium occupies the (0,0,0.5) and (0.5,0.5,0.5) positions. When the wurtzite lattice is relaxed, c/a = 1.204 and u = 0.5. This implies that the Mg and O atoms lie in the same plane. Zn^{2+} ions are very close to the tetrahedral coordinated and octahedral coordinated Mg^{2+} ions. The Mg atom was found to substitute the Zn atom in tetrahedral coordination leading to distortion of the wurtzite ZnO lattice in the $Mg_xZn_{1-x}O$ films [91]. The resulting c/a ratio decreases with increasing x, indicating that hexagonal $Mg_xZn_{1-x}O$ is considerably distorted from the ideal wurtzite structure. The introduction of Mg increases the ionic character of $Mg_xZn_{1-x}O$. Furthermore, Chiou *et al.* [92] reported a Mg-induced enhancement of the localization of O 2*p* and Zn 3*d* states.

It seems impossible to grow single phase $Mg_xZn_{1-x}O$ spanning the entire range of composition (x=0 to x=1), irrespective of the substrate or growth technique. The Mg content at which phase segregation is reported, varies considerably, which is presumably related to the growth technique and growth parameters and to some extent to the substrate. Park *et al.* [93] obtained stable hexagonal $Mg_xZn_{1-x}O$ films up to a limit of 49 mol.% and attributed the extended solubility range to the low growth temperature conditions employed for their MOCVD grown films. Moreover, from other techniques, Minemoto *et al.* [94] reported a

solubility limit of 46 mol% for $Mg_xZn_{1-x}O$ films prepared by co-sputtered ZnO and MgO targets. Using radio frequency magnetron sputtering, the same group observed phase separation only at x=0.58. In addition to the growth technique, the growth temperature also plays a great role. Sharma *et al.* [40] reported the solubility of MgO in ZnO to be 36 wt% using PLD at a substrate temperature of 700–750 ˚C. At higher substrate temperatures over 700 ˚C, the desorption rate of Zn from the substrate surface is much higher than that of Mg due to differences in the vapour pressure of Mg and Zn, which results in Mg rich films with a larger band gap, caused by the rapid formation of the cubic phase. Phase segregation is noticed to deteriorate the quality of the films. It causes the absorption edge to red-shift [95] and the band gap is not well defined.

From $Mg_xZn_{1-x}O$ films grown using PLD, Ohtomo *et al.* [15] has experimentally determined the band gap at RT to vary linearly with Mg mole fraction up to 4.15 eV (for x=0.36). Wu *et al.* [96], using MOCVD, obtained RT band gap (E_g) values of $Mg_xZn_{1-x}O$ films of 3.34 eV, 3.40 eV, 3.51 eV, 3.58 eV, and 3.64 eV for Mg mole fractions of x=0, 0.01, 0.06, 0.10, and 0.14, respectively. Jin *et al.* [97] reported the exciton energy gap of the A-exciton, B-exciton, and C-exciton as a function of magnesium concentration extracted from absorption spectra at RT:

$$\text{A exciton: } E_g = 3.403 + 1.120 \times 10^{-2}x + 3.393 \times 10^{-4}x^2 \quad (2.1)$$

$$\text{B exciton: } E_g = 3.452 + 1.174 \times 10^{-2}x + 3.523 \times 10^{-4}x^2 \quad (2.2)$$

$$\text{C exciton: } E_g = 3.549 + 1.379 \times 10^{-2}x + 3.160 \times 10^{-4}x^2 \quad (2.3)$$

The increase in the band gap with increasing Mg content is due to an increase in the energy of the conduction-band minimum (E_c) and a decrease in the energy of the valence-band maximum (E_v), namely:

$$\Delta Eg = \Delta E_c - \Delta E_v, \ \Delta E_c > 0 \ and \ \Delta E_v < 0. \quad (2.4)$$

Thus, the ionization energies of both donors and acceptors increase with increasing band gap of $Mg_xZn_{1-x}O$. However, the increase in the ionization energy of the donor is expected to be much larger than that of the acceptor, because the conduction-band change is much larger than the valence-band change ($\Delta Ec \ / \Delta Ev = 9/1$) [98].

Like ZnO, *n*-type $Mg_xZn_{1-x}O$ with high crystal quality can be achieved. However, like in most wide band gap II-VI semiconductor materials, $Mg_xZn_{1-x}O$ is difficult to be doped *p*-

type. Many growth experiments have been reported on p-type $Mg_xZn_{1-x}O$: Heo *et al.* [99] reported *p*-type $Mg_xZn_{1-x}O$ by PLD, using a substrate temperature between 550 ˚C and 650 ˚C and using phosphor as dopant; Zhang *et al*. [100] fabricated *p*-type $Mg_xZn_{1-x}O$ by N–Al co-doping during ultrasonic spray pyrolysis at 400 ˚C and Gai *et al.* [101] realized N-doped *p*-type $Mg_xZn_{1-x}O$ by post-growth annealing of plasma-assisted molecular beam epitaxial (PAMBE) films. The understanding of the behaviour of acceptors in $Mg_xZn_{1-x}O$ is still unclear. Wei *et al*. [102] realized as-grown *n*-type $Mg_xZn_{1-x}O$:N produced by PAMBE, which converted to *p*-type with a resistivity of 1.60 Ωcm, a carrier concentration of 6.1×10^{17} cm^{-3}, and a mobility of 6.42 cm^2/V.s, after annealing at 600 ˚C in flowing O_2. Due to strong interaction between Mg and H the compensating effect of H will naturally be a major concern in fabricating *p*-type material [96].

$Mg_xZn_{1-x}O$ has been used in fabricating optoelectronic devices. For example, heterostructures consisting of $Mg_xZn_{1-x}O$ and ZnO are very suitable for resonant tunnelling devices. In addition, using wide band gap cubic $Mg_{0.55}Zn_{0.45}O$ thin films as insulators, metal-insulator-silicon (MIS) devices have been fabricated by Wu *et al.* [103]. Due to its lower optical absorption and adjustable refractive index, $Mg_xZn_{1-x}O$ films also have potential applications in integrated optical and optical wave-guide devices.

Chapter 3 MOCVD: growth system and process

This chapter describes the experimental procedures and conditions used during MOCVD deposition of the ZnO and $Mg_xZn_{1-x}O$ films. A summary of the theory of MOCVD is also included. The first section presents the theory involved in the MOCVD process and details of the precursors used in this work, such as their efficiency, their chemical properties and some illustrative results obtained during this study. The second part focuses on the MOCVD growth procedure and a description of system.

3.1 MOCVD theory

MOCVD was demonstrated by Manasevit in 1968 for the growth of GaAs [104]. Since then this technique has become widely used and has been steadily develop and improved, especially in terms of reactor design, gas delivery and control. Over the years, MOCVD has been used to develop a variety of high quality semiconductor materials including:

- ✓ GaAs-based material for optoelectronic devices operating from the near-IR (~980 nm) to the visible yellow-green (~570 nm) region.
- ✓ InP-based material used in photonic and high speed electronic devices [105].
- ✓ GaSb-based material for photonic devices operating in the mid-wavelength IR spectral region (λ>3 μm).
- ✓ GaN-based material for photonic device applications from visible-green (λ~540 nm with InGaN) to deep-UV (λ~280 nm with AlGaN).

The ability to produce a variety of high quality III-V and II-VI compounds makes MOCVD one of the most complete growth techniques for semiconductor production. Furthermore, this technique does not require high vacuum and it is easily serviceable with larger throughput. In other words, it yields a high growth rate, superior growth efficiency and large-area uniformity, while in-situ doping is also possible [106]. However, the MOCVD growth process is highly complex. Stringfellow [107] has described in detailed the various processes involved in MOCVD. MOCVD is a synthesis process in which chemicals react in the vapour phase near or on a heated substrate to form a solid. This process engages three main domains of physics: thermodynamics, kinetics and hydrodynamics. In addition to these, chemistry forms a significant part of the process and must be taken into account.

Thermodynamics determines the driving force for the overall growth and hydrodynamics controls the rate of transport of material to the growing solid/vapour interface [107]. Thermodynamics indicates the direction of the reaction. This is determined by the change in Gibbs free energy, given by:

$$\Delta G = \Delta H - T\Delta S \qquad (3.1)$$

where ΔH is the enthalpy change, ΔS is the entropy change during the chemical reaction and T is the absolute temperature. If the free energy change is positive for a reaction, net work must be put into the system to affect the reaction, otherwise the reaction cannot take place. The nucleation process of ZnO and $Mg_xZn_{1-x}O$ films is also governed by the Gibbs free energy.

Kinetics tells about the rate at which the reaction occurs. Hydrodynamics in MOCVD depends strongly on the reactor geometry/configuration and also on the total reactor pressure. All these aspects have been intensively treated in reference [107].

MOCVD source materials are generally highly toxic and flammable, requiring great care in the system design and during processing. For the growth of high quality layers, suitable metalorganic precursors are required. For the growth of ZnO and $Mg_xZn_{1-x}O$, diethylzinc, bis-(methylcyclopentadienyl)-magnesium, oxygen and tertiary butanol have been largely used as they have been identified to give superior quality material [108-111].

3.1.1 Precursor chemistry

In MOCVD growth, the choice of precursors is very important. The main problem is to find a combination of precursors so that the chemical reactions only take place at or on the substrate surface. It is important to consider the premature reactions taking place between different precursors, since these affect considerably the growth rate and most importantly, the quality of the layer. The main criteria for the choice of a precursor in MOCVD could be summarized as follows [112]:

- ✓ Saturated vapour pressure in the range of 1–10 mbar in the temperature range 0-20 ˚C
- ✓ A good thermal stability during its evaporation and transport in the gas phase
- ✓ Efficient reaction at the desired growth temperature

- ✓ The precursors should decompose cleanly on pyrolysis without contamination of the growing film (e.g. by carbon). Furthermore, the by-products from the reaction should be non-toxic and non-pyrophoric (to minimize fire hazard). The precursors should also be readily available in consistent quality and quantities at low cost, in liquid rather than gas or solid form and stable in containers over a long period, since their rate of consumption is rather low.

Taking into account all these factors, diethylzinc and bis-(methylcyclopentadienyl)-magnesium have been studied as group II and oxygen gas and tertiary butanol as group VI precursors.

Group II precursors

Zinc and magnesium are very important elements in the fabrication of II-IV wide band gap devices. They have been used in MOCVD [66], molecular beam epitaxy (MBE) [15] and atomic layer deposition (ALD) [113, 114] to grow ternary and quaternary semiconductor materials such as $Zn_{1-x}Mg_xSe$ [115], $Mg_xZn_{1-x}O$ [14] and $Zn_{1-x}Mg_xSe_yTe_{1-y}$ [116]. Diethylzinc and bis-(methylcyclopentadienyl)-magnesium are the main sources utilized for the growth of these II-VI semiconductors in general, and in particular, for $Mg_xZn_{1-x}O$. Nevertheless, there is a variety of other Zn and Mg sources that are currently used for ZnO and $Mg_xZn_{1-x}O$ growth, such as zinc propionate ($Zn(C_3H_5O_2)_2$) [117], dimethylzinc ($Zn(CH_3)_2$) [118], zinc acetate ($Zn(CH_3COO)_2$) [119], (bis-cyclopentadienyl)-magnesium (Cp_2Mg) [120], and bis-(ethylcyclopentadienyl)-magnesium ($EtCp_2Mg$) [121].

Diethylzinc (DEZn) [$(C_2H_5)_2Zn$]

DEZn remains the most widely used precursor for ZnO and $Mg_xZn_{1-x}O$ growth [66]. A comparative study of diethylzinc and dimethylzinc for the growth of ZnO has shown that DEZn is the superior zinc source for the MOCVD growth of ZnO for the experimental conditions used in our reactor (~380℃, ~250 Torr) [122]. Growth using DEZn not only introduces less H and C, but also gives better crystal structure and optical quality for specific growth parameters. Based on these studies and from previous experience in our research group [49, 123], DEZn was also used in the present study. DEZn has not only been used in MOCVD but also in other techniques such as ALD [114], and metal organic molecular beam epitaxy [124].

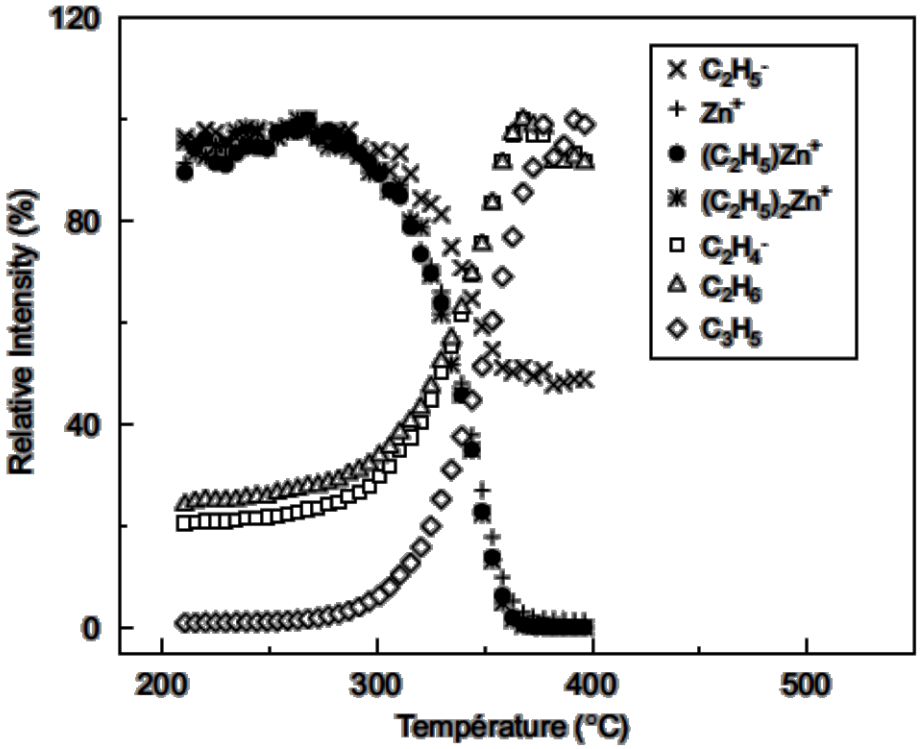

Figure 3-1 Thermal decomposition of DEZn in H_2 as function of temperature [125]

Some studies have shown that DEZn completely decomposes in H_2 at 360 ˚C [125]. Figure 3-1 shows the pyrolysis of DEZn as function of temperature, showing efficient decomposition at around 350 ˚C. It also shows the possible products of the pyrolysis, which are ethylene and ethane. Table 3-1 shows the MOCVD growth of ZnO using various oxidizing agents and their optimum temperature. In all cases, DEZn was used as Zn source. The optimum growth temperature using DEZn varies depending on the oxygen precursors, the reactor geometry and other MOCVD parameters.

Table 3-1 Examples of MOCVD growth studies of ZnO using various oxidizing agents using DEZn as Zn source

Oxygen source	**Optimum growth temperature**	**Substrates/reactor pressure**
TBOH [126]	380 ˚C	Si(100)/300 Torr
NO /NO_2 [127]	420 ˚C	Glass/1 Torr
CO_2 [128]	600 ˚C	Si(111)
H_2O [106]	680 ˚C	GaN/Al_2O_3 /760 Torr
$(CH3)_2CHOH$ [129]	380 ˚C	Sapphire/400 Torr

Some properties of DEZn are summarized in Table 3-2. The Antoine equation permits the calculation of the vapour pressure of the metalorganic at a specific bubbler temperature T (in K). For example, for a bubbler temperature of 5 ˚C, the vapour pressure of DEZn is found to be around 5 Torr.

Table 3-2 Summary of DEZn properties

Antoine equation	Boiling point (˚C)	Fusion point (˚C)
$\mathbf{log P_{DEZn}(Torr) = 8.28 - \frac{2109}{T(K)}}$	118	-28

Bis-(methylcyclopentadienyl)-magnesium [$Mg(CH_3–C_5H_4)_2$]

Bis-(methylcyclopentadienyl)-magnesium is normally used as *p*-type dopant in III-V compounds such as InP [130], GaN [131] and for the growth by MOCVD of semiconductor materials such as MgB_2 [132] and MgS [133]. $(MeCp)_2Mg$ has a higher vapour pressure than (cyclopentadienyl)-magnesium (C_5H_5-Mg, Cp_2Mg). $(MeCp)_2Mg$ is a liquid precursor for the deposition of $Mg_xZn_{1-x}O$, with a reasonably high volatility and easy synthesis even from commercially available products. Moreover, Carta *et al.* [134], in their comparative work on different Mg precursors, showed that $(MeCp)_2Mg$ gives an appreciable higher growth rate compared to the other organometallic Mg sources. They ascribed this to the fact that the Mg–C bond is favourable to protolytic cleavage, which is increased by the oxophylic character of magnesium. Nevertheless, this organometallic precursor presents some difficulties during MOCVD growth, due to its lower vapour pressure. Also, this organometallic compound is pyrophoric (like DEZn) and can produce dust of a hazardous particle size. Unlike DEZn and tertiary-butanol, the thermal decomposition mechanism of $(MeCp)_2Mg$ has not been studied to date. However, cyclopentadienyl compounds have been found to decompose at low temperature (below 400 ˚C) and allow a high growth rate [105].

Some properties of $(MeCp)_2Mg$ are summarized in Table 3-3. The calculated vapour pressure for a bubbler temperature of 48 ˚C (used in this work) is around 0.9 Torr. This is almost six times smaller than the vapour pressure of DEZn.

Table 3-3 Summary of $(MeCp)_2Mg$ properties

Antoine equation	Boiling point (˚C)	melting point (˚C)
$\mathbf{logP_{(MeCp)_2Mg}(Torr) = 7.30 - \frac{2358}{T(K)}}$	56-60/0.3Torr	29

Group VI precursors

Tertiary butanol (TBOH) and oxygen (O_2) remain the foremost oxidants for ZnO and $Mg_xZn_{1-x}O$. They have been thoroughly studied and optimised in MOCVD growth of ZnO [66]. In our group, TBOH has been the main oxygen precursor for the growth of ZnO. For the growth of $Mg_xZn_{1-x}O$, oxygen gas has also been suggested to be a useful O-source [93]. In addition to TBOH [14] and oxygen gas [135-137], CO_2, N_2O [135, 138], NO_2 [139] or H_2O [140] are also used for ZnO and $Mg_xZn_{1-x}O$ grown by MOCVD.

Tertiary butanol (TBOH) [$(CH_3)_3COH$]

Tertiary butanol has been reported to lead to a reduction of premature reactions as compared to oxygen (O_2) or H_2O sources [140]. The growth of ZnO and $Mg_xZn_{1-x}O$ using TBOH has been studied [141] and results have shown that high quality layers can be produced. The decomposition temperature in H_2 has been found to be between 360 ˚C and 430 ˚C (Figure 3-2).

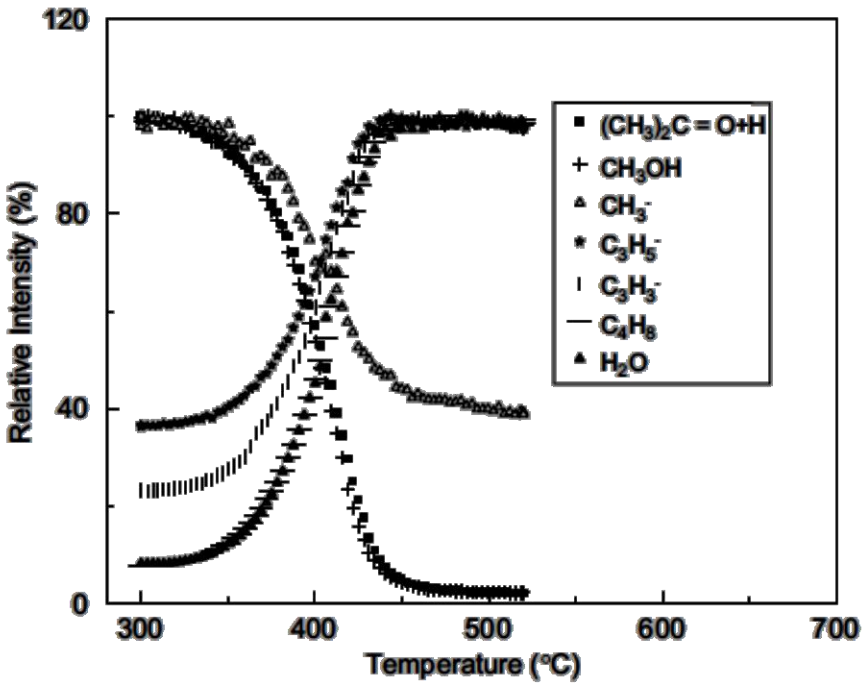

Figure 3-2 Thermal decomposition of TBOH in H_2 as function of temperature [125]

It has been shown that mixing of DEZn and TBOH form an intermediate phase called alkylzinc alkoxide [123], which leads to an optimum decomposition temperature between 380 °C and 450 °C. The properties of TBOH are summarized in Table 3-4.

Table 3-4 Summary of TBOH properties

Antoine equation	Boiling point (˚C)	melting point (˚C)
$\mathbf{logP_{TBOH}(KPa) = 16.6 - \frac{3576}{T(K) - 57}}$	83	25

Oxygen gas [O_2]

The growth of high-quality ZnO and $Mg_xZn_{1-x}O$ films using O_2 is difficult, since ZnO powder is generated by a reaction between Zn and this oxygen precursor in the vapour phase. Oxygen gas remains the most reactive oxygen source with DEZn. However, it still gives good quality layers, especially when combined with DEZn and $(MeCp)_2Mg$. Figure 3-3 shows an Arrhenius plot of the growth rate of ZnO using DEZn and O_2 sources. Bang *et al.* [142] have shown from this study that the optimum growth temperature lies between 400 °C and 650 °C. Beside the strong premature reaction, which is minimised by the use of a two-inlet reactor, the growth of ZnO using O_2 is as commonplace as using TBOH, and yields similar crystalline quality, optical quality and Mg incorporation efficiency [14].

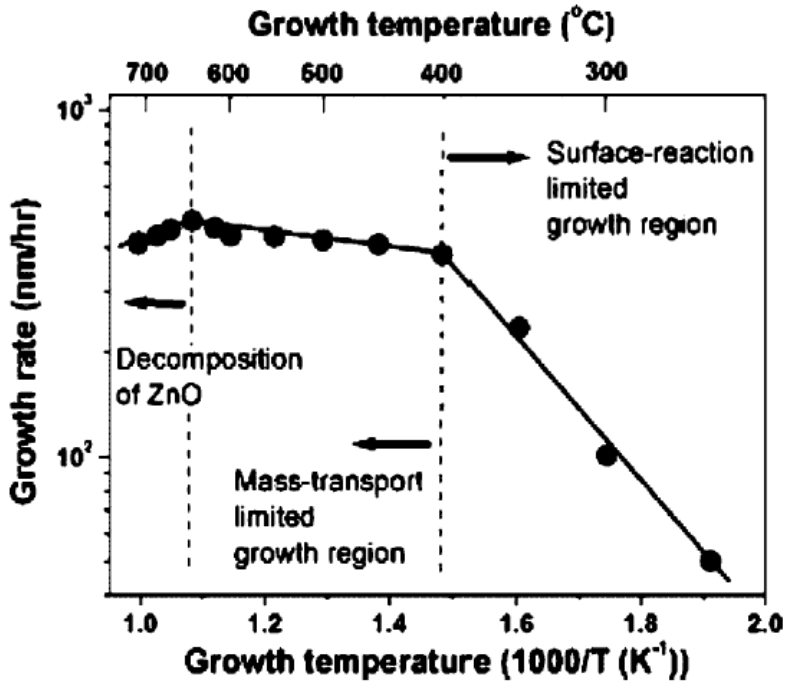

Figure 3-3 Arrhenius plots of the growth rate of ZnO using DEZn and O_2 sources [142]

3.1.2 Sources of contamination

The principal sources of contamination in MOCVD growth are the precursors themselves. The unintentional incorporation of impurities such as C, In, Al, Ga, Li and H, all results from the sources such as DEZn, $(MeCp)_2Mg$, TBOH and oxygen. However, some impurities can diffuse from the substrate into the films, like Al from sapphire substrate. These impurities are undesirable: hydrogen, for example is believed to be responsible for the persistent *n*-type conductivity [143]. Nevertheless, suppliers are making a concerned effort to produce higher purity precursors (electronic grade), which naturally increases the cost of these precursors.

3.1.3 Growth parameters

In MOCVD studies, many parameters such as the growth temperature, the growth time, the growth rate, the growth pressure, the ratio between sources, etc, must be taken into account in order to optimise the material. All the parameters are linked in a certain way. For example, the growth rate can be influenced by the growth temperature; also the ratio between elements could cause the optimum temperature to change. In the present study of ZnO and $Mg_xZn_{1-x}O$, the growth temperature, the growth rate as well as the VI/II ratio have been varied as the main growth parameters.

Growth temperature

The growth temperature or substrate temperature has a strong effect on the structural and optical quality on the deposited films. For example, for ZnO thin films, Kirchner *et al.* [144] found that at temperatures <380 ˚C using DEZn and TBOH, the growth rate is limited by the chemical reaction rate. At higher temperatures, the growth rate decreases due to pre-reactions in the gas phase. In an intermediate temperature range, the growth rate is constant and is mass transport limited. In this case, at a constant flow rate, the growth rate will practically be independent of the growth temperature and all the chemical species transported toward the surface are reacting toward the end product. For ZnO growth, the optimum growth temperature has been found to be between 350 °C and 450 °C [30]. This result is in agreement with the temperature range in which the decomposition of DEZn and TBOH occurs (see section 3.1.1). Using DEZn and $(MeCp)_2Mg$, Thiandoum *et al.* [139] have shown that the incorporation of Mg depends strongly on the growth temperature. They found that higher growth temperatures (~700-800 ˚C) give excellent optical and structural qualities at atmospheric reactor pressure using NO_2 as oxygen source.

VI/II ratio

The VI/II ratio in the input stream is varied to control the stoichiometry of the compound. It is found that the VI/II ratio can influence strongly the structural and optoelectronic properties. An increase in oxygen flow rate leads to a violent reaction with DEZn, which results in an increase in roughness of the surface and changes the morphology of the film. According to nucleation theory such an effect on the morphology is well predicted by the following equation [145].

$$N = A\exp\left(-\frac{\Delta G^*}{RT}\right) \tag{3.2}$$

where N is the nucleation density, ΔG* is the activation energy of nucleation, R is the universal gas constant and T is the growth temperature.

It has been shown that the free energy is proportional to the partial pressure of TBOH, which is part of the activation energy of nucleation. This implies that the density of crystallites can be improved at higher VI/II ratio [141]. In addition, increasing VI/II ratios lead to higher dislocation densities at the interface between substrate and epilayer [146]. Also, vacancies and interstitials can be created during the variation of the VI/II ratio. The creation of vacancies/interstitials could affect impurity incorporation. Furthermore, in ternary alloys, the VI/II ratio has been found to greatly affect the incorporation of the substituting atom. For example, in ZnSeTe [147], an increase in VI/II ratio tends to decrease the Te incorporation efficiency. Interestingly, in GaAs, one can change the carrier type from *p* to *n* by changing the V-III ratio [148]. Overall, the ratio plays a great role in MOCVD growth and therefore needs to be optimised to get high quality material. In previous studies in our reactor [49, 123], the optimisation of growth of ZnO thin films using TBOH and DEZn have shown that the optimum VI/II ratio is about 60 at a growth temperature between 200˚C and 700˚C.

Growth rate

Similar to the growth temperature and the VI/II ratio, the growth rate plays a vital role in MOCVD. From the previous section, one can easily deduce that the growth rate is influenced by the growth temperature (desorption rate) and the VI/II ratio (flux of atoms being transported, adsorption rate) or precursor flow rate. In general, for MOCVD growth, low growth rates have been found to give better layer quality. Other factors which can affect the growth rate are the substrate orientation, reactor pressure, substrate orientation, reactor

geometry, and substrate type. An increase in the growth rate can reduce the degree of order (perfect arrangement of the atoms) in a semiconductor.

3.2 Growth system

The MOCDV growth system used in this work is described in the theses of K. T. Roro [123] and J. K. Dangbégnon [49]. A laboratory scale system from Crystal Growth Technologies was used. Purified argon and nitrogen (6N) were used as carrier and diluent gas. The gases are delivered through stainless steel pipes equipped with pneumatic valves. Several changes had to be made, including the lowering of the reactor pressure (from 250 Torr to 20 Torr) and the use of a dual inlet reactor, described later (see appendix). The piping, all ¼ inch diameter, was heated to 60 ˚C to prevent condensation in the lines. All gas lines are equipped with electronic MKS mass flow controllers to deliver and control the required volumes of reactants. The organometallic sources are contained in stainless steel bubblers and their vapour is transported by Ar gas. During growth, the bath temperature of DEZn was kept at 5 °C for the $Mg_xZn_{1-x}O$ samples and 25 ˚C for ZnO samples during optimisation, which gives a vapour pressure of 5 Torr and 16 Torr, respectively. The $(MeCp)_2Mg$ bubbler was kept at 48 ˚C, yielding a vapour pressure of 0.9 Torr. In order to prevent the condensation of precursor vapour in the delivery lines and clogging of the gas handling system, all sections of the piping that transport chemical vapour were heated to above the saturation temperature of the precursor. The bath temperature of TBOH (99.9999 % or 6N purity) was kept at 30 ˚C, yielding a vapour pressure of 57 Torr. Using the ideal gas equation, $PV = nRT$, the number of moles of each source was calculated. The molar fraction of Mg in the vapour phase $x_V = \frac{n_{(MeCp)_2Mg}}{n_{(MeCp)_2Mg}+n_{DEZn}}$ and the VI/II ratio $\frac{VI}{II} = \frac{n_{VI}}{n_{II}}$ (number of moles of group VI over number of moles of group II) were varied.

During growth these parameters have been varied to systematically study ZnO thin films, as well as Mg incorporation into ZnO. The growth temperature was varied from 280 °C to 680 °C. The V/II ratio was varied from 60 to 960 and the growth time from 30 min to 240 min, keeping the VI/II ratio and the growth temperature constant. As stated above, these growth parameters strongly influence impurity incorporation and defect formation during growth and consequently the optical, electrical and structural properties.

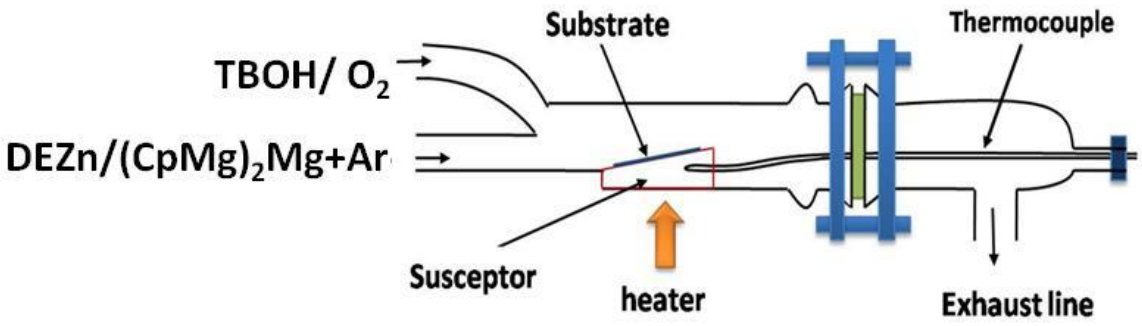

Figure 3-4 Schematic diagram of the two inlet quartz reactor tube

Reactor design

The quartz reactor tube (see Figure 3-4) is designed to minimise premature reactions between the group II and the group VI precursors. The substrate is heated by a halogen lamp positioned directly below the susceptor, as indicated by the arrow in Figure 3-4. The growth temperature is monitored by a type-K thermocouple embedded in a small hole in the susceptor. The temperature is controlled by a digital PID temperature controller. The susceptor is made of graphite and makes an angle of 20° with the horizontal reactor floor. This configuration improves the uniformity of deposition compared to a flat susceptor.

3.3 Substrates

A variety of substrates were used in this work: Al_2O_3 (0001), Al_2O_3 (1-102), ZnO (0001) substrate (supplied by Crystec), Si (111), Si (100), GaAs (100) and glass. A number of these substrates have large lattice mismatch with ZnO and $Mg_xZn_{1-x}O$. For example Si, GaAs and Al_2O_3 (after a 30˚ in plane rotation) have a 40%, 42.4% and 18.4% lattice mismatch with ZnO, respectively. It should be noted that, except for bulk ZnO, there is not a perfectly matched substrate for ZnO. However, growth studies on bulk ZnO have yielded contradicting results in terms of optical and electrical quality. Nevertheless, it has been found that the O surface is better than the Zn surface for epitaxial growth, because mechanical damage can easily occur on the softer Zn surface [5]. C-plane and r-plane sapphire substrates are predominantly used for heteroepitaxial growth of ZnO and $Mg_xZn_{1-x}O$. Even though the growth was performed on other substrates, the $Mg_xZn_{1-x}O$ thin films reported on here were grown on c-sapphire, unless specified otherwise. Figure 3-5 shows the epitaxial relationship between sapphire and ZnO (0001). The growth of ZnO films on c-plane sapphire usually results in the epitaxial relationship ZnO

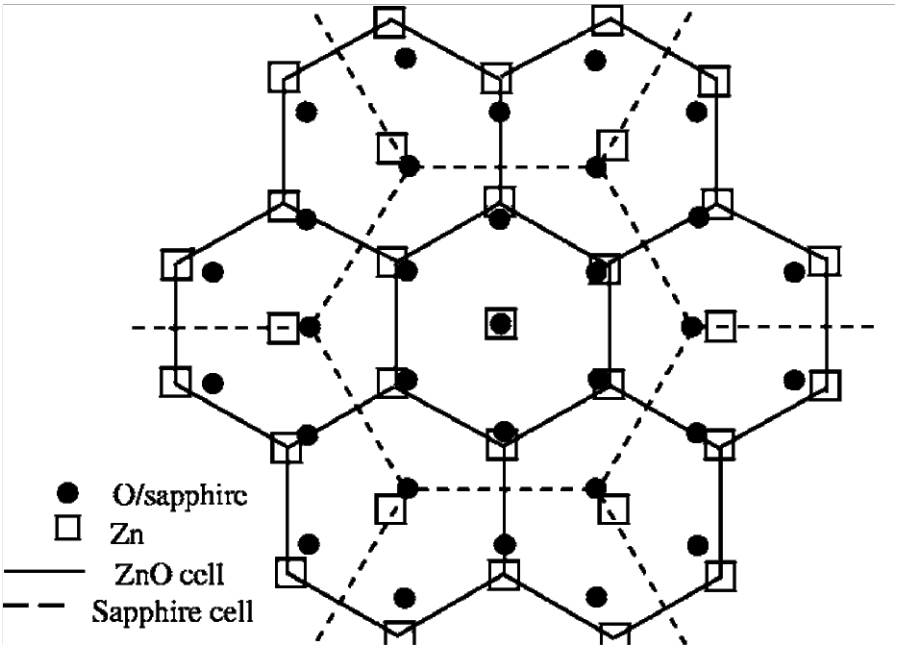

Figure 3-5 Schematic diagram showing the epitaxial relationship of ZnO (0001) grown on Al_2O_3 (0001) [5]

(0001) //Al_2O_3 (0001) and ZnO [$10\bar{1}0$] //Al_2O_3 [$11\bar{2}0$]. Basically, the m-plane normal direction of ZnO aligns with the a-plane normal of sapphire [46].

The surface quality of the substrate is fundamental for good deposition since the presence of defects or particles located on the surface can influence the adsorption rate, the diffusion and the nucleation of the reactive species [149]. Prior to growth, all the substrates were degreased consecutively in heated trichloroethylene, acetone, and methanol and then rinsed in deionised water and blown dry with N_2 gas. The silicon substrates were etched for 1 min in 1:10 solution of HF:H_2O, after the degreasing procedure, in order to remove the SiO_2 layer, which is formed during exposure to air. This amorphous layer tends to degrade the crystalline quality of the $Mg_xZn_{1-x}O$ layer.

3.4 Deposition process

In MOCVD, the three phenomena that play a great part in the process are hydrodynamics, thermodynamics and kinetics, as mentioned earlier. Understanding the dynamic behaviour of fluids is necessary to describe the transport of the gaseous chemical species to the surface to be covered as well as the evacuation of the by-products of the reaction. Modelling gas flow near the surface of the substrate led to the introduction of the concept of a "boundary layer". The boundary layer is a transition zone, where the speed of gas passes from its average value

to zero at the surface. During deposition, reactive species diffuse in opposite directions through the boundary layer. The addition of material on the surface depends on the distribution coefficients of the species and the characteristics of the boundary layer, like its thickness. When the reactants reach the surface, the thermodynamic laws inform about the possible reactions occurring. The deposition process can be divided into different steps, illustrated in Figure 3-6:

- ✓ Transport of the various gas species towards the surface
- ✓ Diffusion of the various gas species through the boundary layer
- ✓ Adsorption of these species on the surface
- ✓ Decomposition of the precursors on the substrate, displacement of the species on the surface, incorporation in the film
- ✓ Desorption of the gas by-products of the reaction
- ✓ Diffusion of the products of the reaction through the boundary layer
- ✓ Elimination of the by-products of the reaction far from the substrate

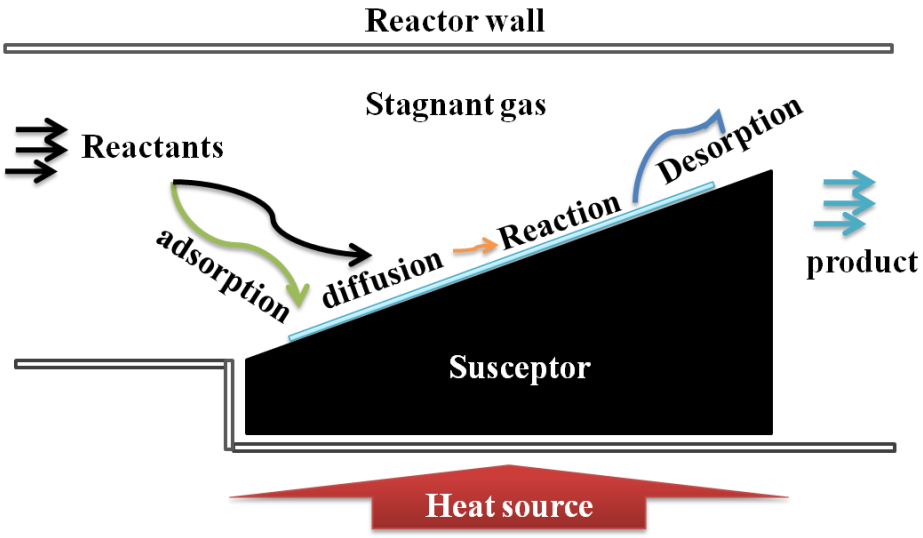

Figure 3-6 Schematic diagram of growth process

Growth mode

There are many types of growth modes, the main three, which have been extensively studied being the Frank-van der Merwer mode, the Volmer-Weber and Stranski-Krastanov modes [151]. The growth mode depends on various parameters of which the most important are

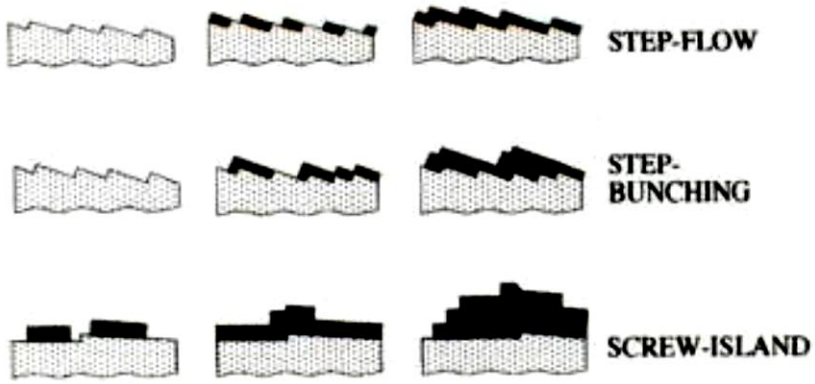

Figure 3-7 Illustration of step flow growth, step bunching and screw-island growth [150]

the thermodynamic driving force and the misfit between substrate and layer. For example, for lattice-matched systems, the growth mode is determined by the relation between the energies of two surfaces and the interface energy. In addition to these classical epitaxial growth modes mentioned above, there are four additional growth modes: step flow mode, columnar growth, step bunching and screw-island growth [152] (see Figure 3-7 for illustration). We will only focus here on the growth mode encountered in most cases in the present study. Figure 3-8 shows a typical cross sectional SEM image of a $Mg_xZn_{1-x}O$ layer on Si (100), illustrating columnar growth and the surface is very rough. For ZnO, in general, there is a very strong tendency of c-axis oriented growth, with a much higher growth rate in the c-direction as compared to other crystal directions. This often leads to columnar structures, even at relatively low temperatures.

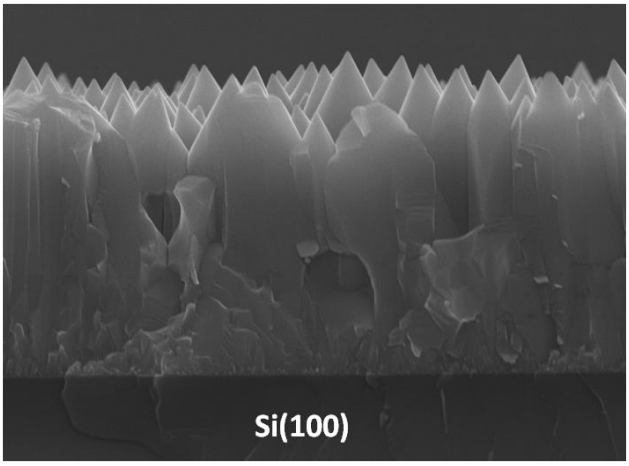

Figure 3-8 Cross sectional SEM view of $Mg_xZn_{1-x}O$ on Si (100) substrate

Chapter 4 Characterization techniques

This chapter introduces the techniques used for the characterization of the $Mg_xZn_{1-x}O$ films. The optical and structural properties were studied by photoluminescence (PL) (4-300 K), X-ray diffraction (XRD), scanning electron microscopy (SEM), transmission electron microscopy (TEM), and auger electron spectroscopy (AES). Energy dispersive x-ray spectroscopy (EDX) was used to estimate the elemental composition of the films.

4.1 X-ray diffraction (XRD)

The crystalline quality of the films has been systematically studied by X-ray diffraction (XRD). This technique is a non-destructive method of analysis of the phase (structure) and the crystal orientation. The diffractometer used is a Philips PW 1840 diffractometer (with a resolution of 0.05˚ (2θ)), which employs CuK_α radiation (λ=1.5405 Å). Figure 4-1 shows the spectra of ZnO and $Mg_xZn_{1-x}O$ (with x=0.45, T_g=420 ˚C, VI/II ratio=60). The diffraction from the (0002) plane of ZnO is at 34.43˚, corresponding to an interplanar distance of 2.60 Å. It is also noticeable that the incorporation of Mg leads to a decrease in the c-axis lattice constant, which causes the (0002) peak to shift toward higher angles. In addition, due to phase segregation, the (111) plane corresponding to cubic MgO appears. Furthermore, most of our films are preferentially oriented with the c-axis perpendicular to the substrate. Many publications on ZnO and $Mg_xZn_{1-x}O$ growth have illustrated that the films are highly c-axis oriented, since the base plane has the lowest surface energy [153]. X-ray diffraction is a good way to estimate the average grain size D of polycrystalline/textured films. According to Scherrer's formula [154]:

$$D = \frac{0.94\lambda}{\beta\cos\theta} \qquad (4.1)$$

where λ is the X-ray wavelength, β (in radians) is the width at half height and θ is the diffraction angle. The average grain size found for the $Mg_xZn_{1-x}O$ films is around 50 nm to 60 nm. The c-axis lattice parameter, which is known to vary with Mg content, has been determined from XRD and will be discussed in chapter 5.

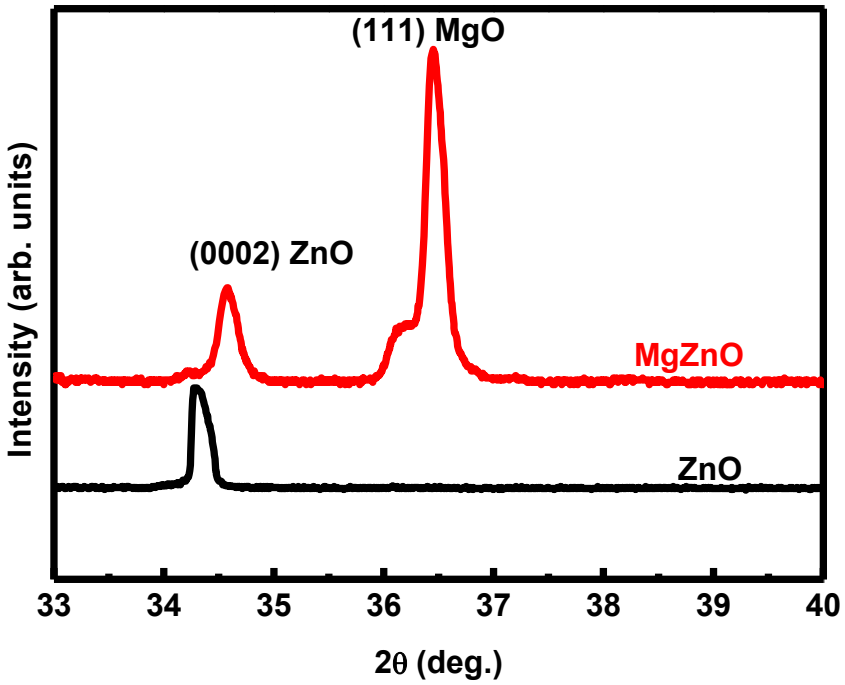

Figure 4-1 XRD spectra of ZnO and $Mg_{0.45}Zn_{0.55}O$ grown on c-Al_2O_3

4.2 Scanning electron microscopy (SEM)

Scanning electron microscopy is useful for the exploration of a diversity of specimens in various fields such as materials science, semiconductor research and microelectronics [155]. In the present study SEM has primarily been used for surface visualization of the ZnO and $Mg_xZn_{1-x}O$ films. Like XRD, it is a non-destructive technique commonly used for surface analysis. It is capable of producing high resolution images, both planar and in cross-sectional views. A Philips XL30 scanning electron microscope and Jeol JSM-7001F Field Emission Scanning Electron Microscope (FESEM) were used to inspect the morphology and to measure the thickness of the $Mg_xZn_{1-x}O$ films. For the FESEM, instead of a thermionic gun, a field emission gun is used for electron beam generation, which allows the formation of an electron probe with diameter of about 0.5 nm [155]. Additionally, it enables specimens to be imaged at low acceleration voltages, i.e. below 5 keV, with high resolution. Figure 4-2 shows typical FESEM images of ZnO and $Mg_{0.25}Zn_{0.75}O$ grown on c-sapphire substrate. Clear surface features are observed, showing the power of this technique. Measurements of the thickness of the films were performed in order to determine the growth rate of the $Mg_xZn_{1-x}O$ films grown in this study.

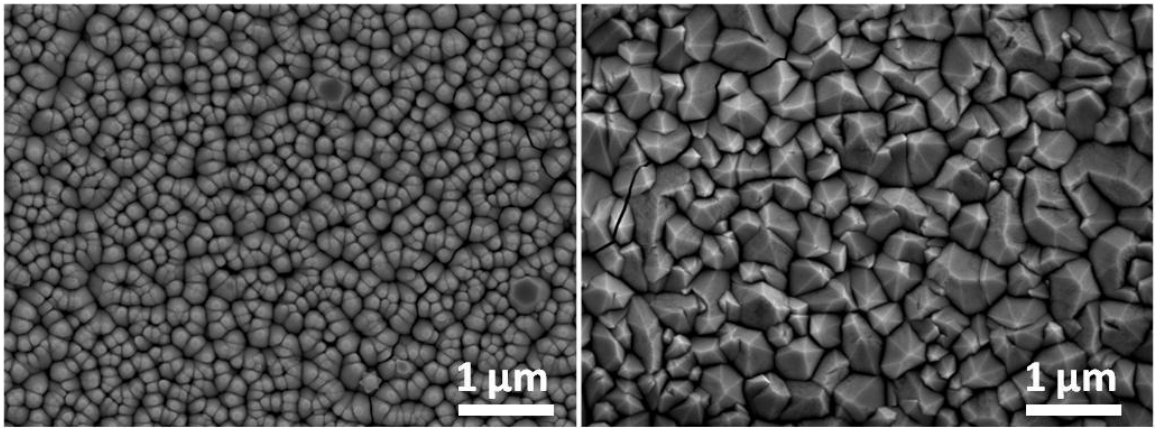

Figure 4-2 SEM images of representative ZnO (left) and $Mg_xZn_{1-x}O$ (x=0.25) (right) thin films grown at 420 ˚C and a VI/II ratio=60 using oxygen gas

4.3 Transmission electron microscopy (TEM)

A JEOL JSM 2100 LAB6 transmission electron microscope (TEM) was used to inspect the nano/microstructure of the films. TEM cross-sectional samples were prepared using standard techniques (mechanical grinding and polishing, followed by argon ion milling at an angle of 4˚). This TEM has three independent condenser lenses and produces the highest probe current for any given probe size, which improves the analytical and diffraction capabilities (see reference [155] for more details). With its characteristics (Table 4-1) one can obtain the atomic resolution of the $Mg_xZn_{1-x}O$ lattice. A bright field TEM image of $Mg_xZn_{1-x}O$ (x=0.01) and corresponding high resolution TEM image obtained along the [11-20] zone axis is shown in Figure 4-3. Columnar growth and the resolution of atomic planes are evident. TEM was also used to confirm the presence of stacking faults in the films.

Table 4-1 Characteristics of JEOL JSM 2100 LAB TEM

Resolution	Accelerating Voltage	Magnification
0.14 nm	80 kV to 200 kV	50x to 1500000x

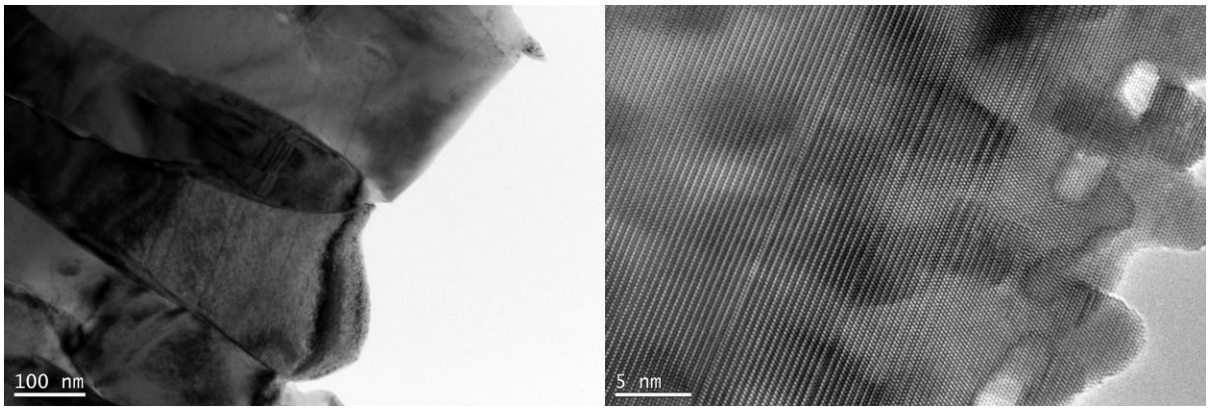

Figure 4-3 TEM images obtained on the JEOL JSM 2100 of $Mg_xZn_{1-x}O$ (x=0.01). The high resolution image on the right was obtained along the [11-20] zone axis

4.4 Energy dispersive X-ray spectroscopy (EDX)

Energy dispersive X-ray spectroscopy (EDX) is an analytical technique used for elemental analysis or chemical characterization of a sample. It relies on the investigation of a sample through interactions between electromagnetic radiation and matter, analysing x-rays emitted by the matter in response to being hit with charged particles [156]. Its characterization capabilities are due in large part to the fundamental principle that each element has a unique electronic structure allowing x-rays that are characteristic of an element to be identified uniquely from each other. Characteristic X-rays are produced when an energetic electron excites an inner shell electron and an electron from a higher energy shell relaxes to its state, releasing a photon of energy equal to the difference in energy between its initial and final energy levels. EDX was performed using a Jeol JSM-7001F FESEM and used to confirm the incorporation of Mg into ZnO.

Figure 4-4 shows the EDX spectra of as grown ZnO and $Mg_xZn_{1-x}O$ thin films on Si (100). The two spectra are for ZnO and $Mg_{0.28}Zn_{0.72}O$. Various peaks corresponding to specific elements in the periodic table are seen. Only Mg, Zn, and O, with a negligible amount of carbon at 0.25 keV, are present. The peak related to Mg incorporated into the films is observed at 1.253 keV. The ZnL_α, ZnK_α and ZnK_β peaks appear at 1 keV, 8.7 keV and 9.6 keV, respectively, due to electron transitions from different orbits after excitation, which correlate well with reported values by Zhu *et al.* [157]. The position of the OK_α peak is at 0.53 keV.

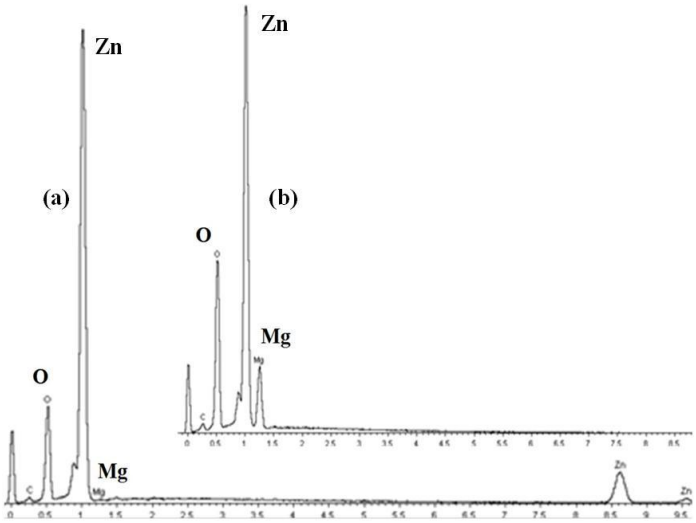

Figure 4-4 EDX spectra taken with a 10 keV incident electron beam of (a) ZnO and (b) $Mg_{0.28}Zn_{0.72}O$

4.5 Auger electron spectroscopy (AES)

AES and scanning Auger microscopy (SAM) were performed on some $Mg_xZn_{1-x}O$ samples using the PHI 700 Scanning Auger Nanoprobe system of the University of the Free State. AES measurements give information on the surface composition as well as information about the chemistry involving these elements. SAM offers the opportunity to obtain higher lateral resolution. AES was done with a 25 kV 10 nA electron beam. It was used to examine the

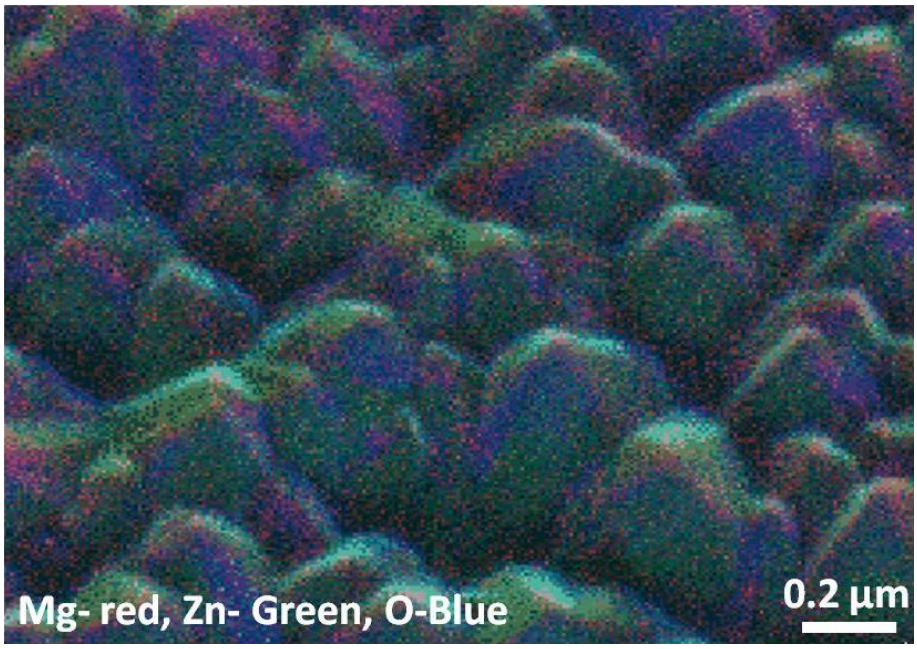

Figure 4-5 SAM map of $Mg_{0.04}Zn_{0.096}O$ grown using TBOH on Si (100)

distribution of Mg atoms on the surface as well as in cross-section to get information on the distribution with depth. Figure 4-5 shows an SAM elemental map of $Mg_xZn_{1-x}O$ grown on Si (100) substrate. The red dots correspond to Mg atoms, the green Zn and the blue oxygen. The solid composition was not determined from this technique because of the strong contribution from adventitious carbon, which affects quantification of the elemental composition.

4.6 Photoluminescence (PL)

PL was used to determine the optical properties of the $Mg_xZn_{1-x}O$ films. It is also a non-destructive spectroscopic technique for analysing intrinsic and extrinsic properties of semiconductors. For low temperature PL (4.2 K) measurements, the samples were immersed in liquid He and excited with the 325 nm line of a HeCd laser (typical excitation power of 7 mW) and the 266 nm line of a Nd:YAG laser (20 mW). Spectra taken at 85 K (liquid nitrogen) or RT were obtained using a Mini-PL UV laser system 5.0 (Photon Systems, USA), which employs the 248.6 nm line of a NeCu laser.

Temperature dependent PL was performed in a closed cycle He cryostat in the temperature range 4.2 K to 300 K. The emission of the sample was focused onto the entrance slit of a 0.5 m SPEX monochromator and detected by a Hamamatsu R3896 photomultiplier tube (PMT) as well as a R666s PMT with a GaAs photocathode. The maximum resolution of the system was 0.02 nm. An optical chopper was used to pulse the laser, which also serves as reference for the lock-in amplifier. The incoming current was amplified by converting it to a voltage using a resistor placed at the entrance of the lock-in amplifier (the lock in technique is used to enhance the signal-to-noise ratio of the detection system). Some PL was analysed using a 1 m SPEX monochromator (TU Dresden, Germany) equipped with a Hamamatsu PMT (R943-02).

When the $Mg_xZn_{1-x}O$ sample is excited by an optical source with an energy greater than the band gap (this justifies the use of the 3 different laser lines 248.6 nm, 266 nm and 325 nm used in this work) electron-hole pairs (e-h) are created. These e-h pairs eventually recombined via several radiative processes. At RT, the primary recombination mechanism is band-to-band recombination: during excitation, an electron is excited from the VB to the CB (Figure 4-6 A). The electron and hole thermalize to their lowest levels in the CB and VB by emitting phonons (heat), and then recombine and emit a photon. The emission of phonons is an extremely fast process, occurring on a picoseconds scale. The photons have energy

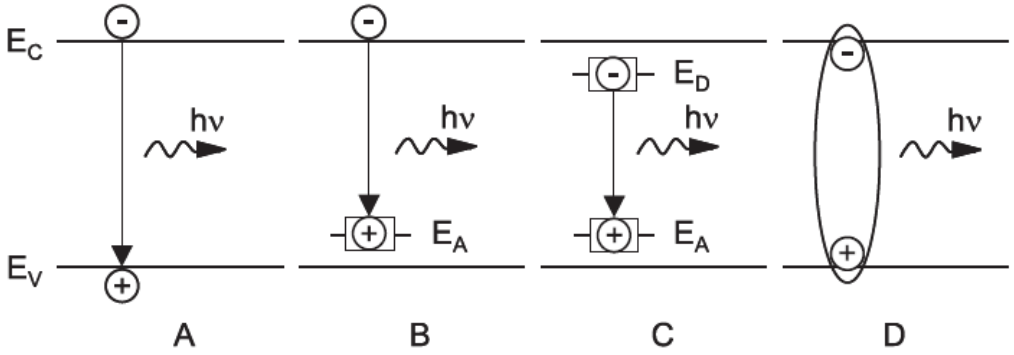

Figure 4-6 Recombination processes in a direct band gap semiconductor: (A) band-to-band transitions (e- h), (B) free-to-bound transition (e, A^0), (C) donor-acceptor-pair transitions (DAP), (D) free exciton transitions

equivalent to the band gap of a direct band gap semiconductor. At low temperature, electron-hole pairs quickly bind together by Coulombic attraction to form an exciton and then emit a narrow spectral line called free excitonic emission [158]. The free exciton (Figure 4-6 D) can move through the crystal and localize on a neutral or ionized donor to form donor bound excitons (D^oX, D^+X). Likewise, acceptors can localize on excitons to form neutral or ionized acceptor bound excitons (A^oX, A^-X). When both donor and acceptor impurities are present in the $Mg_xZn_{1-x}O$ films, an electron on a donor can recombine with a hole on a neutral acceptor to create what is called donor-acceptor-pair (DAP) emission (Figure 4-6 C). Additionally, a free electron can recombine with a neutral acceptor in a free-to-bound transition (FB, FA, (e, A^o)) (Figure 4-6 B).

4.6.1 Free excitons

A free hole and free electron, as a pair of opposite charge, experience a coulomb attraction. They are called free excitons if they don't interact with another center. The coulomb interaction is similar to that of the hydrogen atom. The free exciton binding energy can be obtained from the analogue of the hydrogen atom and is given by [158]:

$$E_{FX} = E_g - \frac{m_r^* e^4}{32\pi^2\varepsilon^2\hbar^2} \qquad (4.2)$$

where ε is the permittivity of the semiconductor and m_r^* is the reduced effective mass [158]. For ZnO, the excitonic binding energy is about 60 meV; for $Mg_xZn_{1-x}O$ one expects higher exciton binding energies, which should increase with Mg content in the crystal to ~80 meV [159].

4.6.2 Donor bound excitons

In the presence of impurities, bound excitons will be measured. When they recombine, the emission is characterized by a narrow spectral width at lower photon energy than that of the free exciton [158]. Bound excitons are excitons that are bound to an attractive center such as a shallow neutral or ionized impurity, a deep impurity, or some other defects. In $Mg_xZn_{1-x}O$ samples, bound excitons dominate the low temperature near band edge PL spectra because of the presence of donors arising from unintentional impurities and/or shallow donor-like defects. The energy of the emitted photon is [160]:

$$\hbar\omega = E_g - E_{BX} - R_X \tag{4.3}$$

where R_X is the exciton Rydberg and E_{BX} is the so called exciton localization energy, which is the energy required to remove the exciton from the impurity [161]. In ZnO, the prominent lines are excitons bound to neutral donors that are located at 3.3598 eV (I_8), 3.3605 eV (I_{6a}), 3.3614 eV (I_5), 3.3628eV (I_4), and 3.3664eV (I_3) [59, 162]. Incorporation of Mg into ZnO is expected to blue shift and broaden the D^oX emission.

4.6.3 Free- to-bound transitions

The transition of a free electron from the conduction band to a neutral acceptor level is denoted by (e, A^0) and the emission energy is given by:

$$E(e,\ A^0) = E_G - E_A + kT/2 \tag{4.4}$$

where E_A is the acceptor ionization energy and T is the temperature of the free electron in the conduction band [163]. These transitions are dominant at intermediate temperatures or at RT, depending on E_A. The lineshape of the (e, A˚) transition is given by:

$$I_{e,A^o}(\hbar\omega) \propto \left(\hbar\omega - E_g + E_A\right)^{1/2} exp\left(-\frac{\hbar\omega - E_g + E_A}{kT}\right) \tag{4.5}$$

where the square root dependence of the pre-factor originates from the density of states and the exponential factor originates from the Boltzmann distribution function [163].

4.6.4 Donor-acceptor-pair transitions

The donor-acceptor-pair transition is an extrinsic transition occurring in semiconductors with high concentrations of residual donors and acceptors [163]. The emission energy of donor-to-acceptor (DAP) or donor acceptor pair transitions is given by [160]:

$$E = E_g - E_a - E_d + \frac{e^2}{4\pi\varepsilon<r>} \tag{4.6}$$

where the fourth term on the right hand side is a coulomb term describing the final state interaction and <r> the average spatial separation between donors and acceptors. This transition can only occur if the separation between constituents of the pair is larger than a critical radius r_c. The intensity is proportional to the overlap integral between the electron and the hole wave function, that is:

$$I_{DAP} \propto exp\left(-\frac{2r}{a_B}\right) \tag{4.7}$$

where a_B is the Bohr radius of the impurity with the smaller binding energy.

4.7 UV transmission

UV-visible transmission spectra were recorded with a Shimadzu UV-3100 UV-vis-near IR spectrometer equipped with a PbS photoconductive cell as detector. This system is able to measure transmission, absorption and reflection data from 190 nm to 3200 nm. This spectrometer is equipped with a double beam, which makes it possible to extract the influence of the substrate and to acquire the transmission spectrum of only the studied layer. The sample surface was illuminated at normal incidence. The spectra were used to extract an approximate value for the band gap of the alloy. The energy band gap was derived from the UV-vis transmission spectra using $(\alpha(\lambda)h\nu)^2$ versus $h\nu$ plots, where $\alpha(\lambda)$ is the wavelength dependent absorption coefficient, and $h\nu$ is the photon energy. Figure 4-7 shows the transmission spectra of three $Mg_xZn_{1-x}O$ thin films. As the Mg content in the vapour phase (x_v) increases the cut off wavelength clearly blue shifts, as expected, due to an increase in the band gap energy.

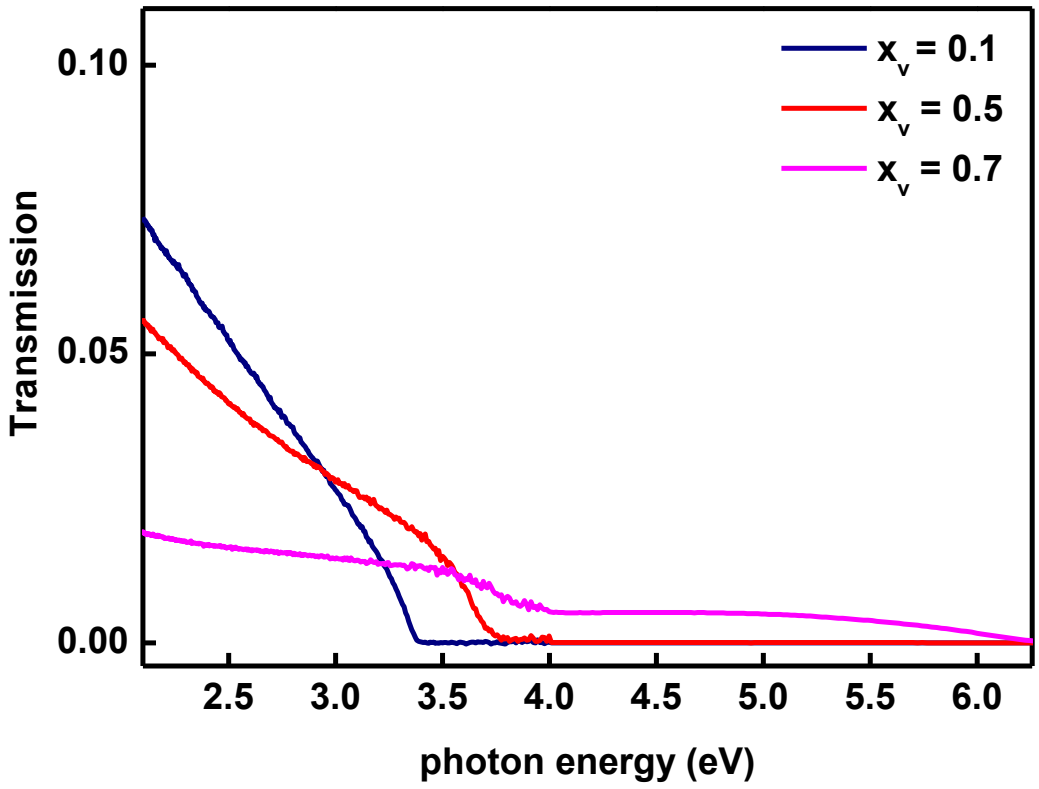

Figure 4-7 Transmission spectra of $Mg_xZn_{1-x}O$ thin films grown with different Mg content in the vapour phase x_v

Chapter 5 Growth and characterisation of ZnO thin films

In this chapter, the influence of the two main growth parameters, i.e. the growth temperature and the VI/II molar ratio in the vapour phase, on the optical and structural properties of ZnO films grown by MOCVD is studied. Details on the growth of films using oxygen gas as oxidizing agent are presented. The effects of Si (100), Si (111), c- and r-sapphire, glass, GaAs and ZnO substrates on the optical, structural and morphological properties of ZnO thin films grown with TBOH are also investigated. This chapter is a preamble to results on the growth of $Mg_xZn_{1-x}O$ using oxygen as oxidizing agent.

5.1 ZnO deposition using oxygen gas as oxidizing agent: Optimization of the growth parameters

5.1.1 Influence of growth temperature and VI/II ratio on growth rate

When ZnO is grown with TBOH, previous studies in our reactor have shown in the low temperature growth regime (200-300 °C), that the growth rate is kinetically limited, i.e. it depends on the growth temperature [111]. For intermediate temperatures (325-400 °C) the growth rate is mass transport limited, i.e. it is independent of temperature, and no variation in structural and optical quality is observed. The growth rate is controlled by the amount of DEZn and TBOH which arrives at the substrate [164]. For higher temperatures (≥400 °C) the growth rate decreases [123] probably due to desorption of zinc and oxygen [164].

An increase in the VI/II ratio at optimal growth temperature (~380 °C) causes the growth rate to increase, which is explained by a competitive adsorption of group II and group VI species on the growth surface. Nishio *et al.* [165] showed that the growth rate is remarkably suppressed for high transport rates of DEZn (i.e. for low VI/II ratios or oxygen deficient conditions), due to a blocking of surface sites by adsorbed species, e.g. methyl radicals resulting from the decomposition of DEZn. For very high VI/II ratios parasitic spontaneous nucleation becomes important, causing the growth rate to decrease [166].

For growth of ZnO using oxygen gas, Figure 5-1 shows the growth rate versus the growth temperature for different VI/II ratios. The films were grown on Si (100) at various temperatures and VI/II ratios. The growth rate increases almost linearly with growth temperature. Also, the growth rate increases with increasing growth temperature, indicating

that the film growth rate is limited by the surface reaction of DEZn and O_2. It appears that the growth rate begins to saturate above 680 ˚C, i.e. that the mass-transport-limited regime is above the range of temperatures studied here.

The growth rate also increases with an increase in the VI/II ratio. The growth rate depends on the oxygen flow rate in the reactor tube. Since the growth rate increases with increasing VI/II ratio, the effective growth condition (on the growth front) is believed to be Zn rich [170]. These results imply that the amount of chemically active oxygen (free radicals, atomic oxygen) that arrive on the evolving surface increases with increasing VI/II ratio, resulting in better stoichiometry between the Zn precursors and oxygen [170].

As the temperature increases, nucleation is also expected to become more efficient, leading to an increase in the deposition rate (at least during the initial stages of growth). Zhu *et al.* [167] investigated the MOCVD growth of ZnO on Si (111) using CO_2 in the temperature range between 450 ˚C and 700 ˚C and showed that as the growth temperature increases, the growth mode changes from kinetically-limited to mass-transport-limited, and finally to desorption-limited mode.

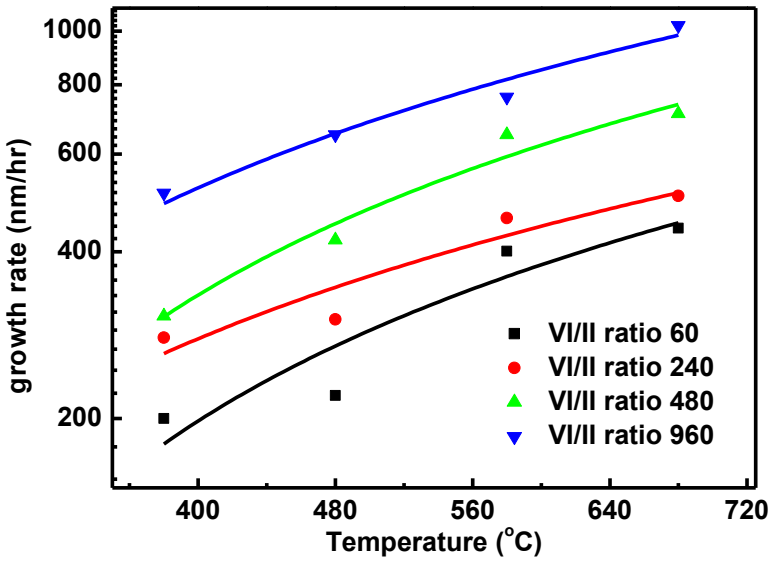

Figure 5-1 Growth rate as a function of growth temperature and VI/II ratio for films deposited at 380 ˚C, 480 ˚C, 580 ˚C and 680 ˚C on silicon substrate

5.1.2 Influence of growth temperature and VI/II ratio on surface morphology

The SEM images in Figure 5-2 show the morphologies of the ZnO layers discussed in the previous section. The morphology varies from hexagonal columns with cone shaped ends to rods. Both an increase in VI/II ratio and growth temperature lead to an increase in the crystallite / rod diameter. The rods show no preferential alignment but their diameters and lengths are rather uniform.

The drastic changes in surface morphology with growth temperature are attributed to various factors, such are the decomposition of the precursors, the nucleation on the surface of the substrate and/or coalescence of nuclei. For temperatures ≤480 ˚C, the surface morphology is fairly uniform, getting rougher with an increase in VI/II ratio. The morphology of the layer grown at 580 ˚C displays a morphology that is a mixture of those observed at 480 ˚C and 680 ˚C. No specific crystallite shape is dominant. At this temperature some rods start to appear, but the films also contain irregularly shaped crystals. At 680 ˚C rod formation is evident.

It is known that the nucleation and coalescence of grains are sensitive to the growth temperature [168]. The initial ZnO deposition will be in the form of nuclei due to the large lattice mismatch with silicon and the native/thermal oxide [170]. According to Zeng *et al.* [171] the nucleation layer will form due to the Stranski-Krastanov (SK) growth mode resulting in some island-like structures on the substrate. The nucleation of ZnO islands on the substrate surface and their evolution will depend strongly on both the temperature and the amount of active oxygen [172]. Higher temperature will promote lateral growth rate leading to larger diameter crystallites as observed. The formation of rods at 680 ˚C stems from a competition among different crystallographic directions, growth along the c-axis being the fastest [173]. It is suggested here that rod formation is enhanced only if sufficient active oxygen is present on the growth front, a notion that is supported by the morphological change from rods and “tubes” at a VI/II ratio of 60 to only rods at a VI/II ratio of 960.

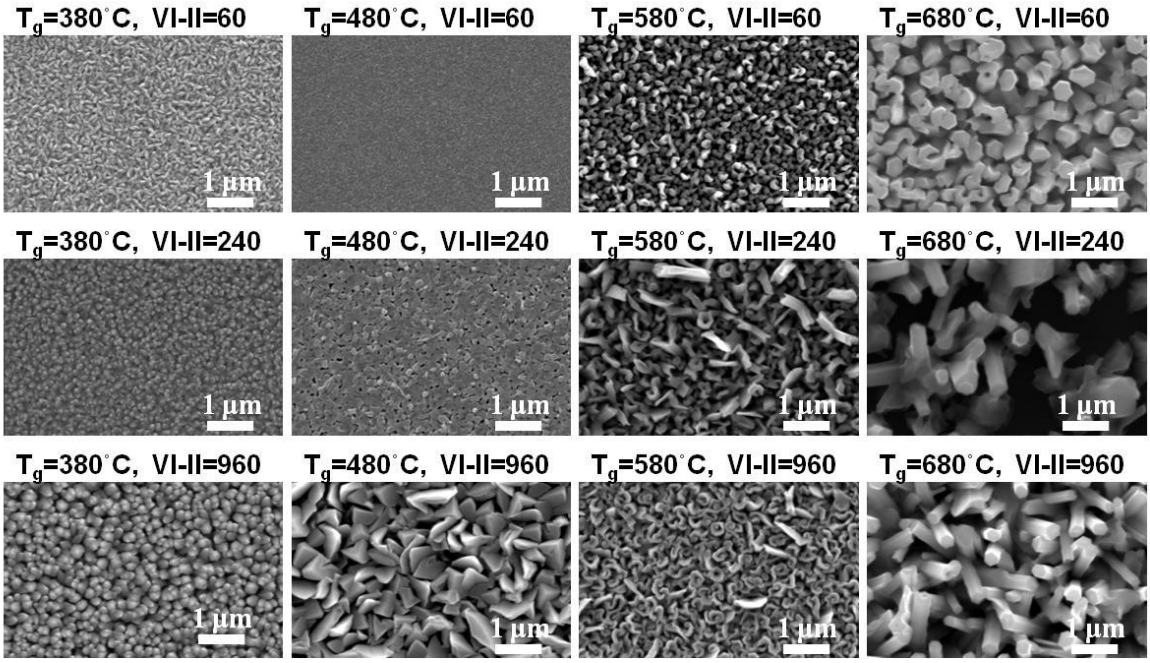

Figure 5-2 The SEM image of the ZnO thin film grown at different temperatures and different VI/II ratios

5.1.3 Effect of growth temperature and VI/II ratio on the optical properties

Figure 5-3 shows a log plot of the low temperature (12 K) PL spectra of the ZnO layers grown at different temperatures and VI/II ratios. In ZnO the near band edge (NBE) emission often dominates because of the presence of donors resulting from unintentional impurities and/or shallow donor-like defects [143]. Two neutral donor bound excitons (D°X) at ~3.359 eV and ~3.362 eV dominate the NBE emission. They are very close to the $I_{6/8}$ and the I_4 lines, respectively [174]. These lines are the fingerprint of Al/Ga and H [59]. Al/Ga is present in DEZn as a trace impurity. It will therefore be incorporated in the films during growth, along with H, which is a constituent of the organometallic molecule. It appears that the hydrogen-related line dominates at higher temperature, but the Al/Ga-related line still remains. The line at 3.335 eV is related structural defect (Y-line) [175]. The structural defect could be a surface defect [44, 174], dislocation, or stacking fault. The intensity of the Y-line increases with growth temperature. In MOCVD, high temperature growth increases the incorporation of carbon in the ZnO films and could cause an increase in structural defects at the surface. Furthermore, the high growth temperature plays a major role in the nucleation. Indeed, an increased nucleation density can promote coalescence of the ZnO islands at high temperature, giving rise to grain boundaries and dislocations. This is in good agreement with the variation

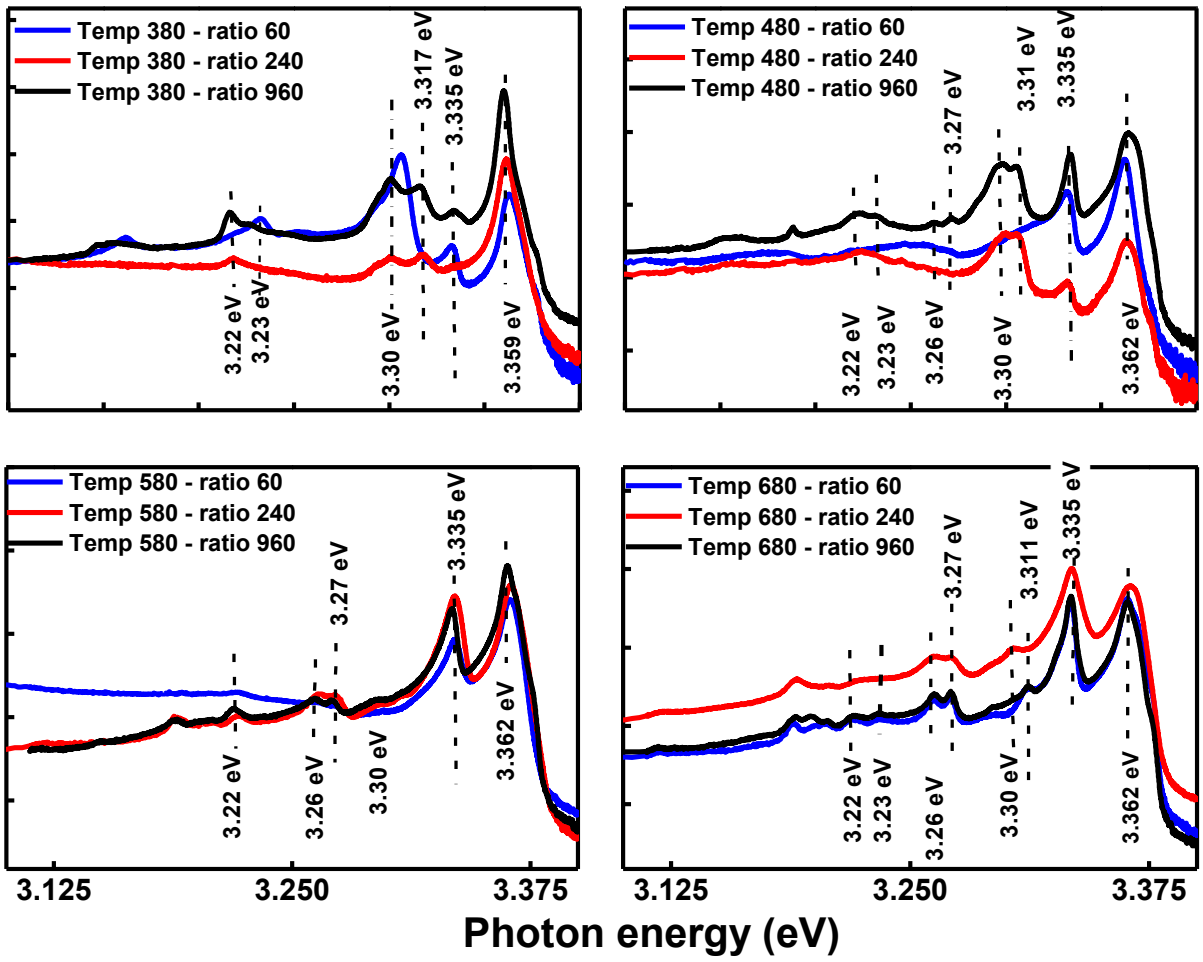

Figure 5-3 Low temperature (T=12 K) PL of ZnO thin films grown on Si (100) substrate with oxygen gas at different temperatures and with different VI/II ratios

in intensity of the structural defect PL, which also increases with growth temperature. The lines at ~3.311 eV and 3.30 eV have been attributed to (e, A^0) and DAP emission [176]. The transitions at ~3.23 eV are ascribed to the first-order longitudinal optical (LO) phonon replicas of the (e, A^0) and DAP, respectively, since the energy separation between them corresponds to the LO phonon energy for ZnO (72 meV). The (e, A^0) peak at 3.31 eV has been assigned to stacking faults by Schirra *et al.* [176]. This PL transition has been unambiguously identified as a transition of electrons from the conduction band to holes localized at stacking fault-related shallow acceptor states [176], resulting from dangling bonds, V_{Zn}, O_{Zn} or O_i [177]. For all the samples (except the one grown at 380 ˚C, VI/II ratio=60) no emission has been observed from deep levels (i.e. in the visible region), which means there is a relatively low concentration of native defects, such as oxygen interstitials, zinc vacancies and oxygen vacancies.

The low temperature growth (≤480 ˚C) yields fewer structural defects and sharper NBE. Low VI/II ratios also yield better optical quality. The optimisation of the ZnO films grown using O_2 gas yields an optimum temperature range from 380 ˚C - 480 ˚C and a VI/II ratio range from 60 - 120.

5.2 Effect of various substrates on ZnO thin films

5.2.1 Introduction

Several studies have been reported on ZnO grown on different substrates, mainly sapphire (Al_2O_3) [178], Si [179], GaAs [180], bulk ZnO [174] and glass [181]. Different conclusions were drawn in terms of the influence of the substrate on the properties of ZnO films. These studies have compared mainly different orientations of one type of substrate, e.g. c-, r-, a- and m-plane sapphire [182], different orientations of GaAs ((100) versus (111)) [164] or different faces of ZnO (O-face versus Zn-face) [183].

For example, Fu *et al.* [179] reported that the nucleation of ZnO on Si is difficult due to the fact that ZnO crystallizes in a hexagonal (wurtzite) lattice on cubic (diamond) Si [126]. The difference in thermal expansion is another limiting factor. It was mentioned earlier that the formation of SiO_x on Si is a highly likely process in the reactor. This will contribute to the degradation of the film quality and cause a randomly oriented polycrystalline film [184]. The effect of diffusion of the constituents of the substrate was studied for ZnO deposited on GaAs. Bang *et al.* [180] suggested that GaAs can provide As atoms, which will diffuse into the film and act as *p*-type dopant. ZnO on c-sapphire has been reported to be monocrystalline, with the ZnO c-axis perpendicular to the substrate surface [178]. Growth of ZnO on r- Al_2O_3 is reported to be epitaxial, whereas on most of the other commonly used substrates, like Si and GaAs, the films are textured [185]. In many studies of ZnO films, sapphire was used as substrate because the oxygen sublattice of sapphire has the same hexagonal symmetry as ZnO. This facilitates epitaxy and can produce the epitaxial relationship shown in Figure 3-5. As in the case of Si as substrate, the growth of ZnO on Al_2O_3 faces several problems due to the differences in chemical nature, structure (wurtzite on corundum), lattice parameters, and thermal expansion [186]. The lattice mismatch between c-sapphire and ZnO is reported to cause high densities of misfit dislocations at the interface [187]. In this section, the effect of different substrates on the optical and structural properties of MOCVD ZnO is illustrated.

5.2.2 Structural properties

Figure 5-4 shows normalised XRD spectra of ZnO thin films on different substrates grown at 380 ˚C with a VI/II ratio=60. TBOH was used as group VI species. Only the (0002) peak of ZnO is observed in each case, showing preferred c-axis orientation of the layers. The dominance of the (0002) ZnO peak for all substrates indicates that the substrate type and orientation do not influence the orientation of the films. Van Drift [188] reported that even in the absence of epitaxy, the preferred film orientation can often be explained by the evolutionary selection rule, which states that the fastest growing crystallographic plane will dominate other planes and thus determine the final orientation. Therefore, regardless of the substrate, the (0001) orientation may competitively dominate other orientations. The insert in figure 5-4 shows the full-width at half-maximum (FWHM) of the films. The FWHM has been extracted by doubling the half-width at half-maximum, measured on the low-angle side of the lines. This was done in order to minimize the influence of overlap between the $K_{\alpha 1}$ and $K_{\alpha 2}$ peaks. The values are different from substrate to substrate and this can be translated to grain size. The XRD peak width is inversely proportional to the grain size, according to Scherrer's formula [188]. The average grain sizes obtained from this formula range between 46 nm for GaAs substrate and 78 nm for ZnO (O-face) substrate.

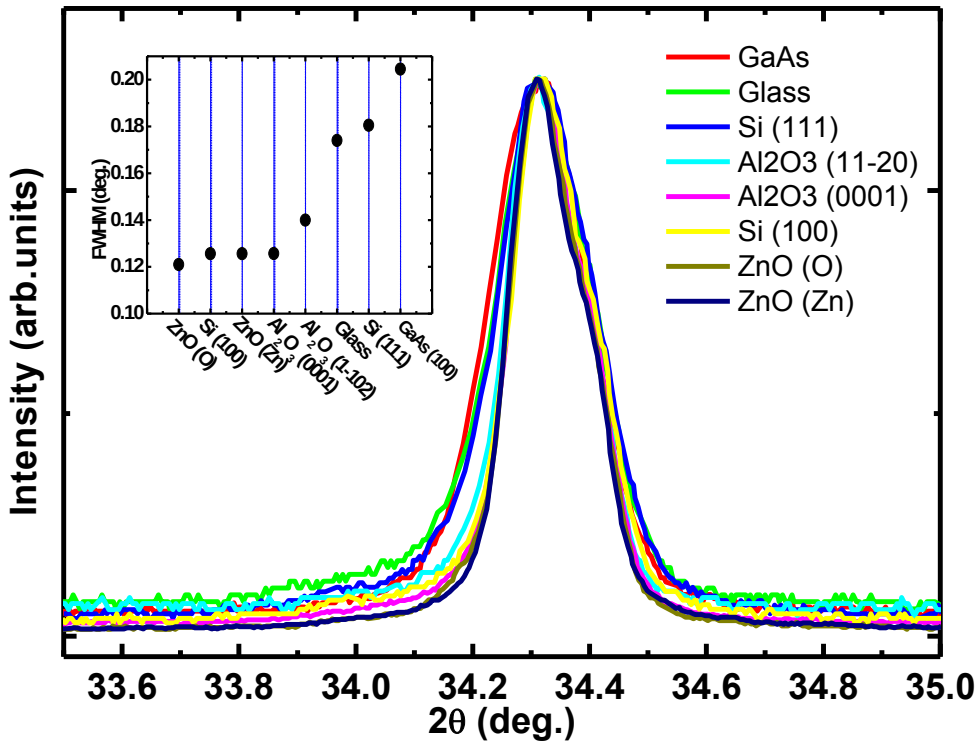

Figure 5-4 Normalized XRD spectra of ZnO films grown on different substrates

5.2.3 Morphology analysis

The surfaces of the ZnO films grown on the various substrates are shown in Figure 5-5. The morphologies are similar, with hexagonal columns having cone shaped ends. In all cases these columns are roughly perpendicular to the substrate, as shown in a cross-sectional SEM view for one of the samples in Figure 5-6.

The observed columnar growth is a result of the high growth rate along the c-axis of ZnO and correlates well with the preferred c-axis orientation of the grains seen in XRD spectra. The average diameter of the columns is the largest for growth on GaAs (100) substrate, which appears to differ from the XRD results. However, it is worthwhile mentioning that XRD gives an estimation of the grain size, while the crystals observed by SEM are probably not single crystalline. The narrowest columns are observed for ZnO films on glass and Si (111) substrate. Wider, but similarly shaped columns are observed for growth on ZnO, Si (100) and Al_2O_3. It is valuable to note the substrate position on the susceptor has strong effects on the growth rate (laterally and vertically), due to gas phase depletion along the flow direction, and also on the layer quality.

It is interesting to note that the trends in the microstructure (deduced from XRD) and in surface morphology (from SEM) do not track each other, neither in terms of substrate type nor orientation, nor in terms of lattice mismatch. The lattice mismatch between ZnO and the various substrates varies hugely: GaAs has the biggest lattice mismatch with ZnO (42%), Si (100) and Si (111) are mismatched by 40% and 16%, respectively, while c- and r-Al_2O_3 have atomic spacings that are 18% and 1.6% respectively, larger than that of ZnO. One would expect grain size (and columnar width) to correlate roughly with lattice mismatch, in

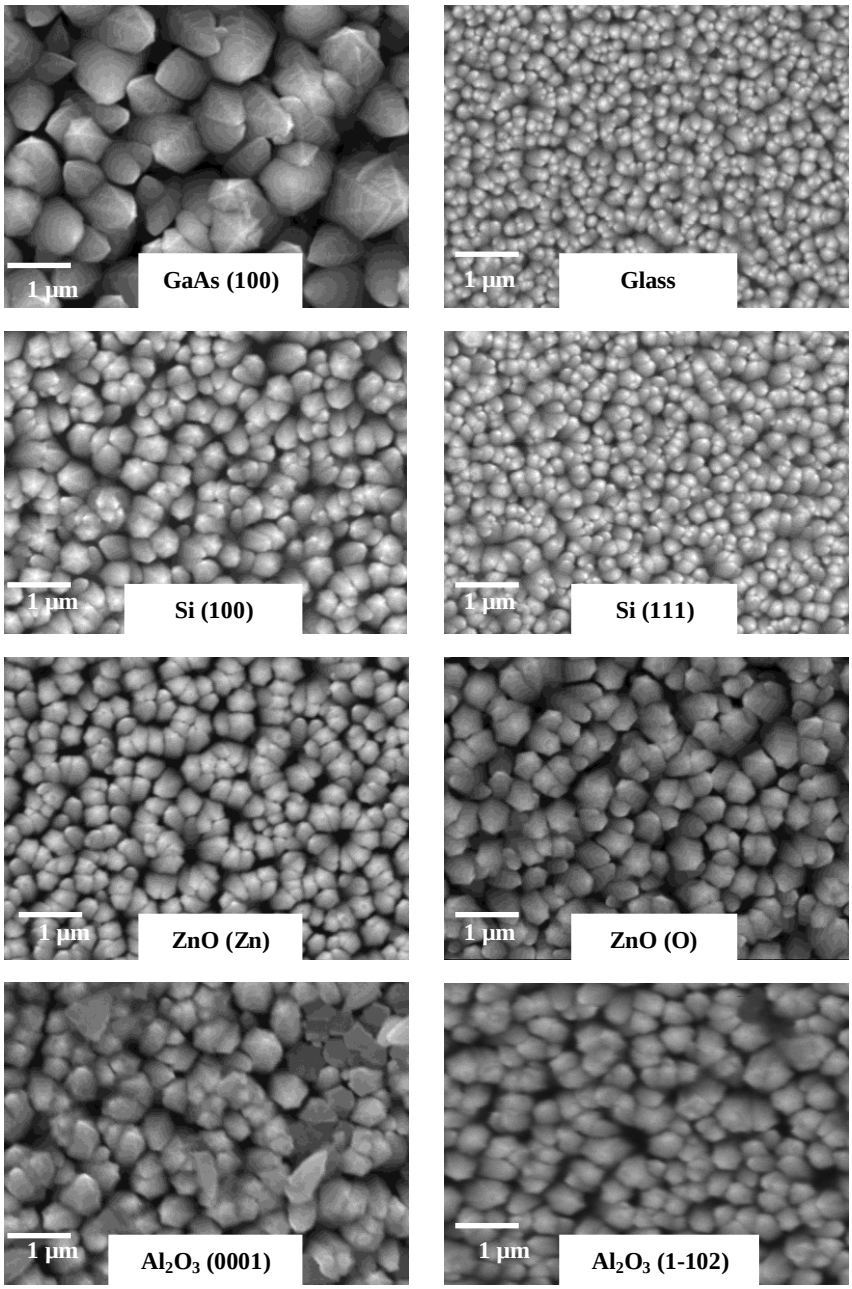

Figure 5-5 SEM images of ZnO films grown on different substrates at 380 ˚C using TBOH as oxidant

the sense that lower mismatch should yield a tendency for the formation of single crystalline, epitaxial films. It seems plausible that, given the rather large lattice mismatch with most substrates used here, the microstructure is not determined by mismatch, but by other factors such as chemical bonding across the interface, residual oxides, substrate morphology, etc.

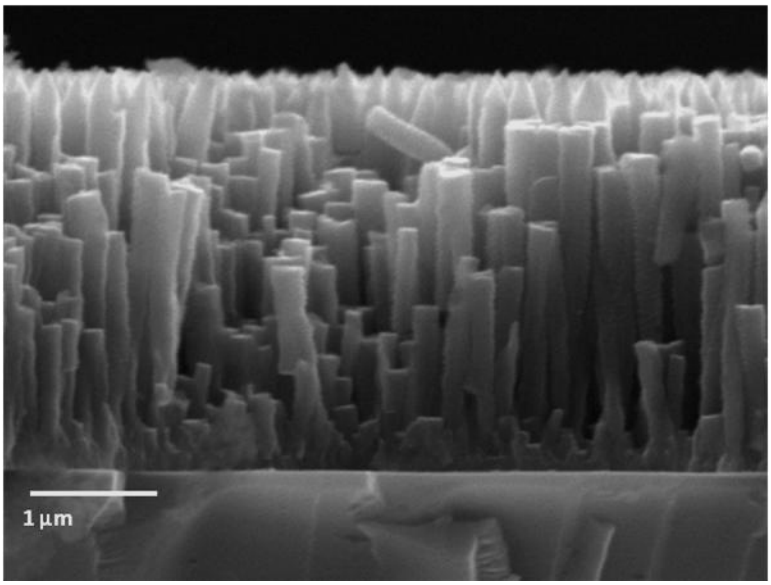

Figure 5-6 Cross-sectional SEM image of ZnO thin film on O-face ZnO substrate

5.2.4 Photoluminescence

Figure 5-7 shows normalized low temperature (11 K) PL spectra of ZnO grown on different substrates. The PL spectra are qualitatively similar, i.e. the same transitions are observed, but with different relative intensities. The NBE emission is dominated by (D°X) recombination around 3.359 eV. The free exciton (FX) appears in some of the samples (for ZnO grown on bulk ZnO and on sapphire) at 3.374 eV, which hints at a relatively low defect/impurity concentration in these samples. The results correlate well with the XRD, in the sense that XRD indicates larger grain size for these substrates, which would imply fewer grain boundaries and structural defects. The insert in Figure 5-7 shows a fit of the NBE emission of the ZnO/GaAs film. Several lines at 3.3649 eV, 3.3624 eV, 3.3596 eV and 3.3568 eV are distinguished. These have been intensively studied by many groups [59, 143, 144, 174]. Meyer *et al.* [59] assigned the lines at 3.3624 eV, 3.3596 eV and 3.3568 eV to hydrogen, gallium and indium impurities, respectively. The line at 3.3649 eV has been ascribed to Zn_i by Sann *et al.* [189]. The FWHM of the dominant line is ~2.2 meV at 11 K, compared to 1.1 meV (at 2.1 K) reported for MOCVD grown ZnO by Kirchner *et al.* [144]. The small FWHM found here indicates the relatively high quality of our material regardless of the substrate.

The peak at ~3.319 eV is ascribed to a (e, A^0) transition, of relatively shallow acceptor states associated with basal plane stacking faults [177]. In ZnO films a high density of stacking faults are often present due to either a translation of the crystal lattice along three equivalent close-packing directions in the (0001) plane or by condensation of vacancies or interstitials to

form dislocation loops, accompanied by partial dislocations [177]. The peak at 3.305 eV is ascribed to donor–acceptor pair (DAP) emission, involving the same acceptor as the (e, A^0) transition [177]. The increase in relative intensity of the stacking fault-related transition for ZnO grown on glass, Si (111) and Si (100) could imply a higher concentration of these defects for growth on these substrates. It is tempting to relate this result to the amorphous nature of glass and the existence of a SiO_x layer on the Si substrate. The amorphous SiO_x could form during the annealing step (in the presence of TBOH). It is expected that nucleation and subsequent evolution of the ZnO will be similar in these three cases. What is not understood at present is the influence of the different substrates on the lateral dimensions of the final columnar structures.

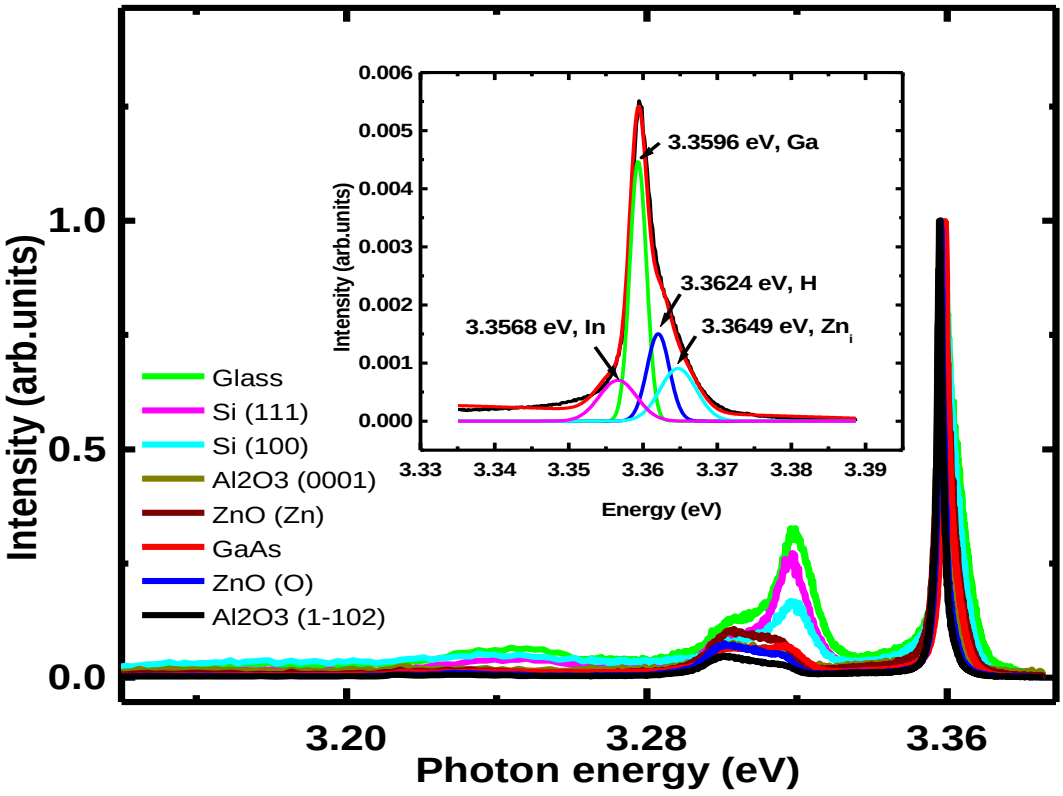

Figure 5-7 Normalized PL spectra (11 K) for ZnO films grown on different substrates. Insert shows a fit of the NBE spectrum of the ZnO/GaAs film

5.3 Conclusions

The growth characteristics of ZnO using oxygen as oxidant have been studied. The effect of the temperature and the VI/II ratio on the morphological and optical properties has been discussed. It has been found that the growth temperature and VI/II ratio strongly affect the growth rate. It was also found that an increase in the growth temperature leads to a morphological change of the layer, from thin film to rods. PL showed a significant increase in the concentration of structural defects for high temperature and high VI/II ratio. The sample grown with a VI/II ratio of 60 and at a growth temperature of 480 ˚C seems to be denser (more compact) and more uniform.

ZnO thin films were also deposited on different substrates (Si, Glass, ZnO and Al_2O_3) using TBOH and the structural, morphological and optical properties have been studied. All the substrates yielded a strong degree of c-axis orientation, with grain sizes (deduced from XRD) being largest for ZnO, sapphire and Si (100) substrate. The surface morphologies were qualitatively similar, with GaAs yielding the largest hexagonal columns (up to 1 µm in diameter). The low temperature PL spectra were also qualitatively similar, although it could be deduced that growth on glass and silicon (both (100) and (111)) yielded higher stacking fault densities in the ZnO films. The results presented on the properties of $Mg_xZn_{1-x}O$ films in the rest of this thesis, were all obtained for growth on Si (100) and c- Al_2O_3.

Chapter 6 Effect of Mg incorporation into ZnO lattice

In this chapter, the influence of Mg incorporation into ZnO on the optical and structural properties of the resulting films is investigated. $Mg_xZn_{1-x}O$ films with different concentrations of Mg are characterized by various techniques, such as XRD, PL, TEM, SEM, and UV-vis absorption measurements. The thin films were grown on c-Al_2O_3 and Si (100) substrates, while varying x_v in the vapour from 0 to 0.6 using either TBOH or O_2 gas as oxidants. Of specific interest is the widening of the band gap, the change in morphology and the possible presence of new defects due to alloying.

6.1 EDX of $Mg_xZn_{1-x}O$ films

For the growth of the alloy, a precise method of evaluating the Mg and Zn composition is important in order to correlate composition with changes in the structural, electrical and optical properties. EDX has been used to estimate the Mg composition in the present study. The Mg composition in the vapour phase is monitored during the MOCVD growth by controlling the source flow ratio. It is worthwhile to note that the Mg concentration is not only affected by the molar flow ratio but also by the growth temperature, the VI/II ratio, the reactor pressure (fixed to ~20 Torr in this thesis), and oxidizing agent. All these parameters are reported in the next chapter, in order to investigate their effects on the Mg incorporation as well as on the properties of the films. This technique does not allow accurate quantitative analysis of the light elements such as oxygen for example, because of a loss in precision.

Figure 6-1 shows a SEM image and EDX measurements in various selected areas of a $Mg_{0.28}Zn_{0.72}O$ film grown on Si (100) substrate at 420 ˚C. The variation is within experimental uncertainty. The values give an average percentage in the chosen area, but does not inform about the location of Mg in the lattice. Also, because of the roughness of certain films, an accurate quantification is quite often difficult.

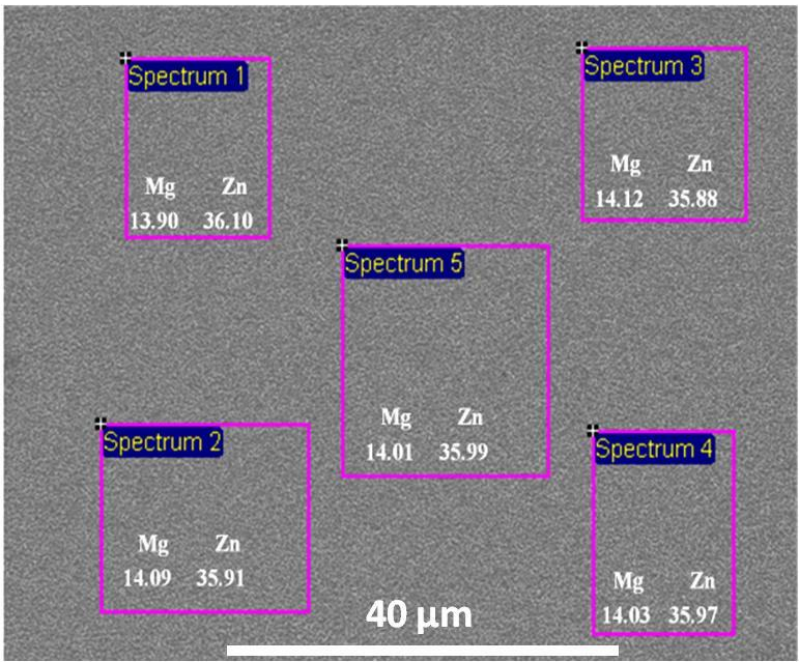

Figure 6-1 SEM image and EDX measurements in various selected areas of a $Mg_{0.28}Zn_{0.72}O$ film grown on Si (100) using TBOH

6.2 Effect of Mg content on the lattice parameters

The growth of ZnO and $Mg_xZn_{1-x}O$ by MOCVD on various substrates at 380 ˚C leads to polar (0001) oriented films. Since, the (0001) plane has the lowest energy amongst all the low-index planes, the growth rate along the c-direction is the highest [190]. Subsequently, the ZnO crystals are elongated in the [0001] direction and the prismatic sides of the crystals are usually the {1010} or {1120} planes. Hence, even under non-epitaxial conditions it is very easy to achieve c-axis oriented films on almost any substrate [91].

Figure 6-2 shows normalized XRD spectra of $Mg_xZn_{1-x}O$ films ($0 \leq x \leq 0.39$) grown on c-Al_2O_3 at 420 ˚C using O_2 as oxidant. The spectra exhibit only the $Mg_xZn_{1-x}O$ (0002) peak for all the samples, except for the film with the highest Mg content of x=0.39. For this sample, a weak peak corresponding to the (10-11) plane of $Mg_xZn_{1-x}O$ is also visible. As the Mg content increases, the (0002) peak shifts towards higher angles, indicating the expected decrease in the *c*-axis lattice constant. This decrease with increasing Mg content is due to the smaller ionic radius of Mg^{2+} compared to Zn^{2+}. The dominance of the (0002) peak shows that the thin films are predominantly oriented with the c-axis perpendicular to the substrate. No evidence of phase segregation was detected for these samples, suggesting that the $Mg_xZn_{1-x}O$ films retain the ZnO wurtzite crystal structure up to $x \leq 0.39$. This is in good agreement with several

reports on $Mg_xZn_{1-x}O$, where the phase segregation was observed to occur around x=0.4 to 0.6 [14, 88, 191, 192].

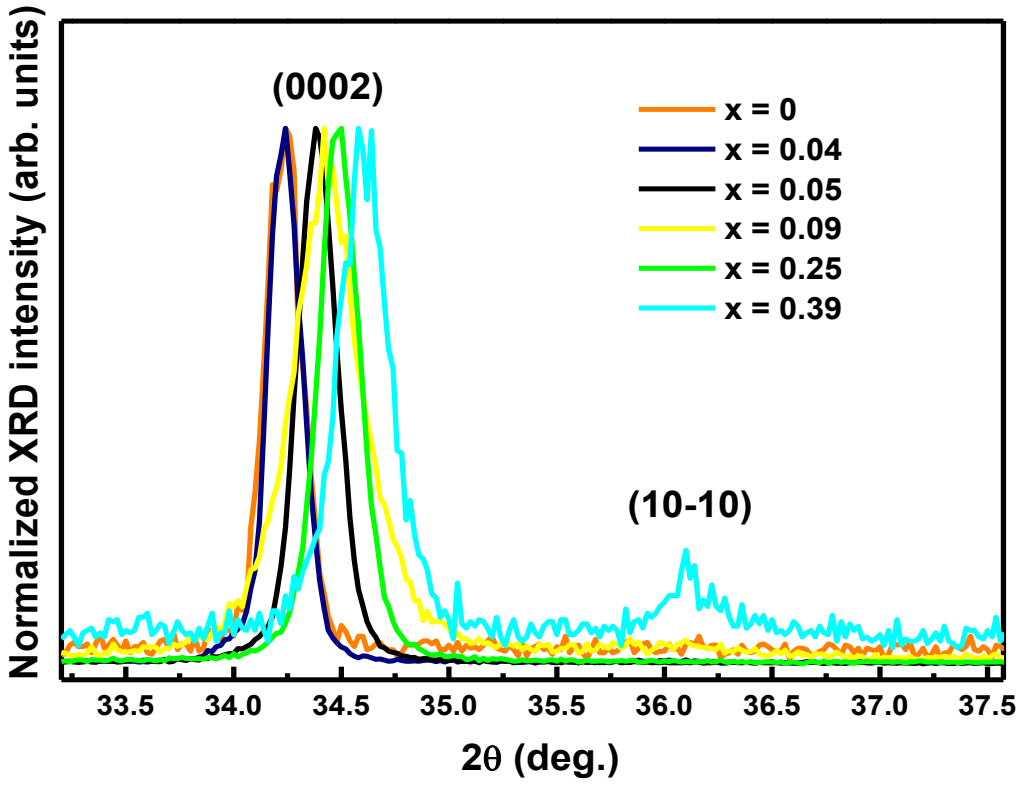

Figure 6-2 Normalized XRD spectra of $Mg_xZn_{1-x}O$ films ($0 \leq x \leq 0.39$) on c-Al_2O_3

The shift in the (0002) peak to higher angles indicates that the Mg atoms substitute on the Zn sites. However, Mg can also occupy interstitial sites, which could cause extended defects, such as dislocations and stacking faults in the layer. The Mg incorporation should also cause a slight increase in the *a*-axis lattice parameter of ZnO depending on the Mg content, but this change cannot be detected in a θ-2θ configuration [15].

Figure 6-3 shows the calculated *c*-axis lattice constant of $Mg_xZn_{1-x}O$ as function of Mg content. The lattice constant was calculated assuming the hexagonal structure for all films, as evidenced by the XRD measurements (with an uncertainty of ±0.002 Å). For comparison, results from Matsumoto *et al.* [193] (MBE) and Ashrafi *et al.* [16] (MOCVD) are also plotted. Our data correlates well with the other published data. As expected, the *c*-axis lattice parameter decreases with increasing Mg content. Overall, the decrease is very small in this composition range (~0.6%), confirming that wurtzite $Mg_xZn_{1-x}O$ films are almost lattice matched to ZnO.

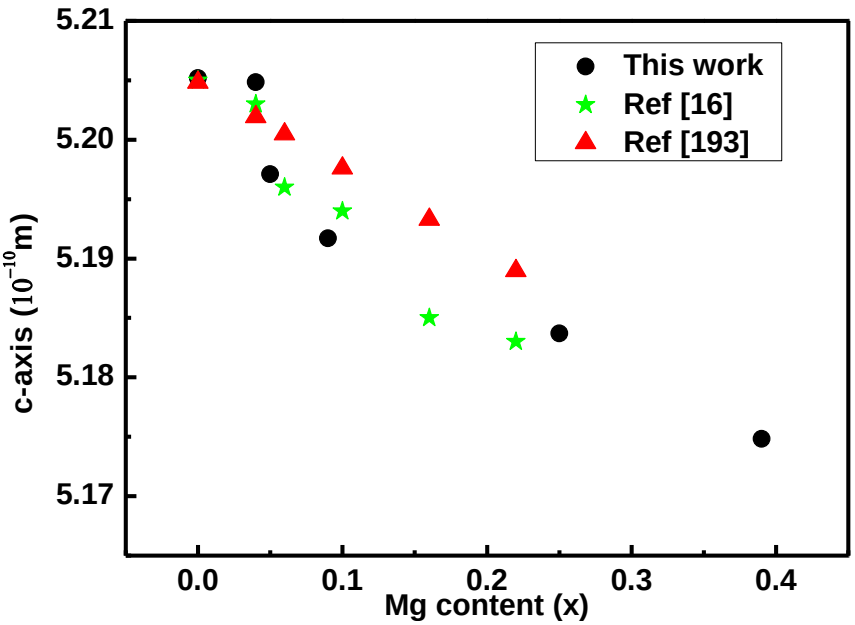

Figure 6-3 Mg concentration dependence of the c-axis lattice constant of $Mg_xZn_{1-x}O$ ($0 \leq x \leq 0.39$) films grown on c-Al_2O_3

A further increase in the Mg content to x=0.45 leads to an additional peak at 36.44˚ (Figure 6-4), which is very close to the (111) diffraction peak of MgO [120]. The appearance of the (0002) ZnO peak and the (111) MgO peak indicates the occurrence of phase segregation. The intensity of the cubic $Mg_xZn_{1-x}O$ (111) peak is stronger than that of hexagonal $Mg_xZn_{1-x}O$ (0002). This indicates clearly the transformation from wurtzite to cubic structure, which correlate well with the broadness of the UV transmission for x_v=0.5 (see figure 4.7).

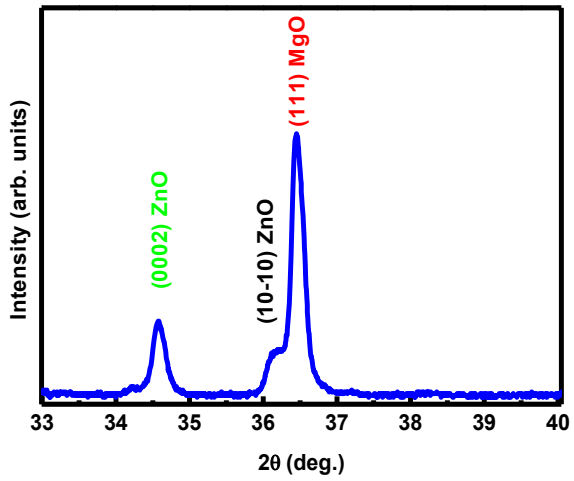

Figure 6-4 XRD spectra of a $Mg_{0.45}Zn_{0.55}O$ film grown on c-Al_2O_3 at 420 ˚C

6.3 Effect of Mg incorporation into ZnO films grown using TBOH

Morphology

Figure 6-5 shows SEM images of films grown with different Mg content in the vapour phase. For low Mg content (Figure 6-5(a) and (b) ($x \leq 0.05$)) the surface morphology remains similar to that of ZnO. The films exhibit columnar, hexagonal crystallites with cone shaped ends. It is worthwhile noting that the columnar structure may lead to structural, chemical, and electrical anisotropy and to rapid diffusion of impurities along the grain boundaries [194]. For higher Mg content ($x \geq 0.23$) (Figure 6-5(c) and (d)) the morphology changes drastically, hinting at structural changes from wurtzite structure to a mixture of wurtzite and cubic phases. For the sample grown with x=0.61 (Figure 6-5(d)), clear evidence exists for the formation of a cubic phase, since pyramidal crystallites with a square/rectangular base are observed. Han *et al.* [195] reported similar morphologies for their cubic $Mg_xZn_{1-x}O$ (≥ 0.5) films deposited on Al_2O_3 substrate by magnetron sputtering.

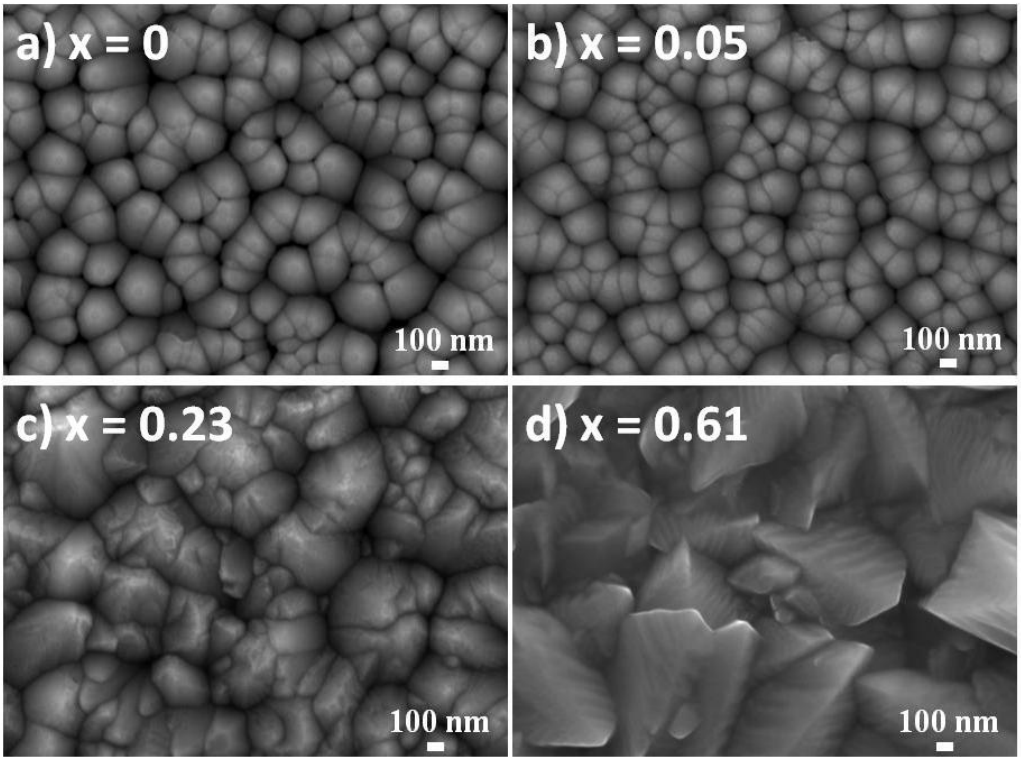

Figure 6-5 Top view SEM images of $Mg_xZn_{1-x}O$ films grown with different Mg vapour phase concentrations on c-Al_2O_3 using TBOH as oxygen source: (a) x=0, (b) x=0.05, (c) x=0.23 and (d) x=0.61

Auger spectroscopy

Figure 6-6 shows SEM images and scanning Auger microscopy (SAM) images of the Mg distribution of the different elements present in two $Mg_xZn_{1-x}O$ films with x_v=0.2 (x=0.08) and 0.6 (x=0.61). The locations of the Zn and Mg atoms are illustrated in the coloured map. For x=0.08, the SAM image shows a fairly uniform Mg distribution on the sample surface. For x=0.61 an accumulation of Mg is evident in between the big crystallites. The Mg distribution appears more non-uniform than Zn. The surfaces of the larger crystals have a low Mg content.

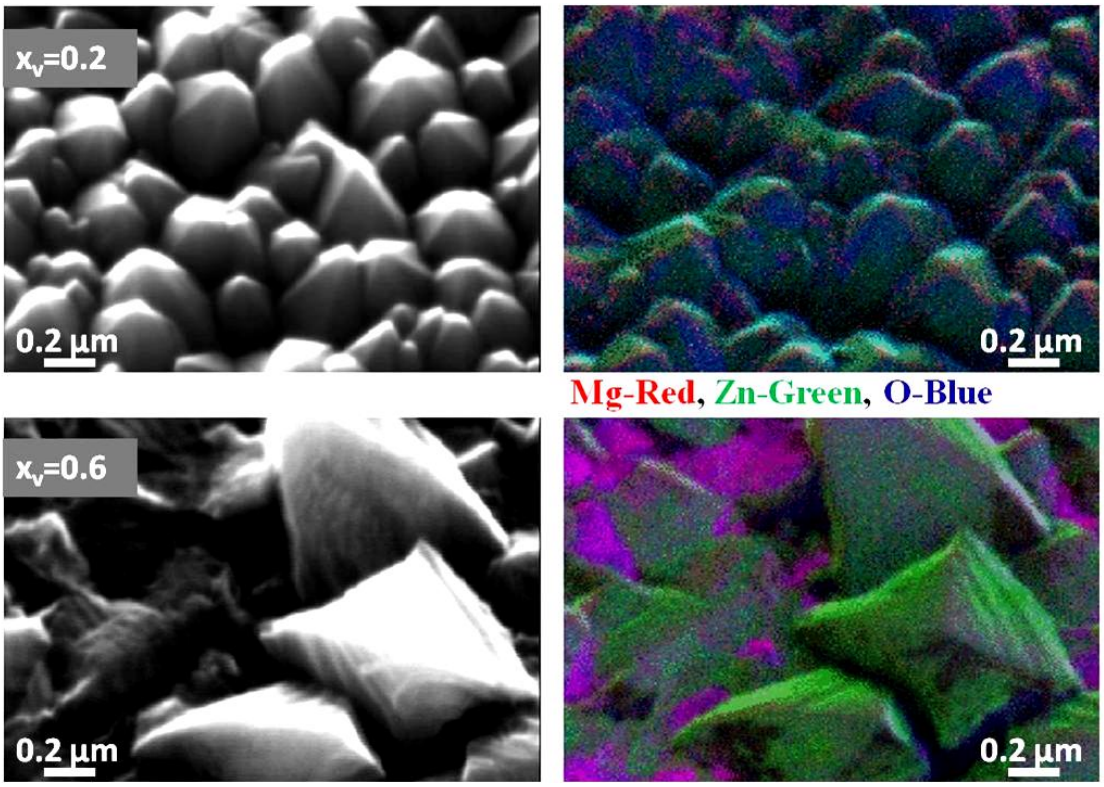

Figure 6-6 $Mg_xZn_{1-x}O$ (x_v=0.2) and (x_v=0.6) SEM images and corresponding compositional SAM map (Red-Mg, Green-Zn, and Blue-O)

Photoluminescence

Figure 6-7 shows 4.2 K PL spectra of a series of $Mg_xZn_{1-x}O$ films grown using TBOH with different x_v (0, 0.05, 0.1, 0.15, 0.2 and 0.3). In most cases, three dominant transitions are seen. The red arrow points to the donor bound exciton D^oX line, while the black arrow points to the (e, A^0) line (seen in ZnO at 3.31 eV). The third peak is a phonon replica of the (e, A^0) transition. When Mg is incorporated, the main D^oX line shifts toward higher energies, implying that the band gap increases with Mg content, as expected. The D^oX line shifts from

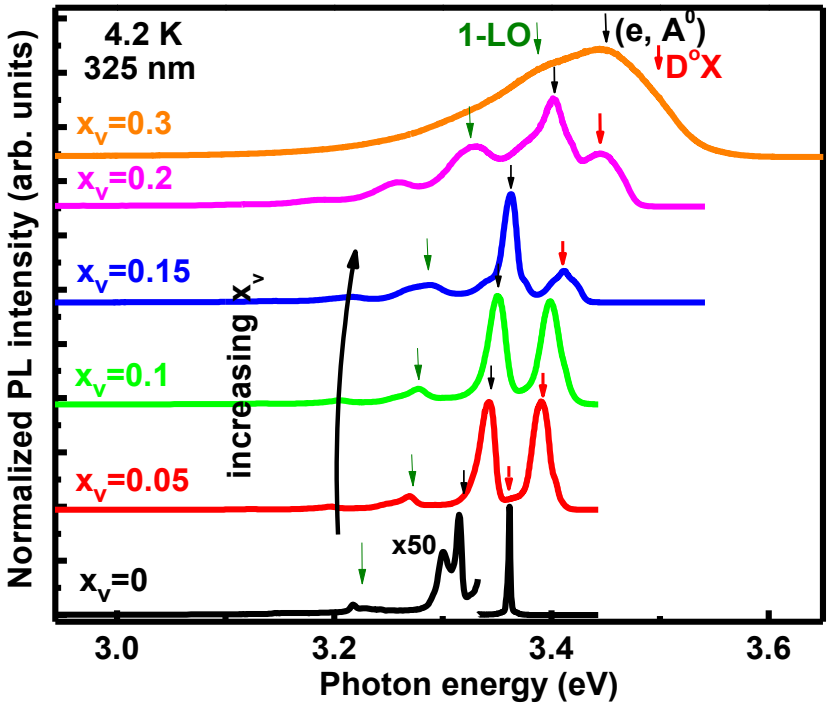

Figure 6-7 Low temperature (4.2 K) PL spectra of ZnO and $Mg_xZn_{1-x}O$ films on c-Al_2O_3 with x_v=0.05, 0.1, 0.15, 0.2 and 0.3

3.361 eV to ~ 3.50 eV and is accompanied by a substantial increase in the FWHM (from 1.8 meV for ZnO to ~82 meV for x_v=0.3). The peaks at 3.315 eV and 3.300 eV from the ZnO sample (x_v=0) are ascribed to stacking faults, as discussed earlier, and their phonon replicas also shift to higher energy as x_v increases. Besides the blue-shift of the main D^oX line, all the other transitions associated with specific defects also shift due to the band gap increase. If it is assumed that the defect responsible for the D^oX in the ZnO spectrum is the same as in the $Mg_xZn_{1-x}O$ films, it seems likely that the impurity is Al [59]. It is noted that the (e, A^0) emission increases in intensity upon an increase in x_v and surpasses the D°X transition for $x_v \geq 0.10$. For 30% Mg vapour content, due to alloy broadening, the (e, A^0) and D°X strongly overlap, giving rise to a broad band. The increase in the stacking fault density could be due to the fact that when Mg substitutes the Zn, it creates more distortion/disorder in the lattice. For both (e, A^0) and D^oX transitions, the FWHM substantially increase with x_v. Park *et al.* [93] explained this increase as resulting from fluctuations in alloy composition, where localized excitons experience a different Coulomb potential. The influence of various broadening mechanisms on the PL linewidth will be discussed in more detail in section 6.6.3.

Figure 6-8 shows normalized RT PL spectra of $Mg_xZn_{1-x}O$ films with x_v ranging between 0 and 0.6. Where available, the mole fraction x in the solid is also given in brackets. The NBE

emission blue shifts upon an increase in the Mg concentration in the vapour phase. At RT, the NBE emission is generally assumed to be dominated by free excitonic (FX) recombination [93,196-200]. Therefore, assuming that the dominant PL peak at RT is due to FX emission, the blue shift confirms an increase in the band gap energy due to an increase in Mg content in the various films. Similar to what is observed at low temperature, the linewidth of the dominant peak broadens as the Mg content increases. The broadening of the peaks result from alloying, inhomogeneous strain, dislocations and finite domain size causing potential fluctuations in the band edges [201]. The alloy disorder in $Mg_xZn_{1-x}O$ is for the most part due to the large band gap difference between ZnO and MgO. Inhomogeneous strain, caused by a lack of film homogeneity, is believed to degrade the opto-electronic quality of the films and to cause the broadening of the XRD and PL peaks in ZnO, for example [202], and also can randomly and locally modify the band gap energy [203]. It should also be noted that the range of values of the FWHM (50-220 meV $0 \leq x \leq 0.61$) (Figure 6-9) compares favourably to reported values for films deposited by molecular beam epitaxy (120-230 meV $0 \leq x \leq 0.39$) [204] showing that for similar Mg incorporation the samples grown by MOCVD are of compatible quality.

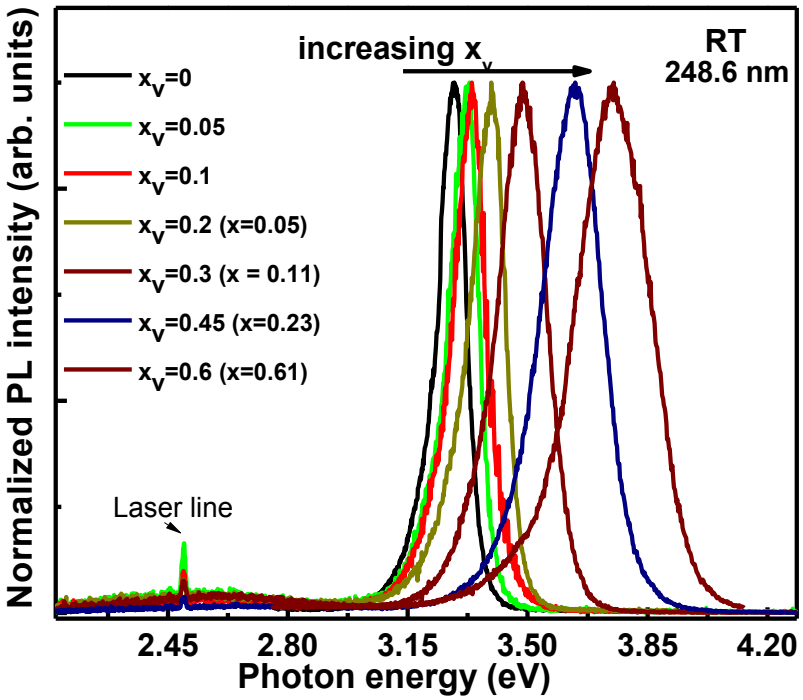

Figure 6-8 RT PL spectra of ZnO and $Mg_xZn_{1-x}O$ films grown on c-Al_2O_3 using TBOH as oxidizing agent

Figure 6-9 shows the PL peak energy, illustrating an increase of 450 meV in the range $0 \leq x \leq 0.61$. The shift in the PL peak position follows the same trend as the transmission measurements (see section 4.7). The shift in the PL peak position confirms the possible use of $Mg_xZn_{1-x}O$ in deep UV optoelectronic devices.

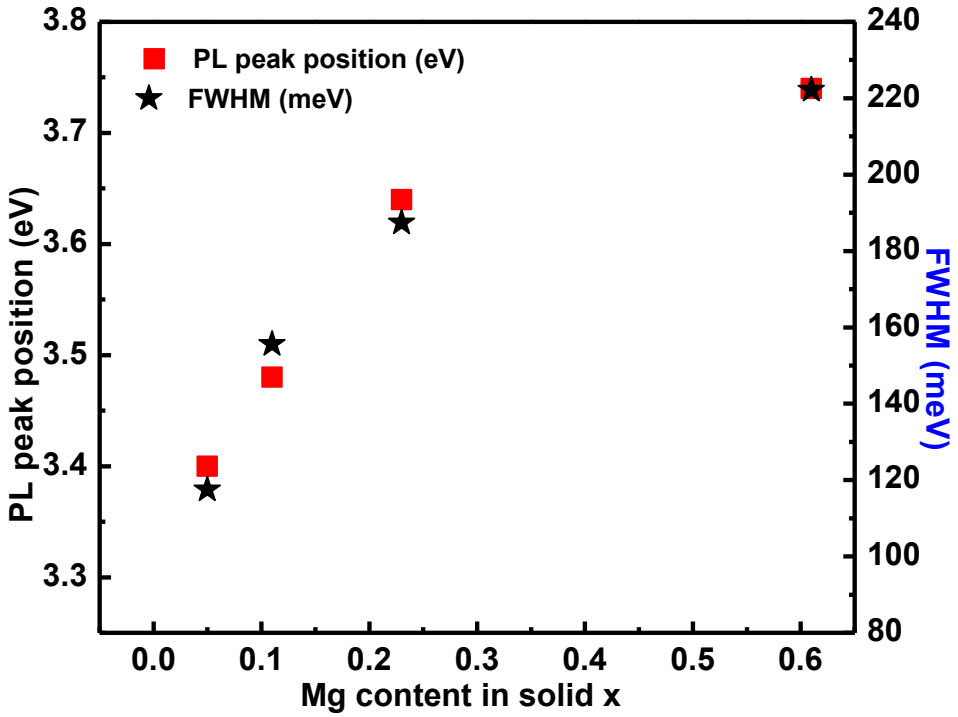

Figure 6-9 Variation in RT PL peak position and FWHM of $Mg_xZn_{1-x}O$ thin films with Mg content

Absorbance

Figure 6-10 shows the RT optical absorbance spectra of $Mg_xZn_{1-x}O$ films deposited on c-Al_2O_3 with different Mg mole fraction in the solid at a constant growth temperature of 420 ˚C and constant VI/II ratio of 60, using TBOH as oxidant. It can be seen from this figure that as the Mg content increases, the absorption edge moves towards higher energies. This indicates an increase in the band gap (E_g) of the material. With increasing Mg content from 0 to 0.43, the cut–off wavelength shifts from ~374.4 nm to ~346.2 nm. For the highest Mg composition, a broadening in the absorption edge is observed, which is attributed to the formation of a Mg-rich phase [93]. Alloy broadening is another cause of broadening of the absorption edge [205].

Reports on evolution of the band gap of $Mg_xZn_{1-x}O$ as function of Mg content show various results [28, 199, 206]. The increase in direct band gap with Mg composition in $Mg_xZn_{1-x}O$

thin films has been quoted in Ref. [15, 186] as: $E_g(Mg_xZn_{1-x}O) = 2.48x + 3.32$ eV. Meanwhile, Chen *et al.* [191] have summarized approximately the dependence of the band gap energies for Mg content varying from 0 to 0.82. They showed that the band gap follows two different linear relationships, one for the hexagonal (wurtzite) phase [$E_g(Mg_xZn_{1-x}O) = 3.32 + 2.00x$ ($0 \leq x \leq 0.33$)] and the other for the cubic phase [$E_g(Mg_xZn_{1-x}O) = 3.02 + 4.03x$ ($0.45 \leq x \leq 0.82$)].

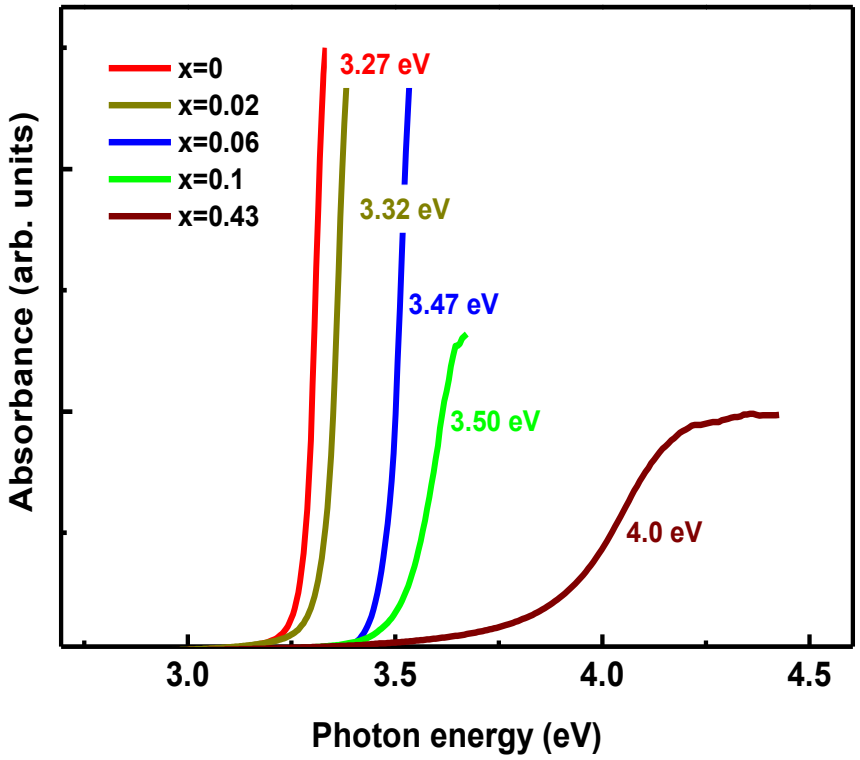

Figure 6-10 RT Optical absorbance spectra of $Mg_xZn_{1-x}O$ grown on c-Al_2O_3 (x=0, 0.02, 0.06, 0.1 and 0.43)

Figure 6-11 shows a comparison of the energies extracted from Figure 6-10 as function of x, with the reported band gap variation from Ref. [186]. As reported in Ref. 199 and 207-209, the band gap depends linearly on the Mg content. Ashrafi *et al*. [16], however, established a non-zero bowing parameter b [$E_g = xE_{ZnO} + (1-x)E_{MgO} - bx(1-x)$] for both $Mg_xZn_{1-x}O$ and for $Cd_xZn_{1-x}O$. It should be noted that for high Mg content, the determination of the band gap remains difficult. This is due to phase segregation between MgO and ZnO occurring at high Mg incorporation. A large range of values has been reported for the band gap in the range $0.6 \leq x \leq 1$ [15, 91, 186, 210].

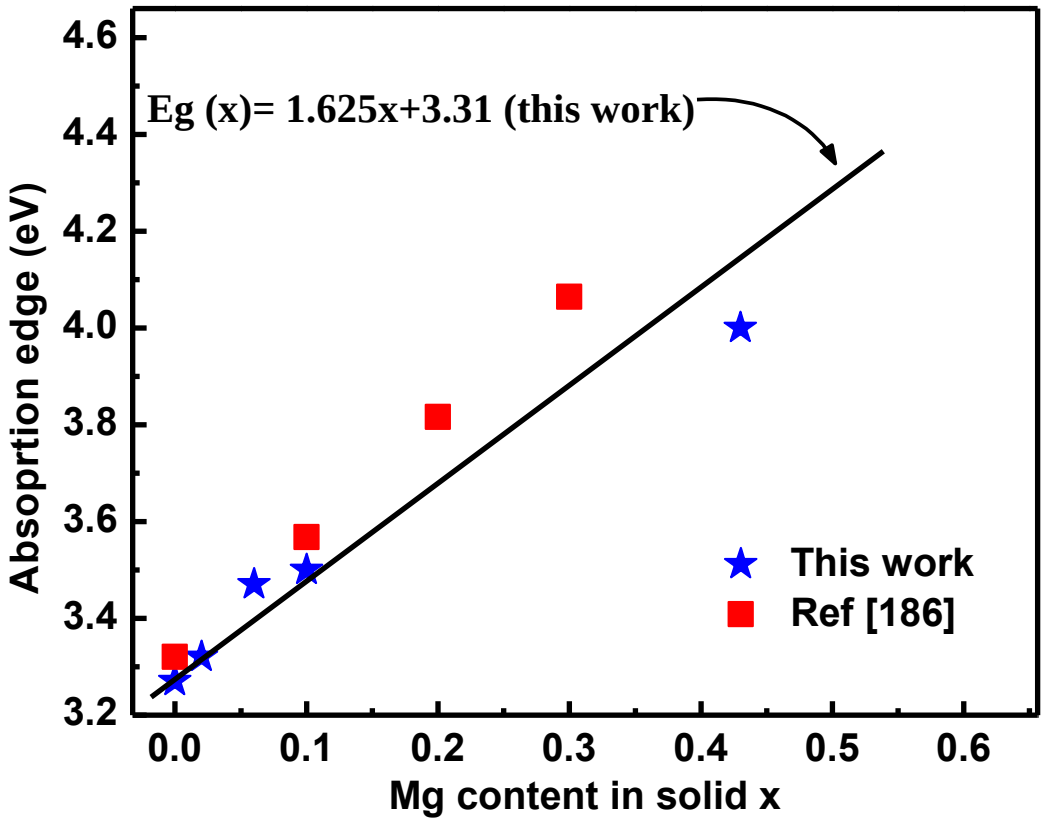

Figure 6-11 Variation of energy band edge as the function of x Mg vapour content with data taken from Ref. [186]

6.4 Effect of Mg incorporation on films grown using O_2

Morphology

Figure 6-12 shows SEM images of films grown on c-Al_2O_3 using oxygen gas with different Mg mole fractions in the solid (x=0, 0.09, 0.25 and 0.39). The growth temperature was 420 ˚C and the VI/II ratio 60. For low Mg content x≤0.09, the surface is characterized by relatively uniform hexagonal shaped crystallites. For high Mg content (x=0.25 and 0.39), the surface morphology changes. This change in morphology is similar to what was observed in the previous section when TBOH was used as oxidant. From the cross-sectional views, it was observed that these films also grew in a columnar fashion. Hexagonal shaped crystallites with cone shaped ends were evident for x≤0.09, resulting from the higher growth rate in the c-axis direction, while for a higher Mg content the film comprises large irregularly shaped crystals on an underlying layer of small densely-packed crystallites.

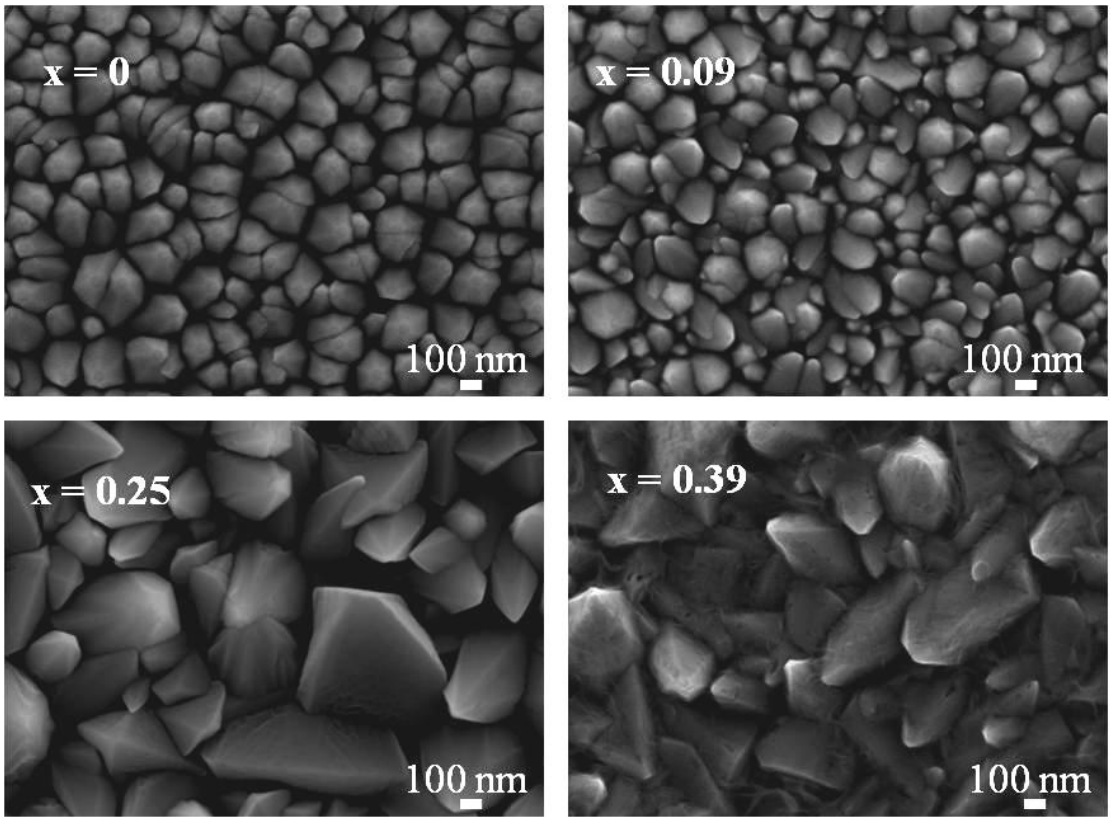

Figure 6-12 Top view SEM images of $Mg_xZn_{1-x}O$ films grown with different Mg concentrations on c-Al_2O_3 using O_2 gas as oxygen source

Structural characterization

Figure 6-13 shows cross sectional bright-field TEM micrographs of a $Mg_{0.01}Zn_{0.99}O$ film grown on c-Al_2O_3 at 420 ˚C, with a VI/II ratio of 60 and using oxygen gas as oxidant. In our reactor, under the present growth conditions, textured films comprising columnar grains with the c-axis perpendicular to the substrate, as illustrated in this image, are obtained for a Mg content up to ~0.2. This columnar growth propagates from an intermediate layer of seed crystals near the interface. In addition, the high magnification TEM image shows the presence of a high density of stacking faults (indicated by brackets). A similar trend was observed for growth on silicon substrate.

Figure 6-14 shows a high resolution cross-sectional TEM image of the interface between the c-Al_2O_3 substrate and the $Mg_{0.01}Zn_{0.99}O$ film. This image confirms the formation of randomly oriented crystallites at the surface of the substrate, which lead to the evolution of columnar structures. The columns grow preferentially along the <0001> direction.

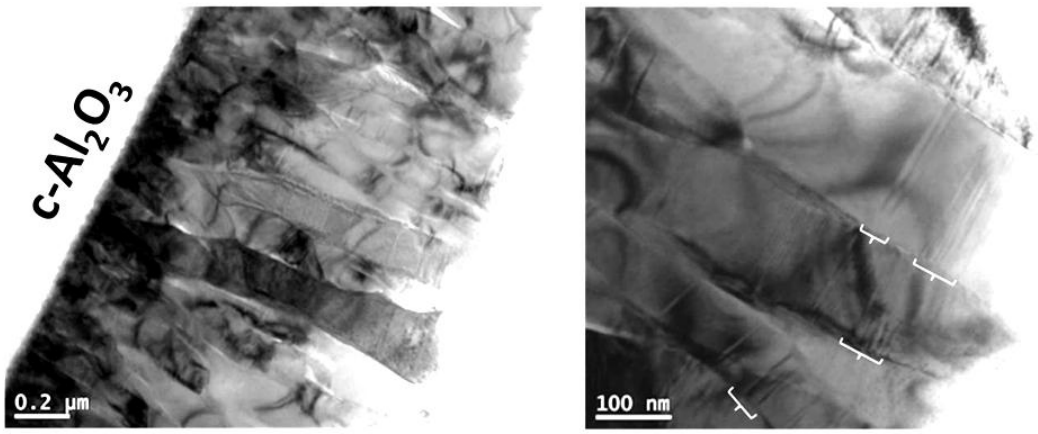

Figure 6-13 Cross-sectional TEM micrographs of $Mg_{0.01}Zn_{0.99}O$ film grown on c-Al_2O_3

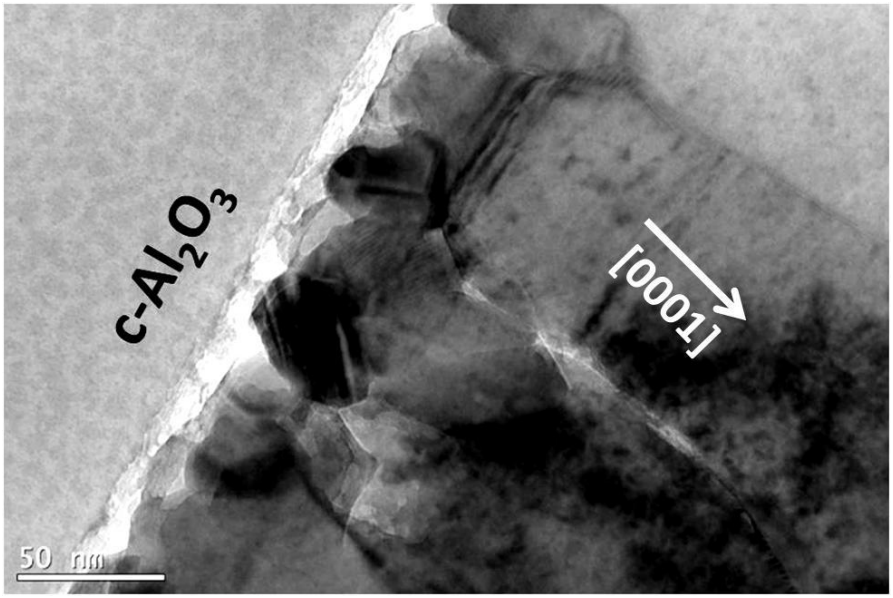

Figure 6-14 Cross sectional HRTEM micrograph of the interface between $Mg_{0.01}Zn_{0.99}O$ and c-Al_2O_3

The interface between Al_2O_3 and $Mg_xZn_{1-x}O$

To further explore the interface between the substrate and film, high resolution TEM was performed. Figure 6-15 shows a micrograph taken from a $Mg_{0.09}Zn_{0.91}O$ film along the [10-10] zone axis. A well-defined interfacial layer (~2 nm thick and indicated by a rectangle) can be clearly seen between the layer and the substrate. The inset on the left is the selected-area diffraction pattern (SADP) from the Al_2O_3 substrate, while the one on the right is from the layer. It shows the orientational relationship between the film and the substrate: $Mg_xZn_{1-x}O$ (0001) [21-10]//Al_2O_3 (0001) [10-10].

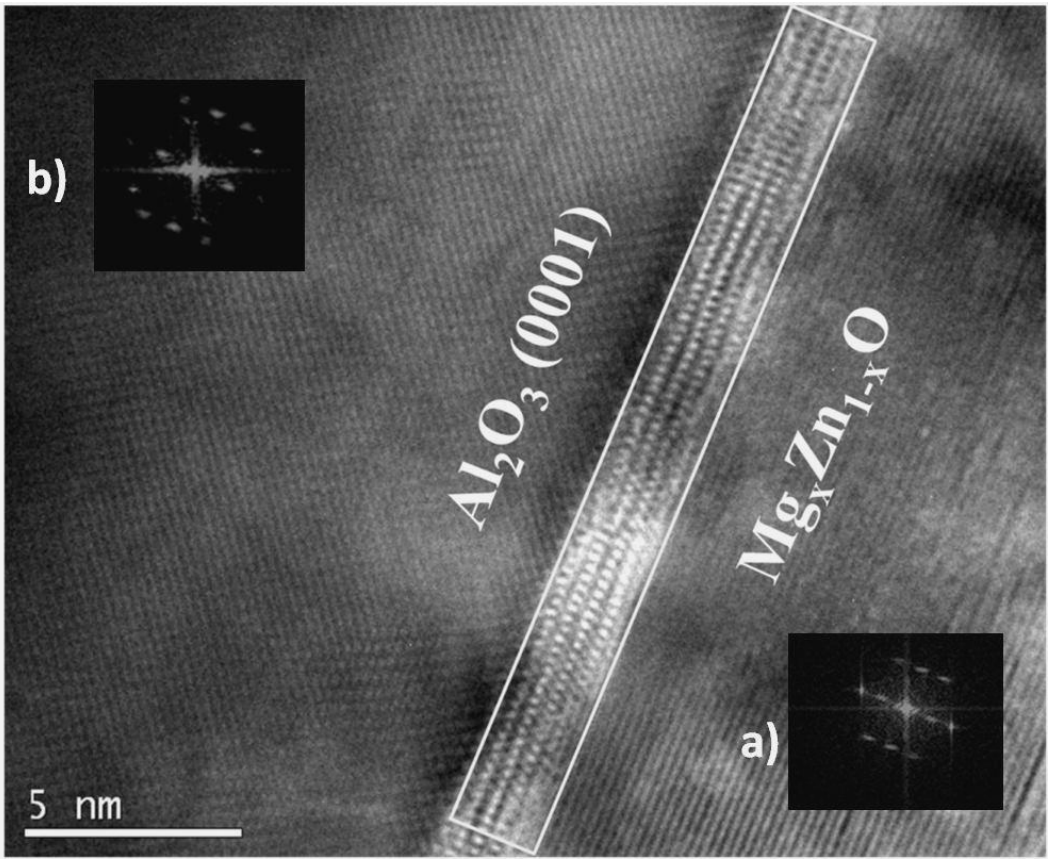

Figure 6-15 Cross sectional HRTEM image of $Mg_{0.09}Zn_{0.91}O$ thin film grown on Al_2O_3. The rectangle shows the interfacial layer between the Al_2O_3 and the film. (a) & (b) are SADPs

SAM elemental maps of the surface and a cross section of the film were also obtained. Figure 6-16 shows the elemental distributions of magnesium, zinc, oxygen and aluminium in a cross-section of the $Mg_{0.09}Zn_{0.91}O$ film. An increased brightness of a specific colour indicates an increased concentration of the relevant element. One can clearly see that the distribution of Zn is fairly uniform with some degree of diffusion into the substrate. A significant accumulation of Al, O and Mg is evident at the interface between the layer and the Al_2O_3. The magnesium distribution appears uniform throughout the rest of the film. It is observed that magnesium and aluminium also diffuse: the former is detected in the substrate, while significant signals from aluminium are detected from the film. This has been independently confirmed by EXD line scans across the interface (Figure 6-17) and AES spot scans on the film and substrate. However, it is worthwhile noting that the thickness of the Mg-enriched region seen in SAM and EDX is larger than the interfacial layer observed in the HRTEM image. The surface AES map measured for Mg, Zn and O for this specific sample shows an essentially uniform distribution of the elements. Similar results have been obtained for other

samples with relatively low Mg content. However, for samples with Mg content larger than ~0.2, the surface distribution of Mg was found to be highly non-uniform.

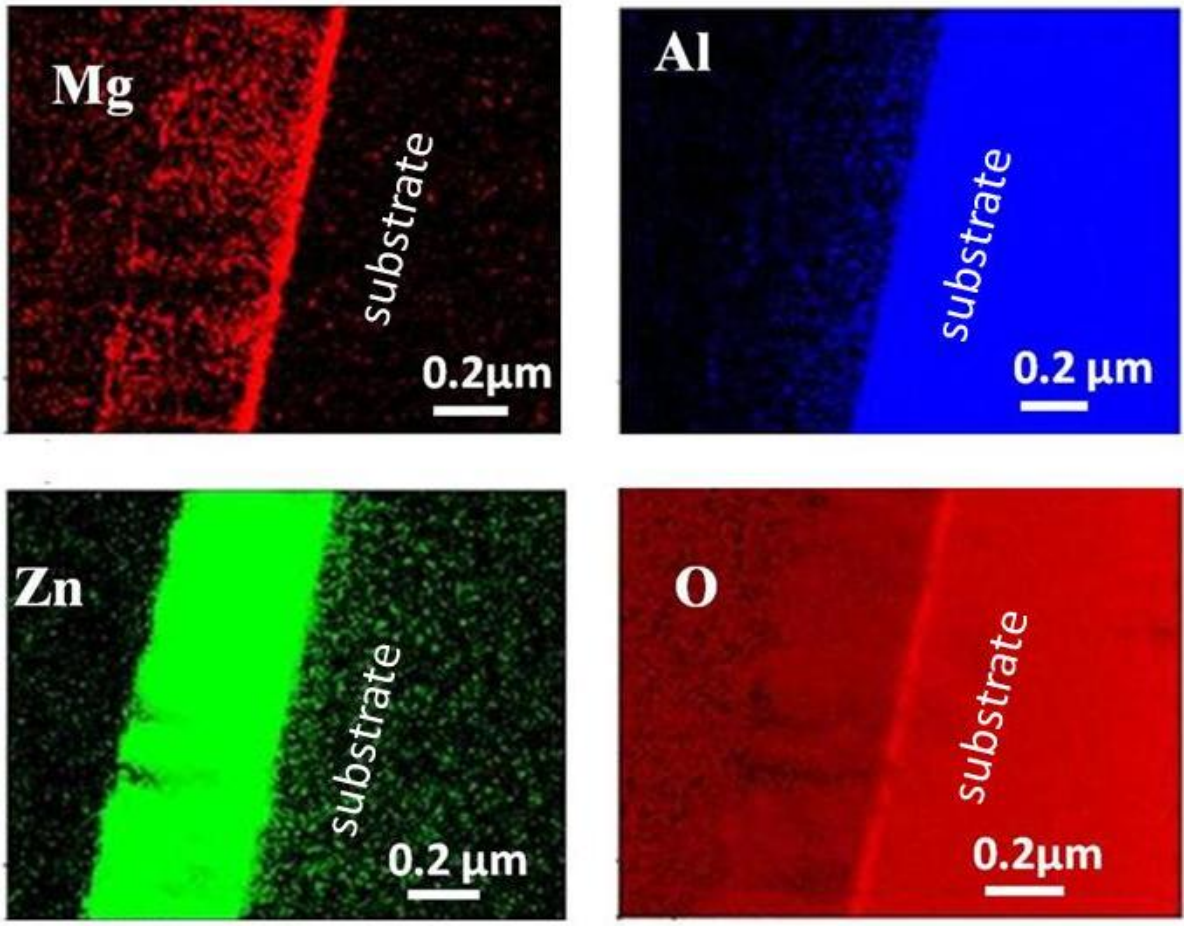

Figure 6-16 SAM images showing the elemental distribution in a cross–section of a $Mg_{0.09}Zn_{0.91}O$ thin film on c-Al_2O_3

Figure 6-18 shows a SAM image of the elemental distribution in a cross–section of a $Mg_{0.09}Zn_{0.91}O$ film grown on Si (100) under the same condition as the one grown on c-Al_2O_3. Again an interfacial region between the layer and the substrate is seen. This region is rich in Mg, as was the case for the film grown on sapphire substrate. Throughout the rest of layer the Mg content remains fairly uniform.

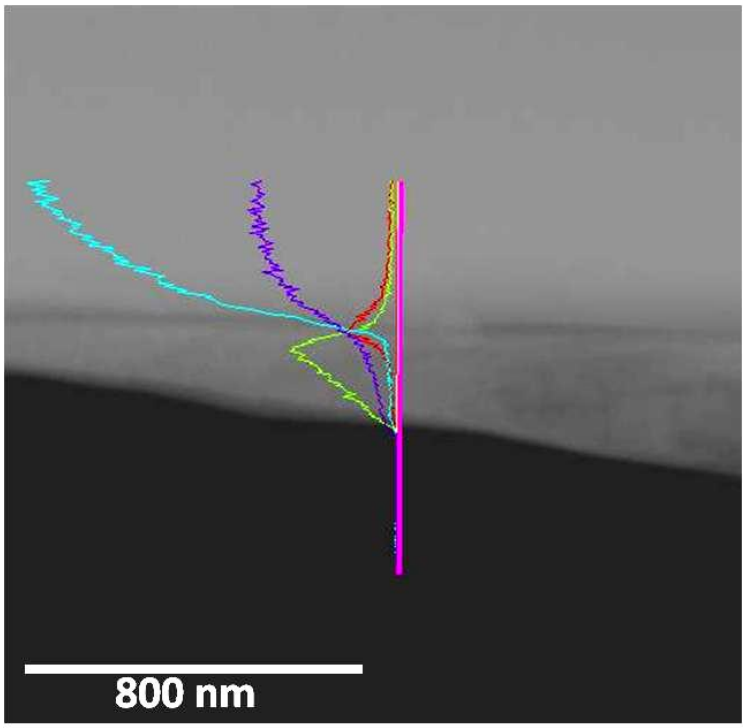

Figure 6-17 Concentration profiles of Mg (red), Zn (green), Al (violet) and O (cyan) obtained from EDX line scans in a TEM along the line indicated by the horizontal magenta line of $Mg_{0.09}Zn_{0.91}O$ *on c-*Al_2O_3

The presence of an interfacial layer will strongly affect the evolution of the subsequent film. It is known that an increase in Mg content in the film could lead to the segregation of phases, even to a complete change from the wurtzite to the cubic structure, as observed and reported by several groups [191, 211, 212]. The TEM observation of an unidentified interfacial layer having a structure different from that of the film, as well as the consistent presence of Mg, Al and O accumulated at the interface, leads to the following interpretation: it seems reasonable to assume that the initial nucleation stage changes with increasing Mg content. For low Mg content, the nucleation phase could keep the wurtzite structure, while for high Mg content the nucleation phase could change to a thermodynamically more favoured cubic structure. This will strongly influence the subsequent evolution of the film. It should be pointed out that the presence of Al in the interfacial layer is due to the Al_2O_3 substrate used here. Deposition on Si leads to a magnesium enriched interfacial layer, as observed by AES (Figure 6-18). Although we have not been able to identify the interfacial layer shown in Figure 6-16, it is suggested to be a spinel, $MgAl_2O_4$. The formation of $MgAl_2O_4$ at the interface between $Mg_xZn_{1-x}O$ (grown by plasma-assisted molecular beam epitaxy) and c-Al_2O_3 has been reported by Vashei *et al.* [212]. The formation of a spinel ($Mg_{2-x}Zn_xTiO_4$) at the interface

between $Mg_xZn_{1-x}O$ and TiN substrate has also been reported in Ref. [4]. Furthermore, growth of MgO on c-Al_2O_3 substrate has been shown to produce a thin $MgAl_2O_4$ layer by a solid state reaction at 475 ˚C. Subsequently, the overgrown $Mg_xZn_{1-x}O$ layer will tend to follow the initial structure at this interface [213].

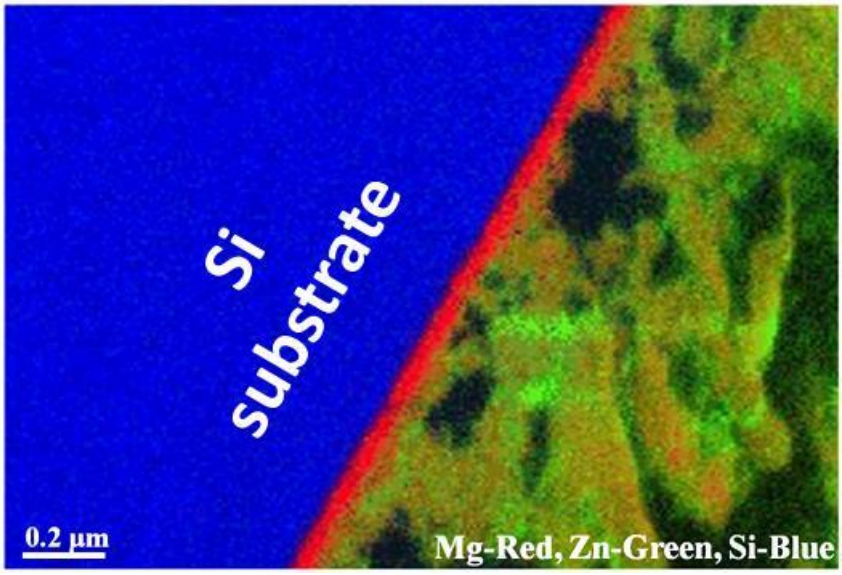

Figure 6-18 SAM image showing the elemental distribution in cross-section of a $Mg_{0.09}Zn_{0.91}O$ thin film on Si (100).

Photoluminescence

Figure 6-19 shows the low temperature (4.2 K) PL spectra of ZnO and $Mg_xZn_{1-x}O$ films with different Mg solid composition, grown using oxygen gas. As for the samples grown using TBOH, the spectra show three dominant transitions, which correspond to the same defects/impurities discussed before. The black arrows point to the D^oX line, which shifts to higher energy due to an increase in the band gap energy. The grey arrows indicate the (e, A^0) transition, which increases in relative strength as the Mg content increases. The shoulder on the higher energy side of the D^oX line is assigned to a D^+X transition. Already for x=0.04 the spectrum broadens to such an extent that an unambiguous identification of the lines is difficult. An increase in Mg content does not seem to change the energy separation between (e, A^0) and its phonon replicas, indicated by blue stars on the spectra.

For both sources the stacking fault related transition increases with Mg content. The spectra have the same PL features and exhibit the same defect-related emission.

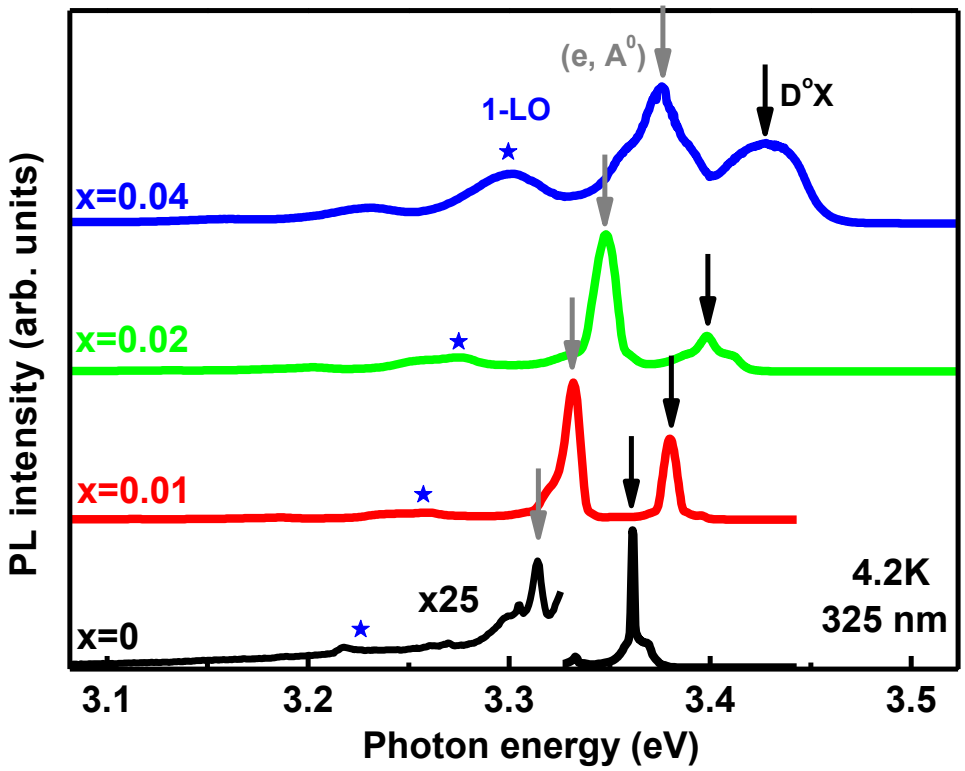

Figure 6-19 Low temperature (4.2 K) PL spectra of $Mg_xZn_{1-x}O$ ($0 \leq x \leq 0.04$) films grown on c-Al_2O_3 at 420 ˚C and VI/II ratio=60.

Figure 6-20(a) shows the normalized RT PL spectra of $Mg_xZn_{1-x}O$ ($0 \leq x \leq 0.39$) films grown on *c*-Al_2O_3. The dominant peak, assumed to be the FX transition, shifts to higher energy as the Mg content increases, due to the increase in the band gap energy. For x=0.25, the shoulder appearing on the lower energy side is assigned to the (e, A^0) transition and was confirmed by temperature dependent PL measurement. The broad dominant peak, observed for x=0.39 could be a combination of the FX and (e, A^0) transitions. Furthermore, for this specific sample, a low energy shoulder coinciding with the FX position in ZnO is also observed, in addition to a transition appearing on the high energy side of the dominant peak. Possibly, three different regions co-exist in this sample. In other words, a pure ZnO region gives rise to the FX appearing as the shoulder on the lower energy side of this spectrum. In addition, the FX + (e, A^0) transitions, dominant in this spectrum, could be from a "Mg poor region" and the shoulder on the high energy side from a "Mg rich region". This could be due to the formation of an interfacial layer during the initial growth stage, which could strongly affect the optical properties for high Mg content. Matsui *et al.* [214] reported the same behaviour in their samples, where they found a Mg rich and Mg poor region for x=0.37,

which gave rise to band-edge emission at 4.0 and 3.7 eV, respectively. Similar results have been reported in the

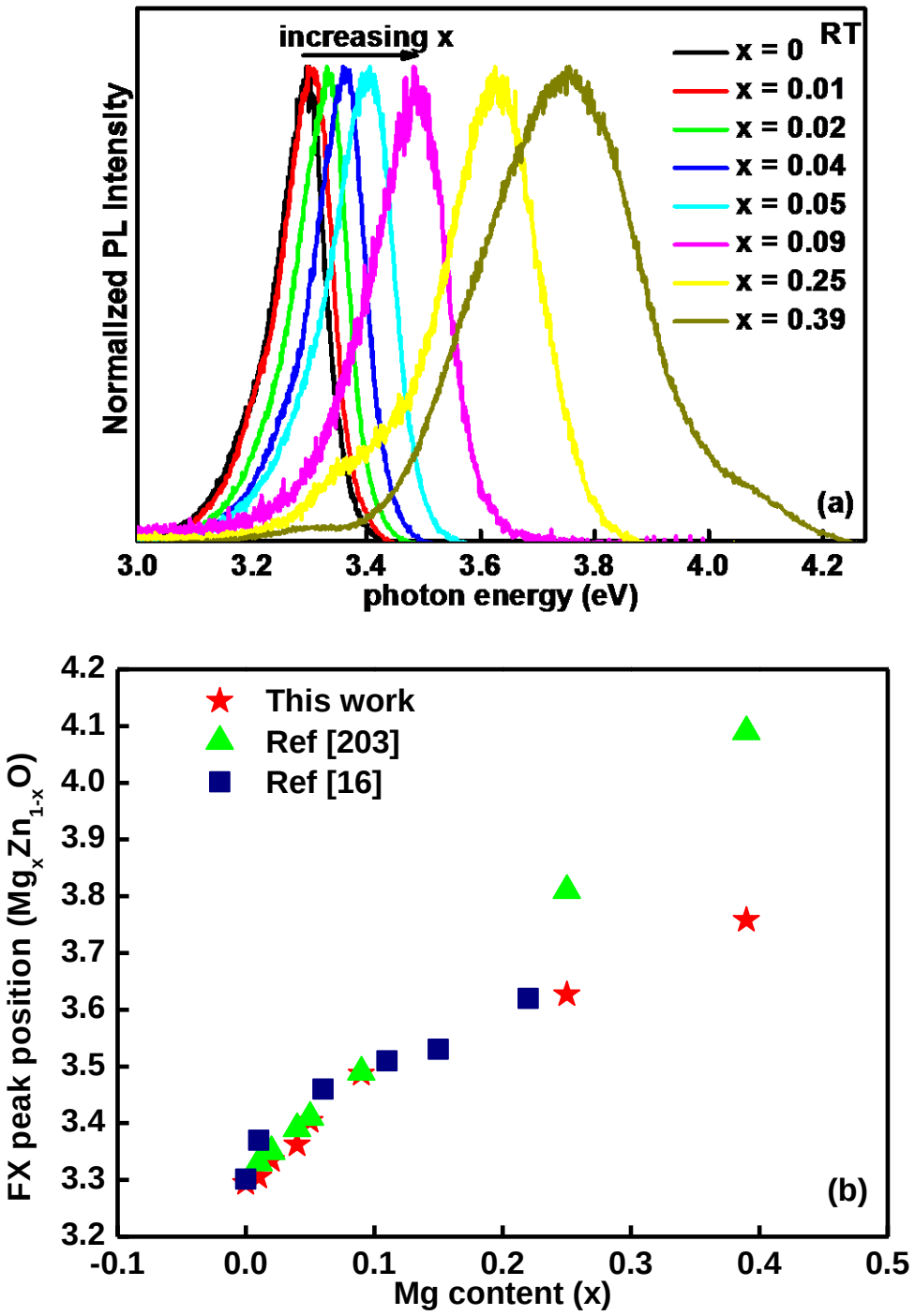

Figure 6-20 (a) RT PL spectra of $Mg_xZn_{1-x}O$ ($0 \leq x \leq 0.39$) films. (b) Dependence of the FX peak position of the films on Mg content

$In_xGa_{1-x}N$ system, where Shimizu *et al.* [215] observed double peaks in the near band edge emission from relaxed $In_{0.19}Ga_{0.81}N$. The peaks were assigned to GaN and InGaN. The FWHM of the main PL peak in figure 6-20(a) increases from 92 meV for x=0 to 285 meV for

x=0.39. It is important to also mention that the FWHM for x=0.39 is overestimated by the possible presence of the (e, A^0) transition. This increase in the FWHM is generally attributed to alloy broadening as also noticed for the growth of $Mg_xZn_{1-x}O$ using TBOH [14]. The cause of this broadening could be inhomogeneous strain, finite domain size effects, alloy clustering and the presence of dislocations and stacking faults [199, 205].

Figure 6-20(b) shows the RT PL peak position as function of the Mg solid content, along with other results published by Heitsch *et al.* [203] (PLD, a-Al_2O_3, 675 ˚C) and Ashrafi *et al.* [16] (MOCVD, 6H-SiC (0001) substrate, 400-600 ˚C). The PL peak positions coincide for all three sets of data ($x \leq 0.2$). Strong discrepancies arise for $x \geq 0.2$. The reported PL peak positions as function of the Mg content for $Mg_xZn_{1-x}O$ films and the majority of ternary alloys, in general, drastically differ due to the use of different substrates, deposition techniques and temperatures [216]. Thus, differences in sample quality, resulting from different experimental conditions, could explain the differences in the peak positions observed in Figure 6-20(b).

Stacking fault related PL

Figure 6-21 shows low temperature PL spectra (4.2 K) of the $Mg_xZn_{1-x}O$ samples with different Mg composition. The $Mg_xZn_{1-x}O$ PL spectra were shifted for x=0.01, 0.02 and 0.04 by 17 meV, 33.1 meV, and 62.1 meV, respectively, so that the D^oX position in each spectrum coincides. Observing the typical spectrum of ZnO, different transitions, which have been extensively studied in the past years, are noticed [162, 177]. The D^oX is present in all samples. The bands at 3.314 eV and 3.297 eV are ascribed to (e, A^0) and DAP recombination, respectively and their phonon replicas are also observed. The luminescence at ~3.314 eV is controversial in the literature and has often been assumed as evidence for *p*-type doping [217]. This energy is also very close to the energy of the free exciton phonon replica [175]. Schirra *et al.* [177] showed that the electronic nature of the 3.314 eV line is a (e, A^0) transition of electrons from the conduction band to holes localized at relatively shallow acceptor states at stacking faults. In their report, the cathodoluminescence (CL) was found to have the characteristics of a transition from the conduction band to acceptor-like states. It was suggested that electronic states due to dangling bonds are the most likely source of the acceptor-like states. It should be stressed that the presence of this band does not prove the presence of acceptor impurities, but rather point at crystalline defects in the samples

considered. This (e, A^0) transition involves a complex related to basal plane stacking faults [177].

Based on a hydrogen-atom-like model, the binding energy of an acceptor is estimated to be:

$$13.6\, m_h^*/m_0\varepsilon_0^2 = 105 \text{ meV} \quad (6.1)$$

using a hole effective mass of $0.59m_0$ [218] and a dielectric constant of 8.75 [218]. This compares well with the experimental value of E_A=124 meV [219] deduced from the PL peak position of the (e, A^0) transition, using the following formula:

$$E_{(e,\,A^0)}(T) = E_g(T) - E_A + k_B T/2 \quad (6.2)$$

Schirra *et al.* [177] reported a value of 130 meV, which is very close to the experimental value of 124 meV obtained from the spectrum for x=0 in figure 6-21 and confirms that the localized acceptor states causing the 3.314 eV luminescence in the present work are located in basal plane stacking faults.

When Mg is incorporated, the main D^oX found in ZnO, is seen to shift toward higher energies. All the other dominant lines seen for ZnO also appear in the spectra for the ternary films and shift by the same energy as the D^oX in each spectrum. It is clear, therefore, that the different luminescence transitions observed in the ZnO remain unchanged in nature when Mg in incorporated. Pronounced LO-phonon replicas are observed in the PL spectra of the ternary films due to the strong degree of ionicity (0.62 for the Zn-O bond; 0.84 for the Mg-O bond).

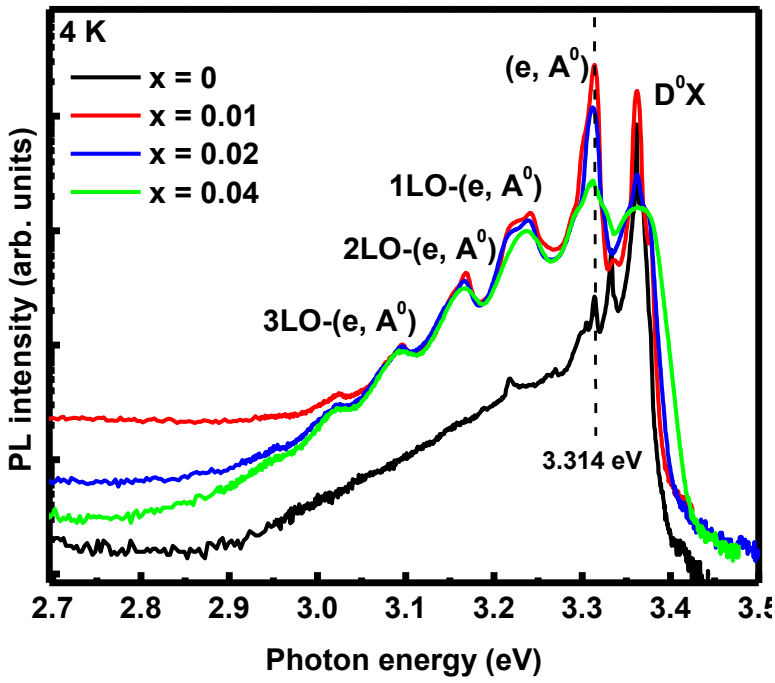

Figure 6-21 Low temperature PL spectra (4 K) of $Mg_xZn_{1-x}O$ films ($x \leq 0.04$). The spectra for the ternary films have been shifted so that the D^0X peak positions coincide with that of the D^0X position in the spectrum of the ZnO film

It is also seen that as the Mg content increases, the (e, A^0) transitions from stacking faults increase in relative intensity. This behaviour was also reported by Blaauw *et al.* [130], where for high Mg dopant concentration in InP stacking faults were observed with a density greater than 10^9 cm^{-2}. The incorporation of Mg atoms into ZnO tends to distort the hexagonal structure of the film, which could lead to dislocations and stacking faults since Mg^{2+} is smaller than Zn^{2+}. This fact is experimentally confirmed by Vashaei *et al.* [88], where they showed that the tendency of the stacking sequence to change from AaBbAaBb in the wurtzite structure to ABCABC in the cubic structure may cause partial dislocations and stacking faults.

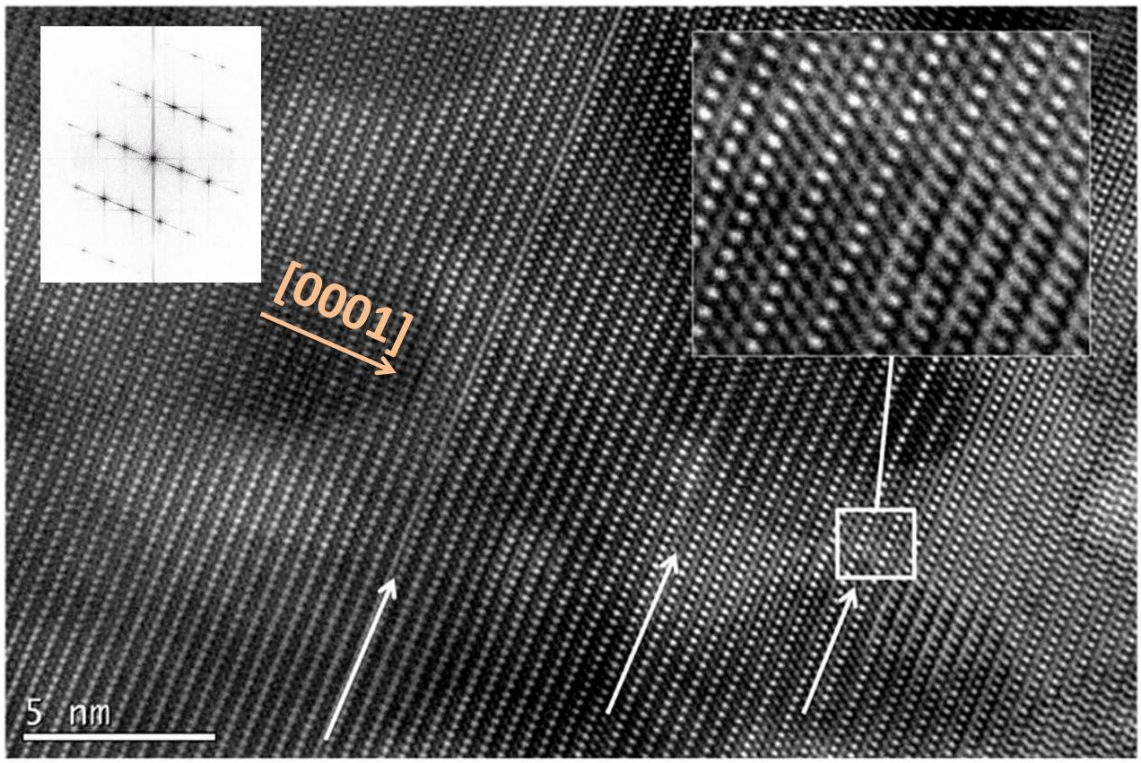

Figure 6-22 A HRTEM image of $Mg_{0.01}Zn_{0.90}O$ showing stacking faults when viewed along the [11-20] axis. The insert shows a sequence of stacking faults

In order to investigate the microstructure of the $Mg_xZn_{1-x}O$ films, cross sectional high resolution TEM (HRTEM) images were obtained from a sample with x=0.01. Figure 6-22 shows a HRTEM image of the film. The base planes are clearly resolved in this image. Stacking faults on the base plane are indicated by white arrows. The density of stacking faults is fairly high in this low Mg content film. Such stacking faults may also originate from incoherent boundaries between adjacent columnar grains during growth. The inset on the left side is a fast Fourier transform (FFT) from the HRTEM image. The incident electron beam is parallel to the [11-20] direction. The magnified insert on the right side shows a faulted section of the material, from which the stacking sequence is identified as...ABABABCBC..., which means the stacking fault is of type I [88]. The most plausible model for the generation of such a stacking fault is the condensation of vacancies or interstitials, which leads to a missing or additional (0001) plane.

6.5 Magnesium incorporation efficiency

The incorporation efficiency η of Mg into ZnO can be obtained from [220]:

$$\left(\frac{M_{Mg}}{M_{Zn}}\right)_{\text{Alloy}} = \eta \left(\frac{M_{Mg}}{M_{Zn}}\right)_{\text{Gas phase}} \quad (6.3)$$

where M_{Mg} and M_{Zn} are the mole fractions of the magnesium and zinc in the gas or solid phase. From EDX measurements, the elemental content of Mg and Zn was evaluated by probing various spots on the samples. Figure 6-23 shows the solid (x) vs vapour (x_v) composition relationship for growth using TBOH and O_2. The straight line indicates the solid composition expected for an incorporation efficiency of one. The solid composition x increases with increasing x_v while the Mg incorporation efficiency seems to increase. For x_v=0.15, 0.3 and 0.45, the calculated values for η are 0.32, 0.37, and 0.49, respectively. As these results show, an increase in $(MeCp)_2Mg$ flow relative to DEZn seems to increase the incorporation efficiency of Mg. The probable explanation is that the DEZn reacts more efficiently with the oxidizing source than the $(MeCp)_2Mg$ in the gas phase. Thus, the decrease in DEZn flow which is accompanied by an increase in $(MeCp)_2Mg$ to keep the VI/II ratio constant, allows Mg to substitute more readily on the Zn lattice sites.

Furthermore, it is worthwhile to add that the Mg incorporation depends strongly on the reactor pressure. For example, at a system pressure of 250 Torr, no traces of Mg incorporation was detected in the sample, while at 20 Torr, for the same growth conditions, the Mg incorporated efficiently into the ZnO thin films. The low incorporation efficiency of Mg into ZnO could also be explained by a lower adsorption rate of Mg (compared to Zn) and a lower decomposition rate of $(MeCp)_2Mg$ compared to DEZn, or by pre-reactions between the Mg precursor and TBOH/O_2.

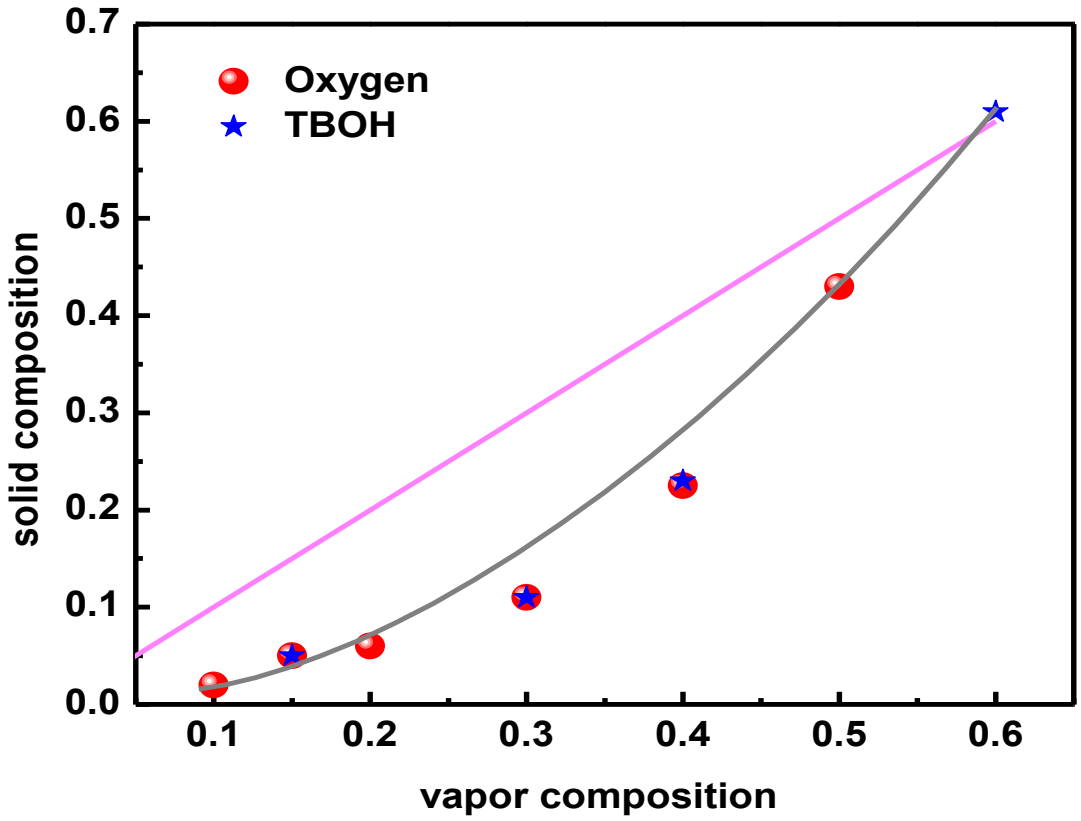

Figure 6-23 Solid composition versus vapour composition. The straight line indicates the solid composition expected for an incorporation efficiency of one

6.6 Detailed photoluminescence study of $Mg_xZn_{1-x}O$ thin films

In this section, the PL of $Mg_xZn_{1-x}O$ thin films is investigated in more detail. Temperature dependent PL measurements on layers with low Mg concentration (x=0, 0.05 and 0.1) are studied and it is shown that the main bound exciton peak position exhibits an "s-shape", characteristic of localization in a disordered alloy. The origin of the PL line broadening of $Mg_xZn_{1-x}O$ is also analysed with respect to alloy broadening, taking into account a random cation distribution and alloy clustering. An analysis of the deep level emission is given.

6.6.1 Temperature dependent PL

In order to investigate the behaviour of the different optical transitions assigned to various defects in previous sections, the temperature dependent PL was performed for selected temperatures between 4 K and 160 K for $Mg_{0.05}Zn_{0.95}O$ (Figure 6-24 bottom) and between 4 K and 70 K for ZnO (Figure 6-24 top). These layers were grown at 420 ˚C using a VI/II ratio of 60 and TBOH as oxidant. It can be seen that the PL spectra of the ZnO film comprise

various emission features, which change in relative intensities and exhibit different peak shifts with temperature. Upon an increase in temperature, the dominant D^oX emission red-shifts and decreases rapidly in intensity. The quenching of this emission with temperature is accompanied by the increased prominence of two transitions on its higher energy side. This could be explained as follows: as the temperature rises, the shallow D^oX thermally dissociates into free excitons, and therefore the FX emission becomes more prominent. As the temperature increases further, the D^oX line disappears and the FX transition becomes dominant. The Y-line at 3.33 eV is known to rapidly vanish with increasing temperature and disappears above 30 K. Furthermore, as the temperature increases, the DAP transition (appearing at 3.298 eV at 4 K) and its LO-phonon replica quench with increasing temperature and above 50 K the associated (e, A^0) transition on its high energy side becomes more pronounced. This is due to the ionisation of the shallow donor taking part in the pair emission. The behaviour of the (e, A^0) is in conformity with the observations by Thonke *et al*. [221] and Schirra *et al*. [177]. They reported that this transition develops a pronounced high energy Boltzmann tail with increasing temperature, typical for a free-to-bound transition.

The dominant donor for ZnO as well as for $Mg_xZn_{1-x}O$ (low Mg incorporation) is Al/Ga, mostly incorporated from the organometallic sources used and possibly sapphire substrate, if used. However, due to the broadness of the spectrum it is possible that the nature of the impurity responsible for the bound excitonic transition changes. For example, Grundmann *et al*. [205] showed that the D^oX changes from I_6 (Al-related) to I_4 (H-related) for x=0.045.

In high quality ZnO, the neutral shallow donor bound exciton often dominates because of the presence of donors caused by unintentional impurities and/or shallow donor-like defects. This is clearly also the case for $Mg_xZn_{1-x}O$ films with a low Mg content. The behaviour (thermal quenching) of this line observed for both ZnO and for $Mg_{0.05}Zn_{0.95}O$, conforms with other published results [223, 224]. Some reports on $Mg_xZn_{1-x}O$ (x=0.1) have shown the persistence of the D^oX transition up to RT [223], which indicates a localization energy (E_{loc}) comparable to the thermal energy k_BT at RT. Using the relation for the D^oX energy [223]

$$E_{D^oX}(T) = E_{FX}(T) - E_{loc}, \tag{6.4}$$

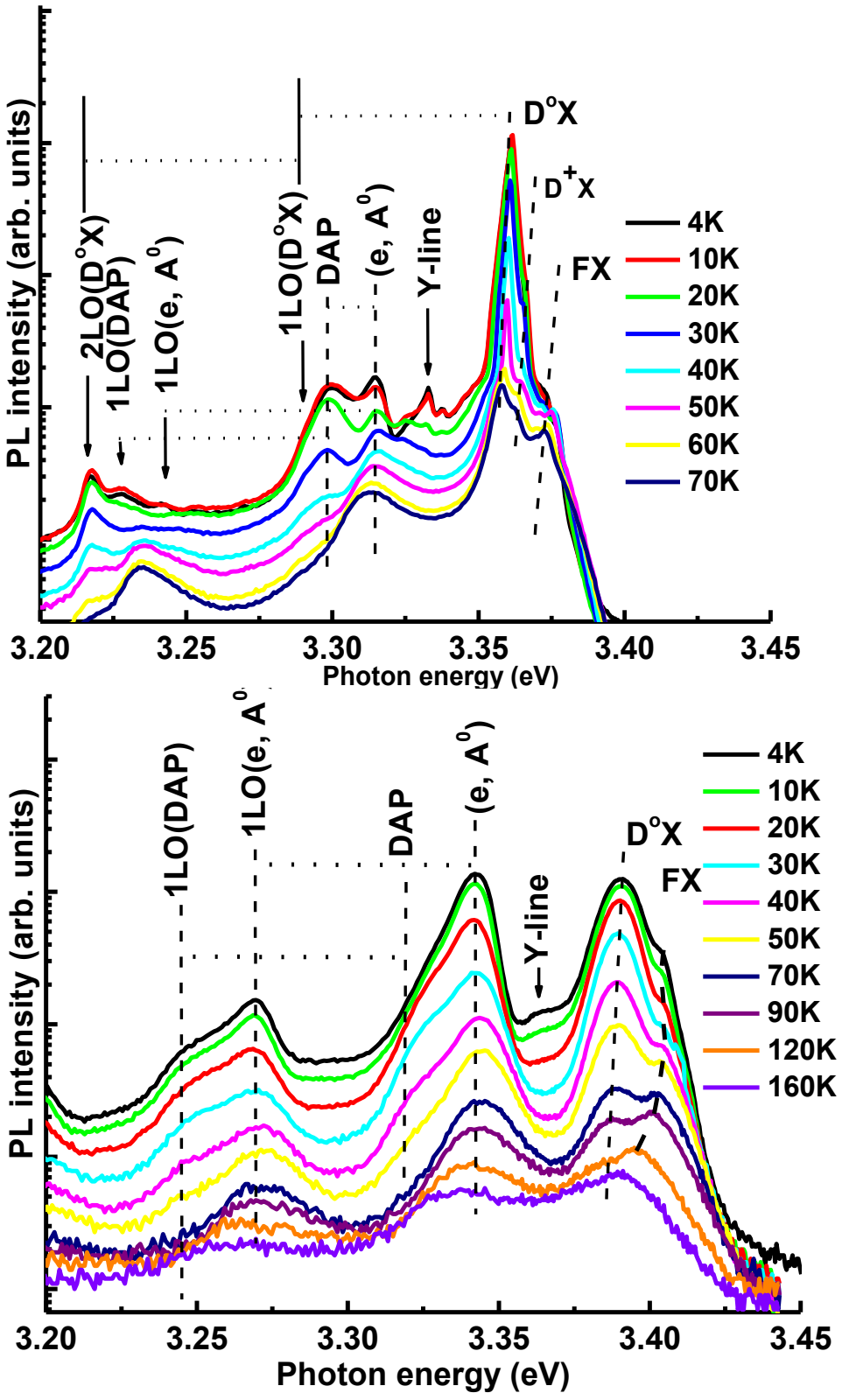

Figure 6-24 Temperature dependent PL spectra of ZnO on Al_2O_3 (0001) (top) and $Mg_{0.05}Zn_{0.95}O$ on Al_2O_3 (0001) (bottom)

where E_{loc} is the bound exciton localization energy, this group reported a value of ~16.5 meV for x=0 and 35 meV for x=0.1. The E_{loc} of ZnO is much smaller than 35 meV. Using Hanes Rules, Pan *et al.* [197] derived the two values of the donor binding energy of ZnO and $Mg_{0.1}Zn_{0.9}O$, and concluded the donor level to be deeper than that of ZnO since $E_D(Mg_{0.1}Zn_{0.9}O)>E_D(ZnO)$.

For $Mg_xZn_{1-x}O$, the increase of the (e, A^0) signal strength could be due to an increased concentration of Zn vacancies, which could lead to the formation of base plane stacking faults and hence enhance the DAP and (e, A^0) emission. It is valuable to note that the energy separation of the longitudinal phonon replicas of the $Mg_xZn_{1-x}O$ is almost the same as the LO phonon energy of ZnO (~72 meV).

Figure 6-25 shows the temperature dependent PL spectra of the $Mg_{0.05}Zn_{0.95}O$ film, excited with a NeCu laser line, between 84 K and RT. Note that due to the poorer resolution of the mini PL system, the FX and D^oX lines cannot be resolved at 84 K and 90 K (compare to figure 6-24 (bottom)). It can be seen that the PL spectra consist of different emission features, which change in relative intensities and display different peak shifts with temperature. From 84 K to 140 K the NBE emission is dominated by the FX+D^oX lines, which red-shifts with increasing temperature. Above this temperature the FX dominates. The peak on the lower energy side of the D^oX line is the (e, A^0) transition. The (e, A^0) transition can still be seen at RT. It seems plausible to assume that for films with higher Mg content, this transition dominates the spectra at RT.

Since free and bound exciton peak energies differ from the band gap by values that are independent of the temperature, they follow the band gap change with increasing temperature. Furthermore, the intensity of the bound exciton peak may be fitted with the following equation [158]:

$$I_{BX} = \frac{I_0}{1+C\exp\left(-\frac{E}{kT}\right)} \qquad (6.5)$$

where C, E, and I_0 are fitting parameters. E is known as the quenching activation energy and is often a good approximation for E_{loc}. I_0 is the intensity of the D^oX at T=0 K and k is the Boltzmann constant.

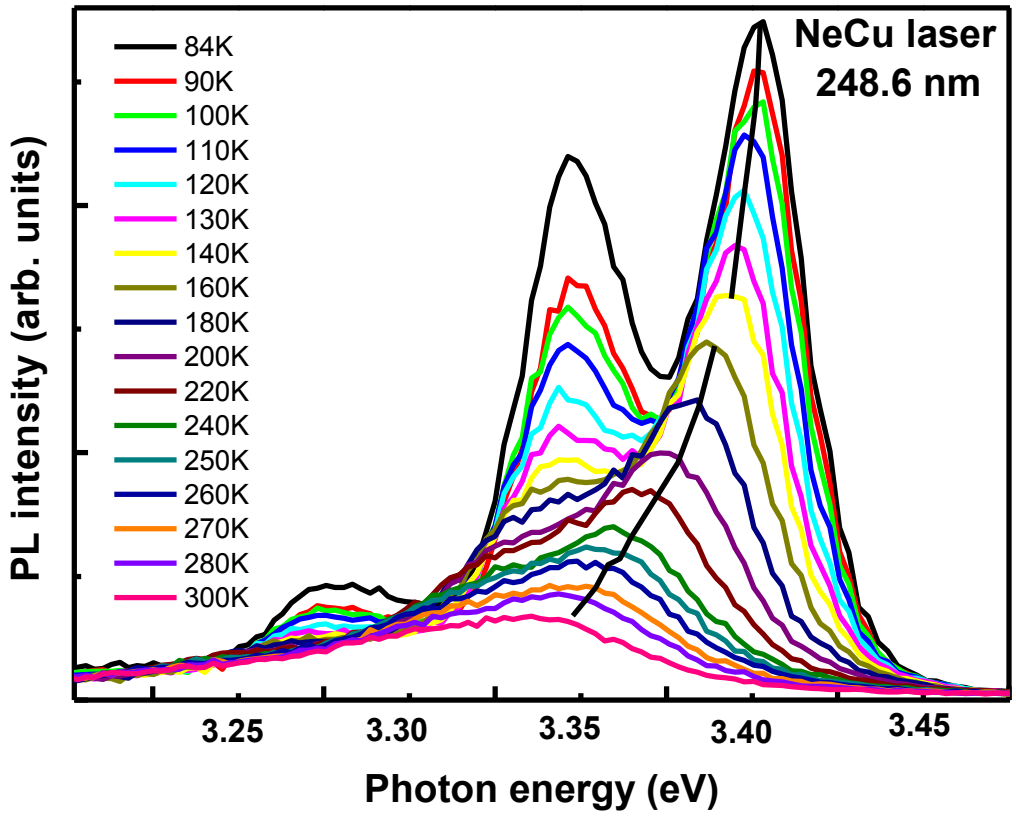

Figure 6-25 Temperature dependent PL spectra of $Mg_{0.05}Zn_{0.95}O$ film between 84 K and RT

Figure 6-26 shows the integrated PL intensity of the D^oX line measured for both samples as a function of the inverse of temperature. The fitted activation energies E for ZnO and $Mg_{0.05}Zn_{0.95}O$ are 13.7 meV and 19.2 meV, respectively. The activation energy increases with increasing Mg content, confirming the increase in the localisation energy and therefore possibly in the binding energy of the donor involved in this transition [225]. These values compare favourably with the values measured from the PL spectra in figure 6-24 (12.5 meV for ZnO and 15.2 meV for $Mg_{0.05}Zn_{0.95}O$) and with the value of 16.5 meV reported by Pan *et al.* [197] for x=0.1.

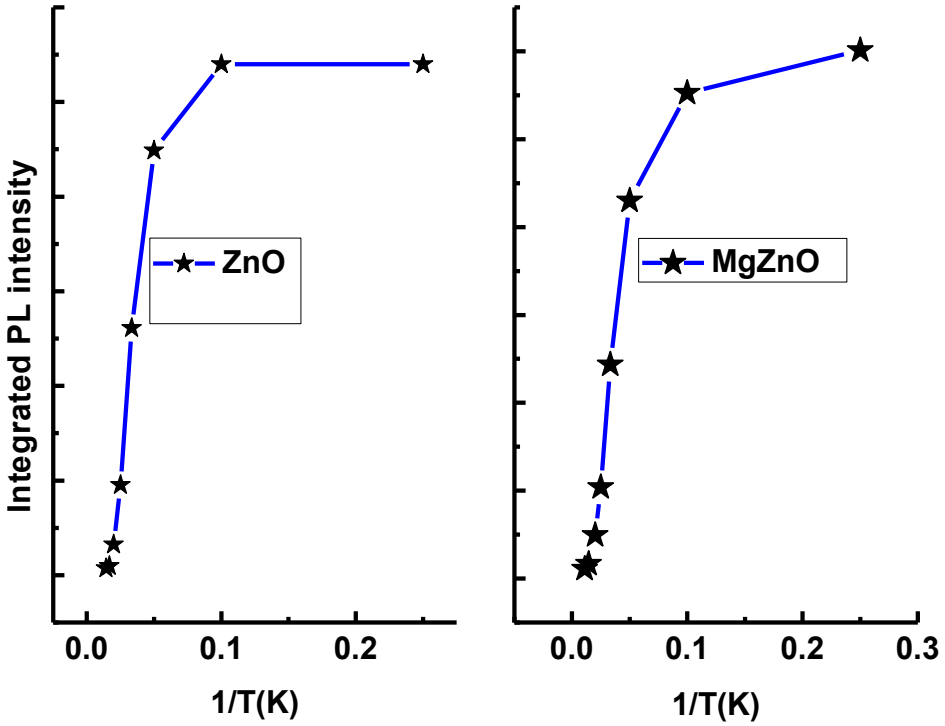

Figure 6-26 Intensity decay with increasing temperature of the D^oX line for ZnO and $Mg_{0.05}Zn_{0.95}O$ fitted with equation (6.5)

6.6.2 Exciton localization effects due to disorder

Exciton localization in semiconductor alloys has been the subject of continuous interest. Localized excitons, referring to excitons that are spatially localized due to composition, charge or strain fluctuations in crystals or films, have stimulated intensive research in the past decades because they have been found to be responsible for the high emission efficiency of a variety of semiconductor alloys [226]. The random placing of metal atoms on the cation sub-lattice leads to potential fluctuations and subsequently, to disorder-induced broadening of spectral lines (alloy broadening) [225]. It is experimentally proven for $Al_xGa_{1-x}As$ that exciton localization reduces the contribution to the broadening due to impurities, statistical disorder, defects, and thermal energy [161]. Generally, exciton localization is only predominant at temperatures at which excitons are stable. The excitons in oxide semiconductors seem to be easily localized by alloy fluctuations, due to the strong electronegativity and small Bohr radius of the exciton. This implies that excitons are more sensitive to local inhomogeneities [227].

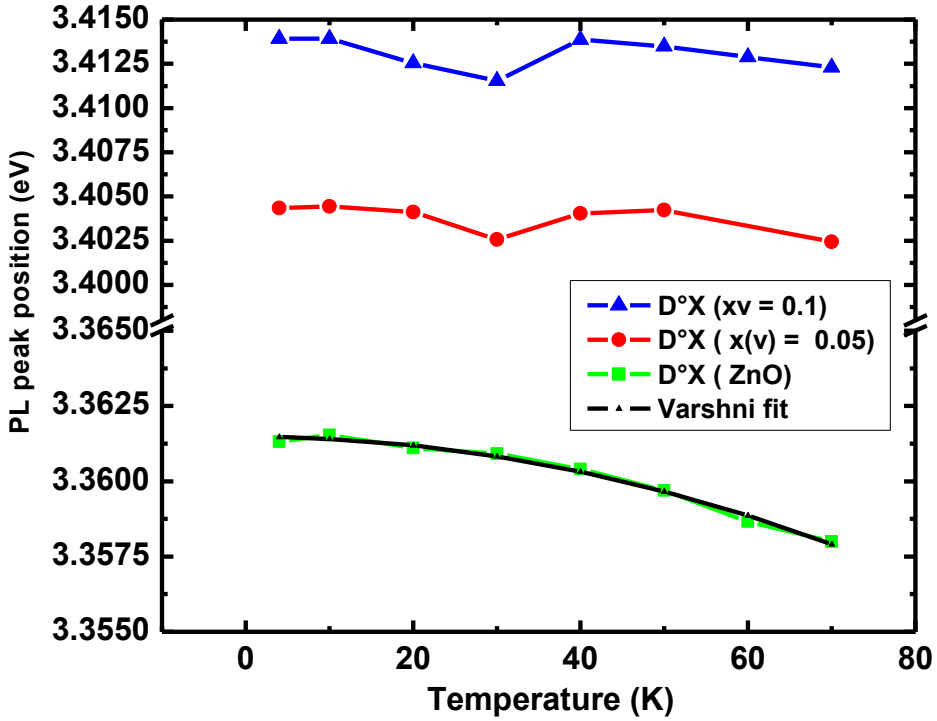

Figure 6-27 D^oX peak energy vs temperature for ZnO and $Mg_xZn_{1-x}O$ thin films with x_v=0.05 and 0.1 (The D^oX of ZnO is fitted to the Varshni relation)

Figure 6-27 shows the D°X energy (extracted from a Gaussian de-convolution of the temperature dependent PL spectra of $Mg_xZn_{1-x}O$ films grown with x_v=0, 0.05, 0.1) plotted versus temperature. A monotonic decrease of the D^oX energy caused by the band gap shrinkage with increasing temperature is observed for ZnO. For the ternary films, the emission line first red-shifts with respect to the Varshni formula. Upon a further increase in temperature (30–40 K), a slight blue-shift is observed, followed at higher temperatures by a systematic red-shift. This behaviour has been observed in $Mg_xZn_{1-x}O$ and other semiconductor alloys [93, 177, 205]. Bell *et al*. [228] showed that at the lowest temperatures, excitons will become trapped in local potential minima. This phenomenon is called "*exciton freeze out*". As the excitons gain kinetic energy (i.e. their transport is thermally enhanced), they are able to thermalise into the lowest potential minima, causing a red-shift. The red-shift is of the order of σ^2/k_BT, where σ is the standard deviation of the excitonic emission in the alloy due to alloy broadening. As expected, the red-shift increases with increasing x_v (from 1.5 meV to 2.5 meV), due to the fact that alloy broadening increases with Mg content. This is confirmed by Ye *et al.* [229] who used Raman and PL spectroscopy of $Mg_xZn_{1-x}O$ to show that the disorder associated with the incorporation of Mg enhances exciton localization and asymmetrically broadened the phonon lines. The blue-shift observed above 40 K arises from

a delocalization of excitons and the final red-shift in the high temperature range is dominated by the thermally induced band gap shrinkage. This is typical for most semiconductor alloys [226, 205].

6.6.3 PL line broadening

As mentioned above, line broadening is caused by different mechanisms. The broadening of the exciton linewidth in substitutional alloys is primarily due to alloy fluctuations within the exciton volume. In an ideal alloy semiconductor $A_xB_{1-x}C$, the excitonic line width is given by [231]

$$\Delta E_{exc} = 2.36\sigma^E = 2.36\frac{dE_g}{dx}\left[\frac{x(1-x)}{KV_{exc}}\right]^{1/2} \quad (6.6)$$

where dE_g/dx is the change in the energy gap with the alloy composition x, K is the cation density in the wurtzite structure and V_{exc} is the excitonic volume ($V_{exc} = 10\pi a_B$) [231]. Grundmann *et al.* [205] proposed that in $Mg_xZn_{1-x}O$, alloy clustering effects (i.e. a non-random distribution of Mg on the cation sites) plays a significant role in the linewidth broadening and can be estimated by

$$\Delta E_{exc} = 2.36\sigma^C = 2.36\frac{dE}{dx}\left[\frac{x(n-x)}{KV_{exc}}\right]^{1/2} \quad (6.7)$$

where n is a integer between 1 and 4 (the maximum number of Mg atoms that could surround a given oxygen atom).

Figure 6-28 compares the FWHM of the D^0X lines with the theoretical results based on Eq. (6.6) and Eq. (6.7). Eq. (6.6) considers alloy disorder and does not take into account broadening due to degradation of the crystal quality, alloy clustering and defects, whereas Eq. (6.7), takes into account the presence of Mg_nO clusters in the films. It is evident that the experimental PL linewidths are larger than those calculated assuming a statistically random distribution of Mg. In most other works [205], the experimental values are greater than those deduced from theory due to additional causes. It is also clear that clustering yields linewidth values that are much higher than those found experimentally here. This is unlike Grundmann's work [205], where the PL spectra showed no evidence of extended defects (stacking faults, dislocations) like in the samples studied here. The present results cannot be only interpreted in terms of a purely random alloy. Thus, to explain the increase of the FWHM, one can take into account the strong immiscibility of MgO in ZnO even for low

compositions, as suggested for InN based ternary alloys in Ref. [232]. This could lead to phase segregation resulting in compositional inhomogeneities larger than what is expected from statistical randomness [88]. Futhermore, it is suggested that the presence of stacking faults in all the samples could contribute to line broadening. The effects of defects such as stacking faults and dislocations on the theoretical linewidth should thus also be considered.

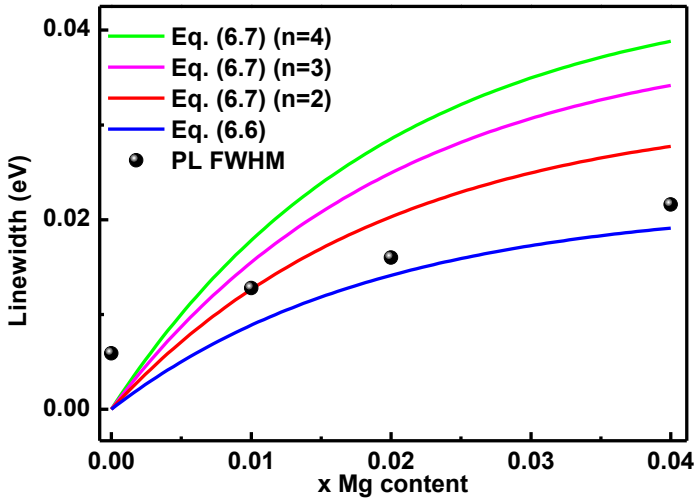

Figure 6-28 Linewidth of the D°X emission versus Mg content

6.6.4 Laser power dependence

The nature of the different PL transitions, especially the (e, A^0) transition can also be deduced from the excitation intensity dependence. The excitation power dependence of the PL lines of $Mg_xZn_{1-x}O$ was investigated in order to provide further insight into the mechanisms responsible. To confirm the nature of the D^oX transition, the evolution of its intensity as function of the excitation intensity was studied.

Figure 6-29 shows low temperature (4.2 K) PL spectra of $Mg_xZn_{1-x}O$ (x_v=0.1) grown on c-Al_2O_3 obtained at different excitation powers. Two main transitions, labelled D^oX and (e, A^0), can be seen. The peaks at lower energies are LO-phonon replicas of the (e, A^0) transition. No peak shift is observed. The D^oX and (e, A^0) lines have slightly different dependencies on excitation power, with the former line increasing slightly faster than the latter. As the excitation power increases, some broadening is observed on the higher energy side of the D^oX line, suggesting the emergence of FX emission. Neither the D^oX nor the (e, A^0) line shifts with laser power. From these measurements, it is difficult to conclude a difference in the nature of the two emission lines.

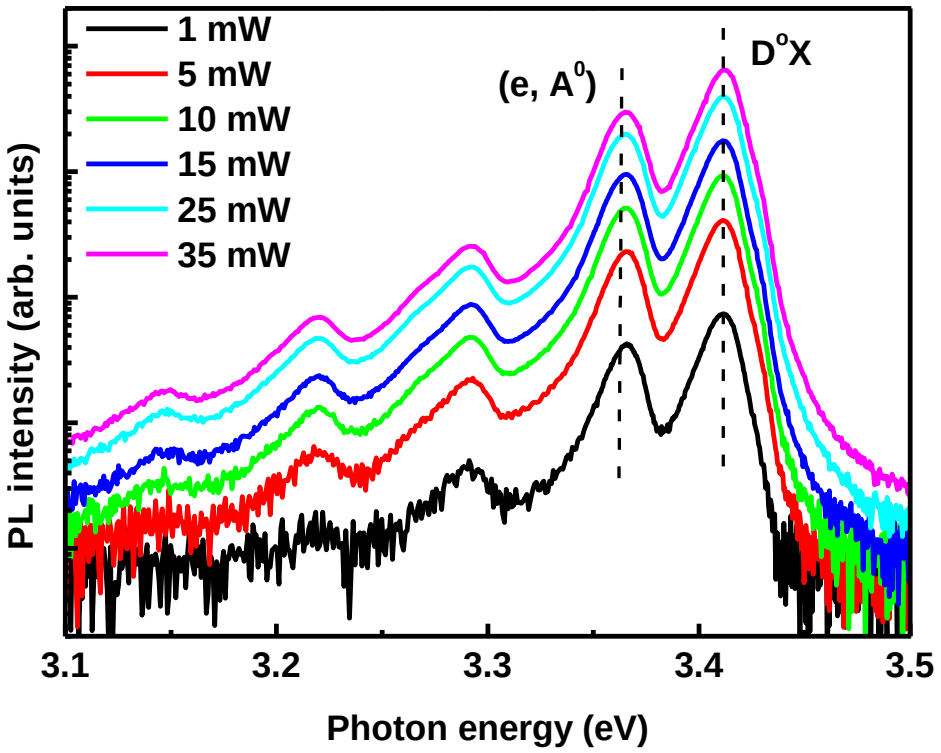

Figure 6-29 Low temperature (4.2 K) PL spectra at different excitation power of $Mg_xZn_{1-x}O$ (x_v=0.1) grown on c-Al_2O_3

6.6.5 Deep level emission in $Mg_xZn_{1-x}O$

Figure 6-30 shows the normalized PL spectra (85 K) for films grown on c-Al_2O_3 with various x_v. Two prominent bands can be seen; NBE emission and a broad DLE band. Both bands shift toward higher energies with Mg content. As expected, the NBE emission broadens due to an increase in Mg content. The DLE band shifts by the same amount as the NBE emission. This was also found by Trunk *et al.* [233]. The broad DLE band measured for ZnO was deconvoluted into two Gaussian components, one at 2.35 eV and another one 2.53 eV, in order to resolve individual constituents of the DLE. The former band is believed to be related to zinc vacancies V_{Zn}, while the latter has been ascribed to oxygen vacancies V_O [234]. When Mg atoms substitute Zn atoms, the Mg 3*s*-like states raises the CBM, leaving in the first approximation the VMB unchanged. Since the DLE tracks the NBE emission, it seems reasonable to conclude that the deep acceptor (i.e. V_{II}) tracks the CBM, while the energy level of the deep donor (i.e. V_O) remains approximately constant relative to the VBM. This could also explain the observed blue-shift of the DLE bands with increasing Mg content in Ref. [234].

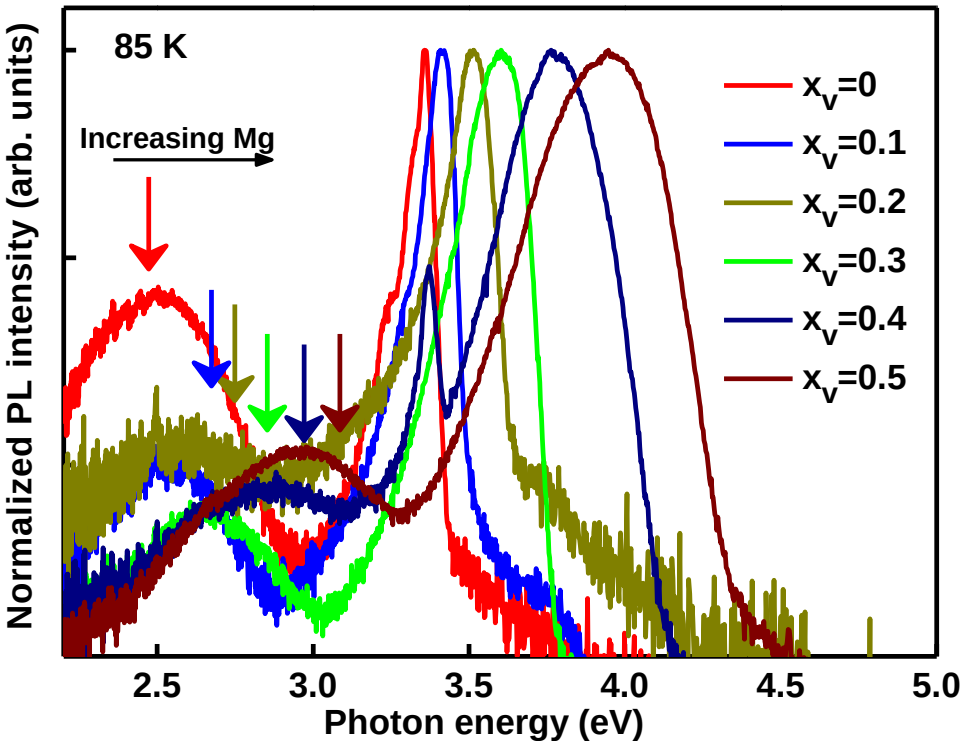

Figure 6-30 Normalised PL spectra (85 K) of $Mg_xZn_{1-x}O$ grown on c-Al_2O_3

6.7 Conclusions

The growth of $Mg_xZn_{1-x}O$ thin films on c-Al_2O_3 substrate by MOCVD has been illustrated. $Mg_xZn_{1-x}O$ films were grown at 420 ˚C using two different oxygen precursors (TBOH and oxygen gas). DEZn and $(MeCp)_2Mg$ were used as Zn and Mg sources, respectively, while the VI/II ratio was fixed at 60 and the reactor pressure at ~20 Torr. The effect of Mg incorporation on the structural and optical properties was analysed. EDX measurements confirmed the incorporation of Mg into ZnO, but showed that Mg is distributed non-uniformly for $x \geq 0.1$ (laterally and with depth). RT near band edge PL and absorption spectra confirmed the increase in the band gap towards the deeper UV. The FWHM of the XRD spectra as well as the FWHM of the PL lines were seen to increase with Mg content, which has been assigned to the presence of stacking faults and inhomogeneous strain. The surface morphology was found to vary from hexagonal crystallites to cubic crystallites upon increasing the Mg content. Evidence for phase separation was deduced for higher Mg concentrations ($x \geq 0.23$) from XRD measurements, where the presence of both the (111) MgO peak and (0002) $Mg_xZn_{1-x}O$ peak was detected. TEM showed the presence of an interfacial layer between $Mg_xZn_{1-x}O$ and the Al_2O_3 substrate for higher Mg incorporation. This interface is suspected to be cubic $MgAl_2O_4$. The c-axis length of the film was shown to decrease with

increasing Mg content, as a result of the smaller ionic radius of Mg^{2+} compare to Zn^{2+}. Low temperature PL (4.2K) showed the D^oX, (e, A^0) and the LO phonon-replicas of the (e, A^0) transition to be the main transitions in the spectra. The 3.314 eV line in the low temperature PL spectra of ZnO was seen to shift toward higher energy and also to increase in relative intensity as the Mg content increased. This line has been related to basal plane stacking faults. HRTEM confirmed the presence of stacking faults in the films.

The temperature dependent PL of ZnO and $Mg_{0.05}Zn_{0.95}O$ has been investigated. The behaviour of the different emission lines confirmed the mechanisms assigned. The temperature dependence of the D^oX line was described within the context of localization in a disordered alloy potential. PL line broadening exceeded that expected for a random distribution of atoms on the cation site, but was less than what is expected for clustering. It has been suggested that the presence of stacking faults could be one of the causes of the line broadening in the PL spectra.

Chapter 7 Optimisation of growth parameters for $Mg_xZn_{1-x}O$

As part of optimizing the growth of $Mg_xZn_{1-x}O$ thin films, the various growth parameters were systematically varied. Such an optimization process is also essential to improve the quality of the thin films. In this study, the effect of growth temperature, VI/II ratio, growth rate, post growth annealing and buffer layer on the properties of the films as well as on the Mg incorporation was investigated. In this chapter, the effect of the growth parameters on the incorporation of Mg and on the microstructure, morphology and optical properties of the films will be reported.

7.1 Mg incorporation in films grown with TBOH

7.1.1 Growth Temperature

Photoluminescence

Figure 7-1 shows the normalized 85 K PL spectra of $Mg_xZn_{1-x}O$ films (x_v=0.2, VI/II ratio=60) grown at different temperatures on c-plane Al_2O_3. The spectra of the films grown at 380 ˚C and 480 ˚C are dominated by D°X recombination (indicated by arrows), with the (e, A^0) emission appearing as either a shoulder or a distinct peak on the lower energy side. The PL of the film grown at the lowest temperature is of poor quality (i.e. the lines are broad). Low growth temperatures will result in a low decomposition rate/efficiency of the metalorganic precursors and a low surface mobility of the reactants, leading to poor quality films. Also, the Mg incorporation in this film is slightly reduced, possibly due to incomplete decomposition of $(MeCp)_2Mg$. This sample shows a strong peak centred at 3.32 eV, which is believed to be a (e, A^0) transition related to stacking faults in the films. The sample grown at 580 ˚C has very weak luminescence as well as a poor surface morphology and inferior structural properties (see next section). This is ascribed to the re-evaporation of reactants from the growth front, which leads to a lower growth rate and weaker PL. It is worth noting that Muthukumar *et al.* [28] found an optimum temperature of ~400 ˚C for the growth of $Mg_xZn_{1-x}O$ by MOCVD and using the same sources as in this study. This is in good agreement with the temperature range of 380 ˚C to 450 ˚C yielding higher quality films in our reactor.

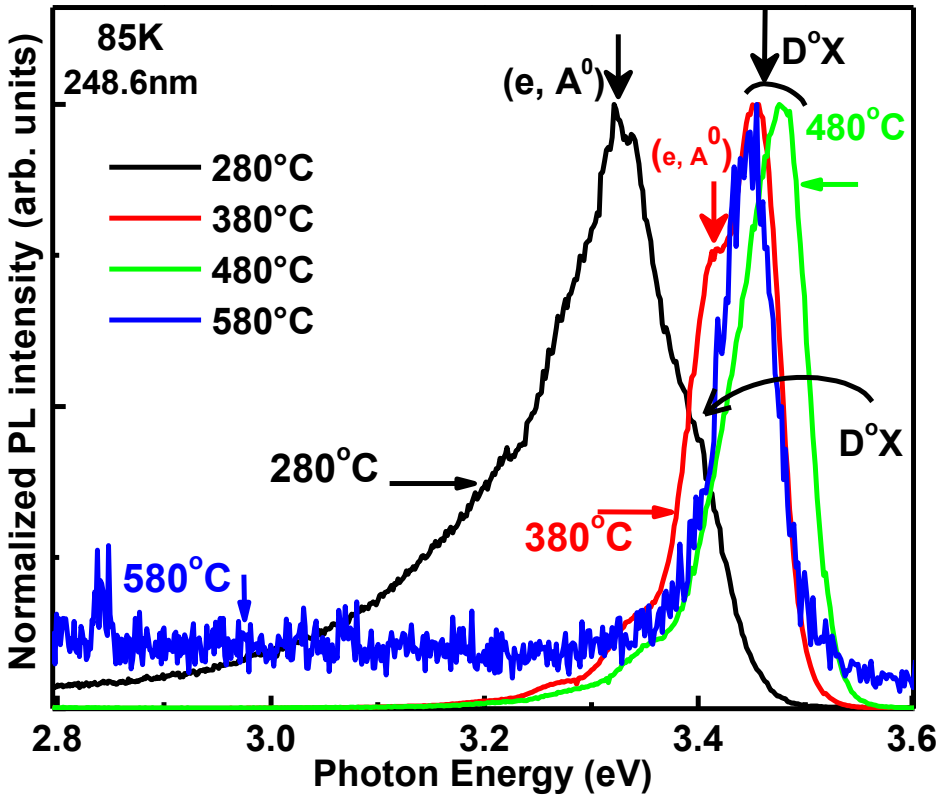

Figure 7-1 Normalized PL spectra taken at 85 K for $Mg_xZn_{1-x}O$ films (x_v=0.2) grown on Al_2O_3 (0001) at different temperatures (280 ˚C to 580 ˚C) using TBOH as oxygen source

Surface morphology

Figure 7-2 shows the surface morphology of the same films grown at different temperatures on c-Al_2O_3. The surface morphology clearly varies with changing growth temperature. At the lowest growth temperature (T_g=280 ˚C), the surface is almost featureless with small crystallites distinguishable. As in the case of growth of ZnO using TBOH, low temperature growth leads to a low decomposition rate of the alkylzincalkoxide and low surface mobility of reactant species, which results in partially amorphous material [123]. This is supported by the very weak XRD signals observed for this sample. Upon increasing the temperature to 480 ˚C, the surface morphology improves in the sense that the columns are clearly faceted with no evidence for the decoration of these crystals by smaller crystallites (as observed at 280 ˚C). The columnar crystals also increase in diameter. The SEM image of the sample grown at 380 ˚C (not shown) is the same as the one grown at 480 ˚C. A further increase in temperature to 580 ˚C results in a change in the shape of the crystallites to plate-like, with no clearly preferred orientation.

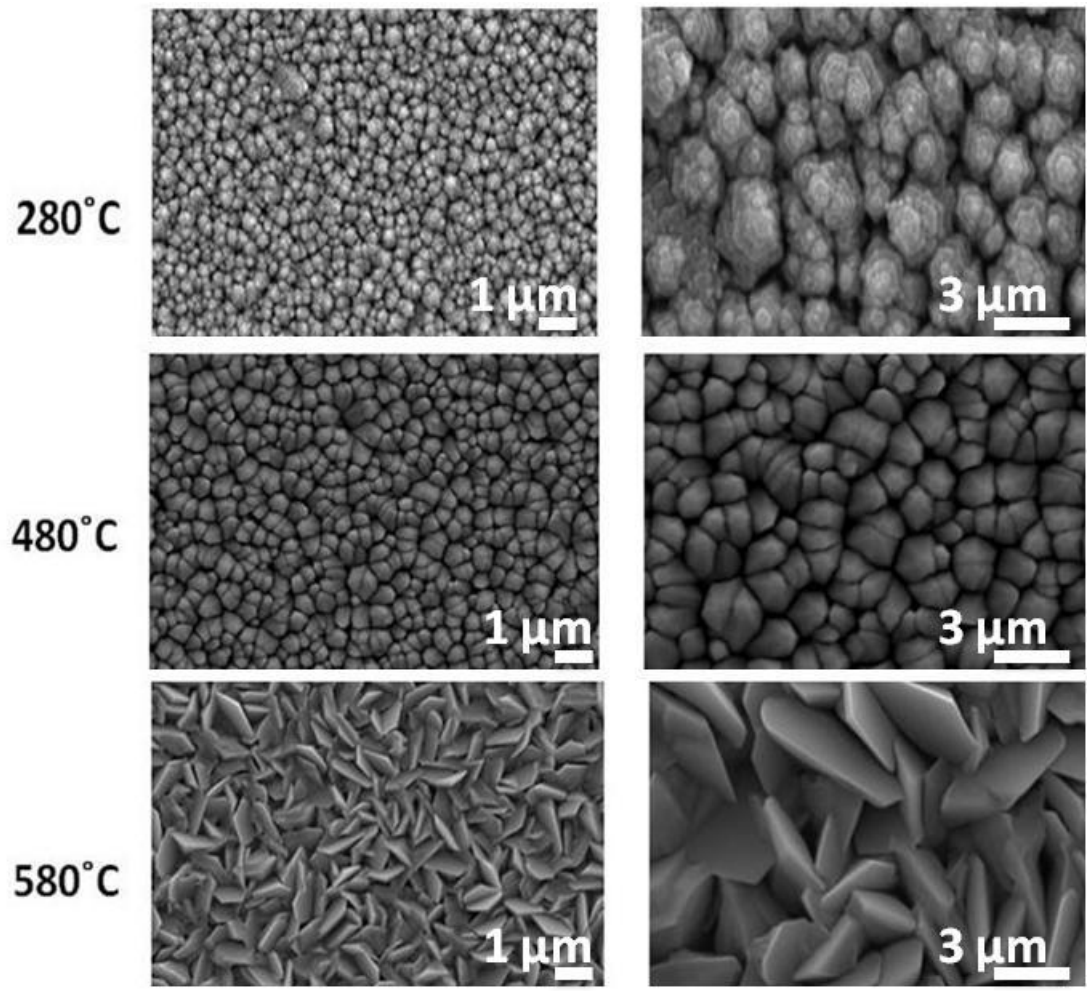

Figure 7-2 SEM images of the surfaces of $Mg_xZn_{1-x}O$ films grown on Al_2O_3 (0001) using TBOH at 280 ˚C, 480 ˚C and 580 ˚C at two different magnifications

For ZnO grown using DEZn and TBOH in our reactor, the optimum growth temperature is around 380 ˚C [123]. From the present results, it can be concluded that the Mg incorporation does not vary greatly around the optimum temperature (for ZnO) but that the morphology is strongly affected. The incorporation efficiency of Mg atoms depends strongly on the decomposition of DEZn, which serves as catalyst for $(MeCp)_2Mg$ pyrolysis [139]. From the above results a growth temperature for $Mg_xZn_{1-x}O$ films between 380 ˚C and 480 ˚C was chosen. Thus, the growth temperature of all the samples discussed here after was 420 ˚C. An important observation is that for temperatures over 600 ˚C, the $Mg_xZn_{1-x}O$ layers become optically dead (i.e. no PL could be detected).

7.1.2 VI/II ratio

Photoluminescence

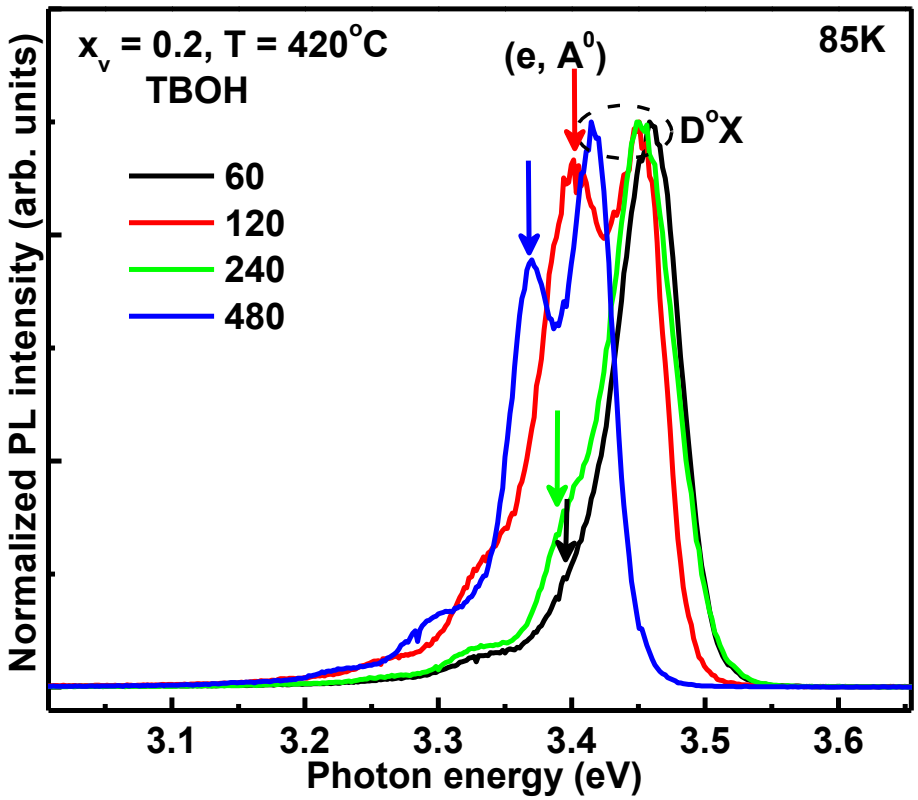

Figure 7-3 Normalized PL spectra (85 K) for $Mg_xZn_{1-x}O$ films (x_v=0.2) grown with different VI/II ratios (60, 120, 240, 480) using TBOH as oxygen source

Figure 7-3 shows the normalised PL spectra measured at 85 K of $Mg_xZn_{1-x}O$ films (x_v=0.2) grown at 420 °C with different VI/II ratios. The D°X line dominates each spectrum, with the (e, A^0) line and its phonon replicas also present. It is noticed that for the highest VI/II ratio, the Mg incorporation decreases somewhat, as evidenced by the red-shift of the D°X line. This could indicate a stronger premature reaction between $(MeCp)_2Mg$ and the oxygen source or a preferential heterogeneous interaction between Mg and the oxygen species on the growth front, which results in the removal of the former from the growing surface. It should be mentioned that for VI/II ratios between 15 and 120, no major effect has been observed on the incorporation of magnesium.

The reduction in Mg content is only observed for very high VI/II ratios (≥480) and is accompanied by a strong reduction in film thickness from 2.2 to 0.9 μm. It has been suggested [141] for the growth of ZnO by MOCVD (using DEZn and TBOH) in the

temperature range 300 ˚C to 500 ˚C that an oversupply of oxygen species will prevent the adsorption of Zn species, resulting in a decrease in growth rate [235]. A similar site blocking mechanism is suspected to result in the reduced growth rate of $Mg_xZn_{1-x}O$ grown with high VI/II ratios in the present work.

Surface morphology

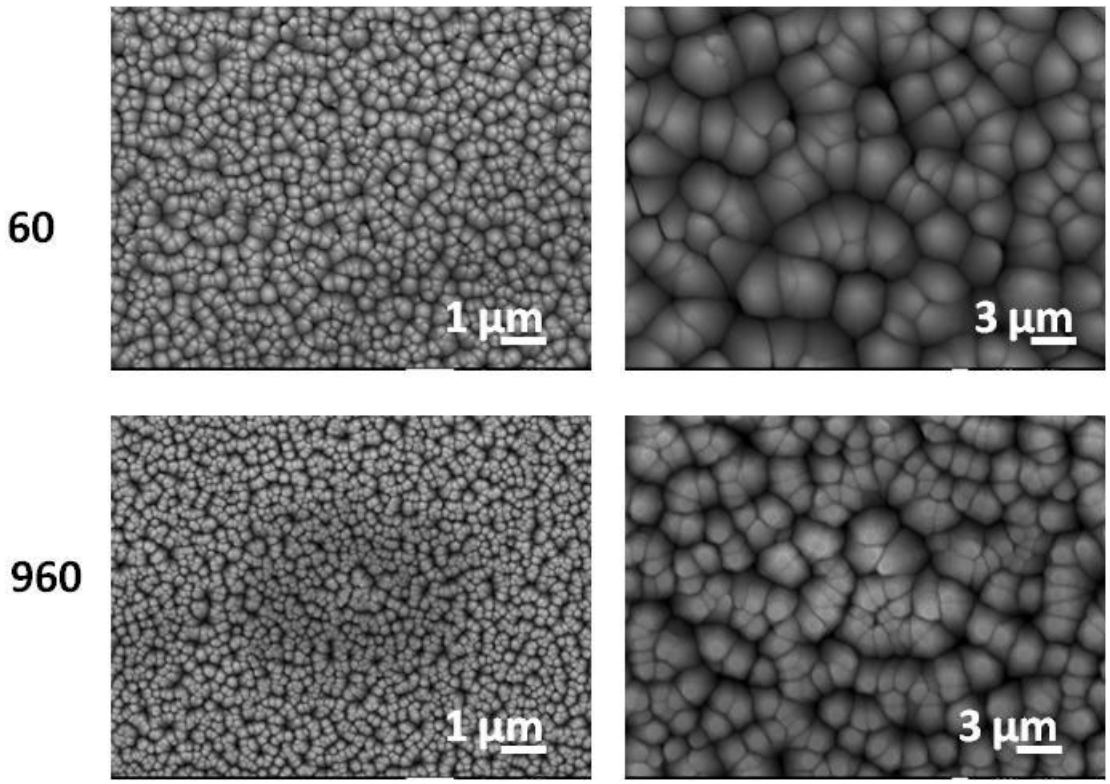

Figure 7-4 SEM micrographs showing the surface morphology of films grown with VI/II ratios of 60 and 480 using TBOH

To illustrate the morphological changes arising from a change in VI/II ratio, Figure 7-4 compares SEM images of films grown with VI/II ratios of 60 and 480. No significant difference is noted, with compact films with uniform columnar crystallites obtained. Roro *et al.* [166], as well Agouram *et al.* [141] reported similar results for ZnO films grown by MOCVD.

7.2 Mg incorporation in films grown with oxygen gas

7.2.1 Growth temperature

Photoluminescence

Figure 7-5 shows normalized PL spectra of $Mg_xZn_{1-x}O$ grown at different growth temperatures (320 ˚C to 620 ˚C) on c-Al_2O_3, using oxygen gas as the group VI source. The D^oX position varies slightly due to small differences in Mg incorporation. As was the case for growth using TBOH, stacking fault-related transitions are observed at energies below that of the D^oX line, labelled (e, A^0). No obvious trend is observed in terms of Mg incorporation or the strength of the stacking fault PL. The Mg content appears to be slightly higher at around 520 ˚C.

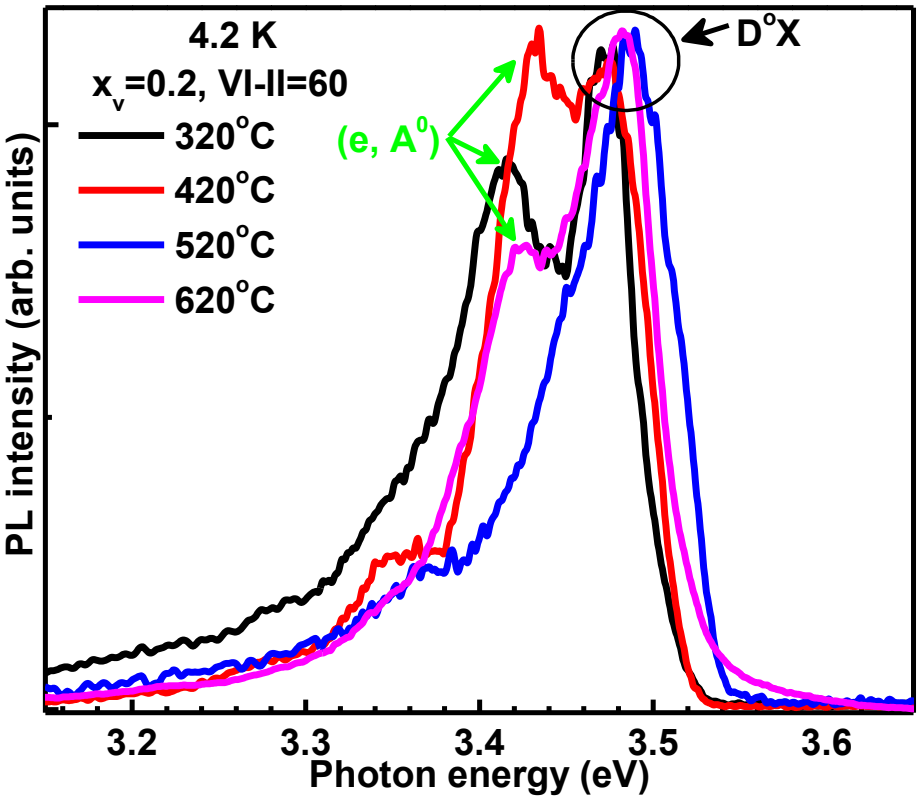

Figure 7-5 Low temperature (4.2 K) PL spectra of $Mg_xZn_{1-x}O$ films (x_v=0.2) grown on c-Al_2O_3 at temperatures ranging from 320 ˚C to 620 ˚C using O_2 as oxygen source

It has been reported that growth using $(MeCp)_2Mg$ can be performed up to 800 ˚C using either O_2 or N_2O [236]. However with TBOH, degradation of the films occurs above 500 ˚C. This is mostly due to the low reactivity and low cracking temperature of the alcohols. Although the reported growth temperature using metal alkyls range between 200 ˚C and 400 ˚C, $(MeCp)_2Mg$ seems useable up to higher temperatures, while still yielding good quality layers. The critical issue for growth at higher temperatures is the occurrence of a strong parasitic oxidation reaction between $(MeCp)_2Mg$ and the oxygen sources. This

phenomenon occurs mostly at the inlet of the reactor tube and can cause an oxygen deficiency above the substrate. There is however a large variation in published results with regards to higher temperature growth. This is most probably due to differences in the precursors used, but also due to the reactor setup (geometry and total pressure).

Surface morphology

Figure 7-6 shows SEM images of the films. The surface morphology changes significantly with substrate temperature. At 320 ˚C, uniform columnar crystals are obtained. This feature remains at 420 ˚C, but the size of the columns increases. At 520 ˚C, the surface exhibits

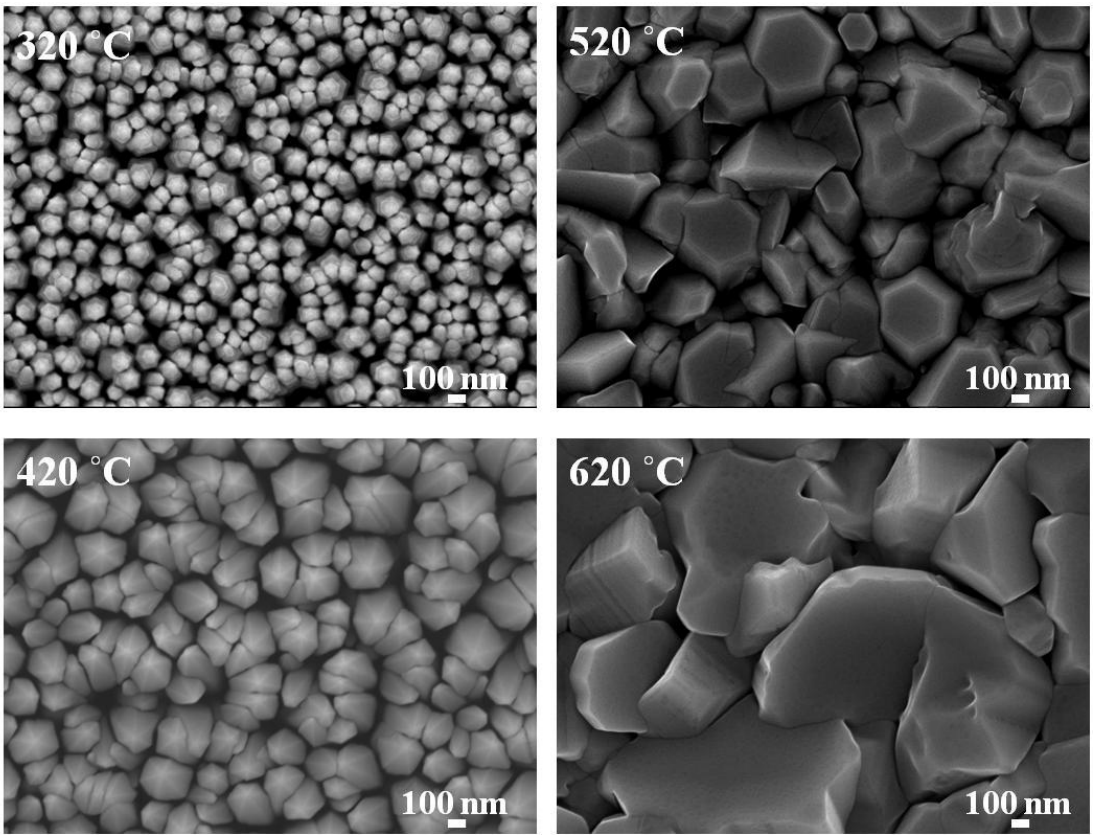

Figure 7-6 SEM images of the $Mg_xZn_{1-x}O$ films grown on c-Al_2O_3 at various temperatures using O_2 gas

faceted features with a variety of shapes. Some of these columns have the characteristic hexagonal symmetry. A further increase in temperature increases the size of the crystallites with no hexagonal columns observed. The growth temperature which seems to yield columnar growth is around 420 ˚C. This temperature has also been found to be "optimum" for growth of ZnO using O_2. EDX on the sample grown at 620 ˚C yielded a Mg mole fraction of 0.07 and XRD showed the (0002) peak to dominate for all samples.

7.2.2 VI/II ratio

Photoluminescence

Figure 7-7 shows the PL spectra (4.2 K) of $Mg_xZn_{1-x}O$ (x_v=0.2) grown with different VI/II ratio on c-Al_2O_3 at 420 ˚C. The spectra are dominated by D^oX emission. In this case, the stacking fault related transition is very small. No obvious change in Mg incorporation is detected. The VI/II ratio has no major effect on the Mg incorporation when using $(MeCp)_2Mg$.

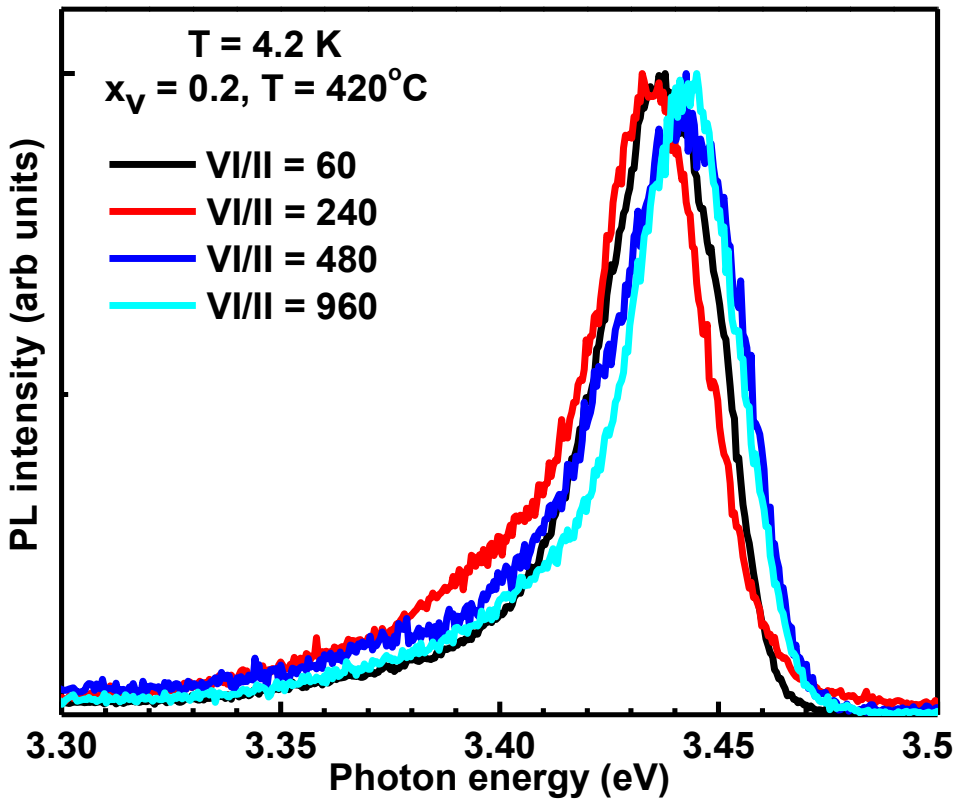

Figure 7-7 Low temperature (4.2 K) PL spectra of $Mg_xZn_{1-x}O$ films (x_v=0.2) grown on c-Al_2O_3 with different VI/II ratios and using O_2 as oxygen source

Surface morphology

Figure 7-8 shows SEM images of the films. As compared to growth using TBOH, there is no significant change in the morphology of the films. The VI/II ratio does not affect the size or the shape of the columns or crystals. In cross-sectional views (not shown), the columnar structures are observed to orient normal to the substrate, which indicates preferred growth along the c-axis. The availability of oxygen does not influence the initial nucleation stage at the interface.

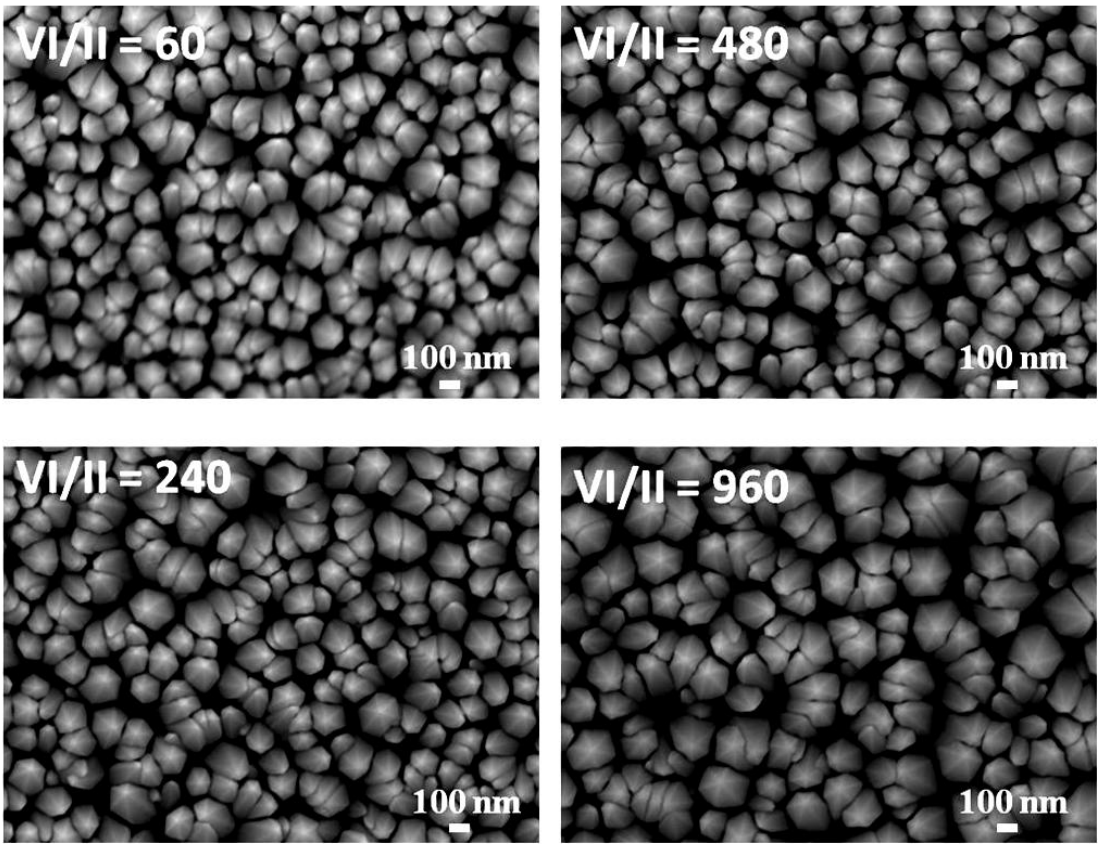

Figure 7-8 SEM images of $Mg_xZn_{1-x}O$ films grown on c-Al_2O_3 with different VI/II ratios (60-960) using O_2 gas

7.3 Comparison of films grown with TBOH and oxygen

In this section, some properties of films grown with either TBOH or O_2 as oxidizing agent will be compared. In terms of Mg incorporation, Figure 7-9 compares the PL peak positions and the FWHM of the RT PL peak of films grown with different Mg mole fractions x_v, using the two different group VI sources. The results are almost identical. The quality of films grown with either oxygen source is comparable. With regard to the incorporation of Mg, the samples grown using TBOH show a slightly higher incorporation efficiency, which could be due to pre-reactions occurring between O_2 and DEZn, depleting Mg within the growth zone.

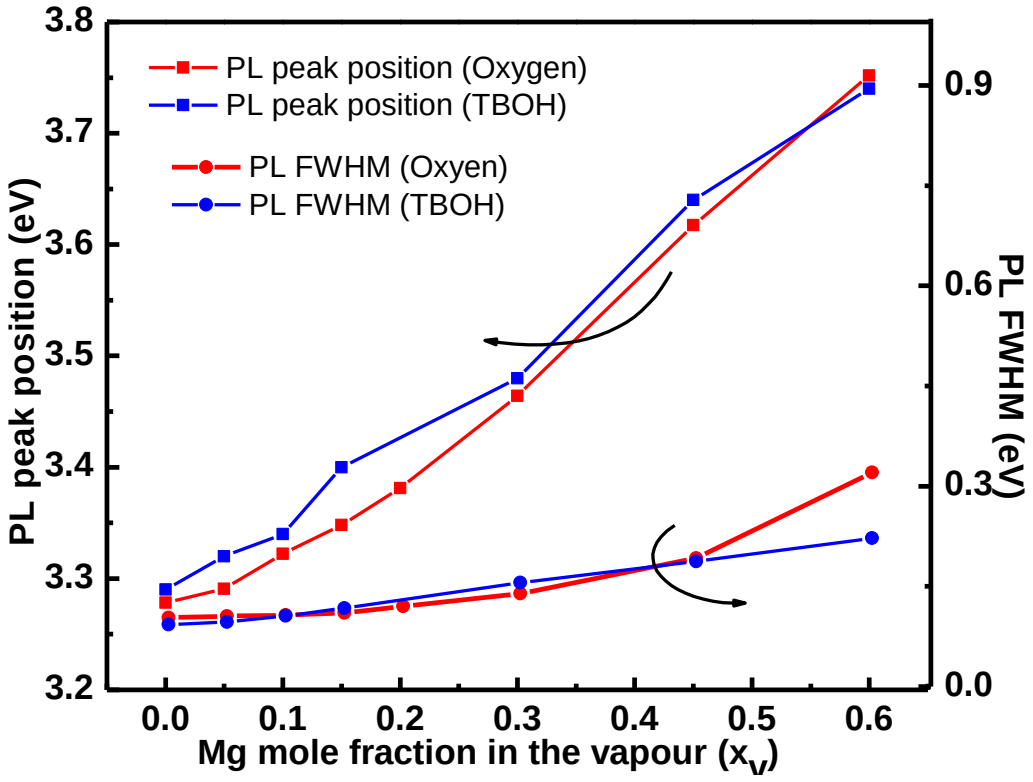

Figure 7-9 Comparison of O_2 and TBOH as oxidizing agent for $Mg_xZn_{1-x}O$ thin films grown at 420 ˚C and VI/II ratio=60: RT PL peak position and FWHM

7.4 Growth rate

Morphologies

Figure 7-10 shows cross-sectional SEM images of $Mg_xZn_{1-x}O$ grown on c-Al_2O_3 substrate at different growth rates (3.3 µm/h, 2.8 µm/h, 1.4 µm/h and 0.5 µm/h) using TBOH as group VI source and x_v=0.2. Note that the growth times were changed to keep the thicknesses of the films the same. The growth temperature was 420 ˚C. For all growth rates, the films reveal columnar growth with cone shaped ends. The size of the columns varies depending on the growth rate. For a low growth rate (0.5 µm/h), the film appears denser compared to a high growth rate (3.3 µm/h). The variations in thickness are within experimental error. The deposition rate strongly influences the initial nucleation and coalescence of the films. It seems likely that a decrease in growth rate increases the coalescence of crystallites/grains formed during the initial deposition.

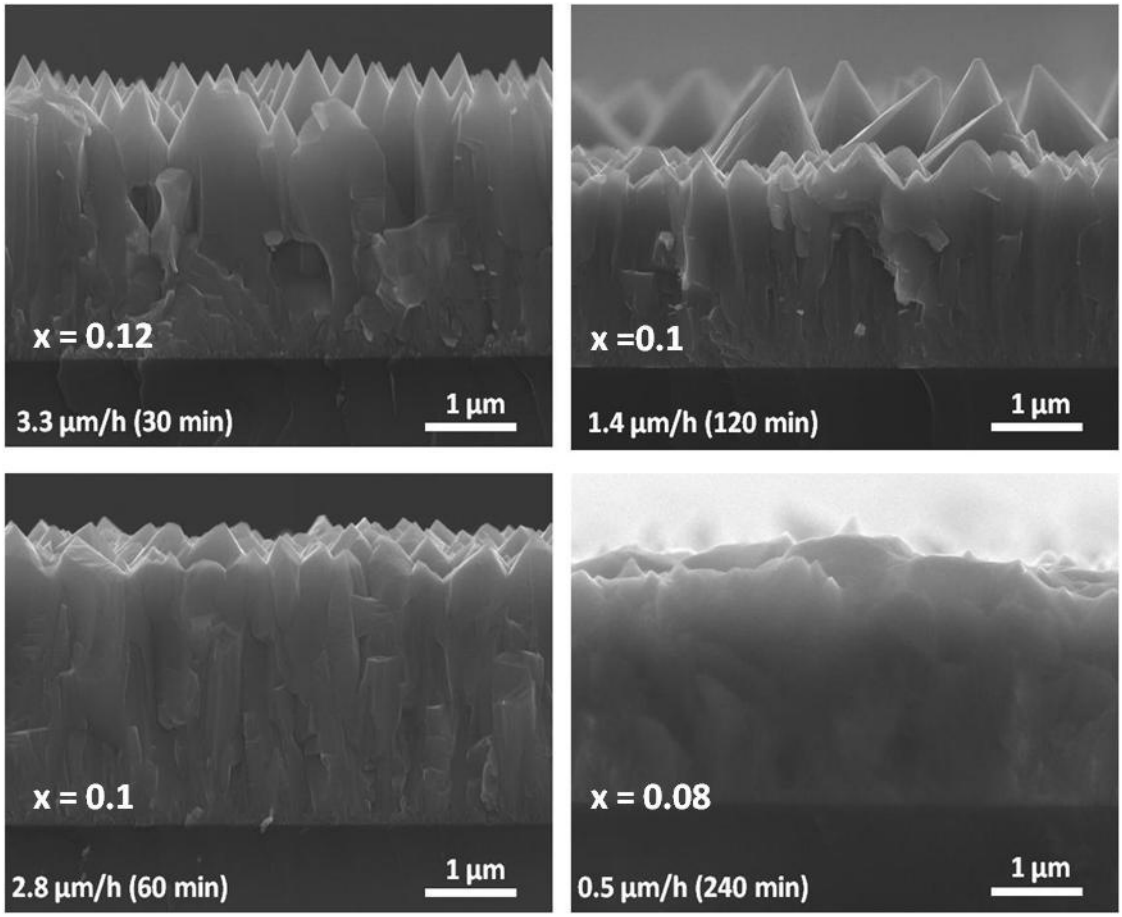

Figure 7-10 Cross sectional SEM images of $Mg_xZn_{1-x}O$ thin films grown on c-Al_2O_3 substrate at different growth rates (3.3 µm/h, 2. 8µm/h, 1.4 µm/h and 0.5 µm/h) using TBOH as oxidant

Figure 7-11 shows the surfaces of the films. For growth rates of 3.3 µm/h and 2.8 µm/h, the surface features are similar to those of ZnO films. The films comprise dense columnar crystals with the films grown at 2.8 µm/h having the smallest columns. For growth rates of 1.4 µm/h and 0.5 µm/h, the surface features are comparable to those of $Mg_xZn_{1-x}O$ films with $x \geq 0.2$ (see Chapter 5). The surfaces of these films drastically differ from those grown at higher growth rates and are also considerably rougher. The lower growth rates seem to enhance the formation of cubic structures even for low Mg mole fractions (see inserts). Similar results have been observed by Kim *et al.* [237] when growing $Mg_xZn_{1-x}O$.

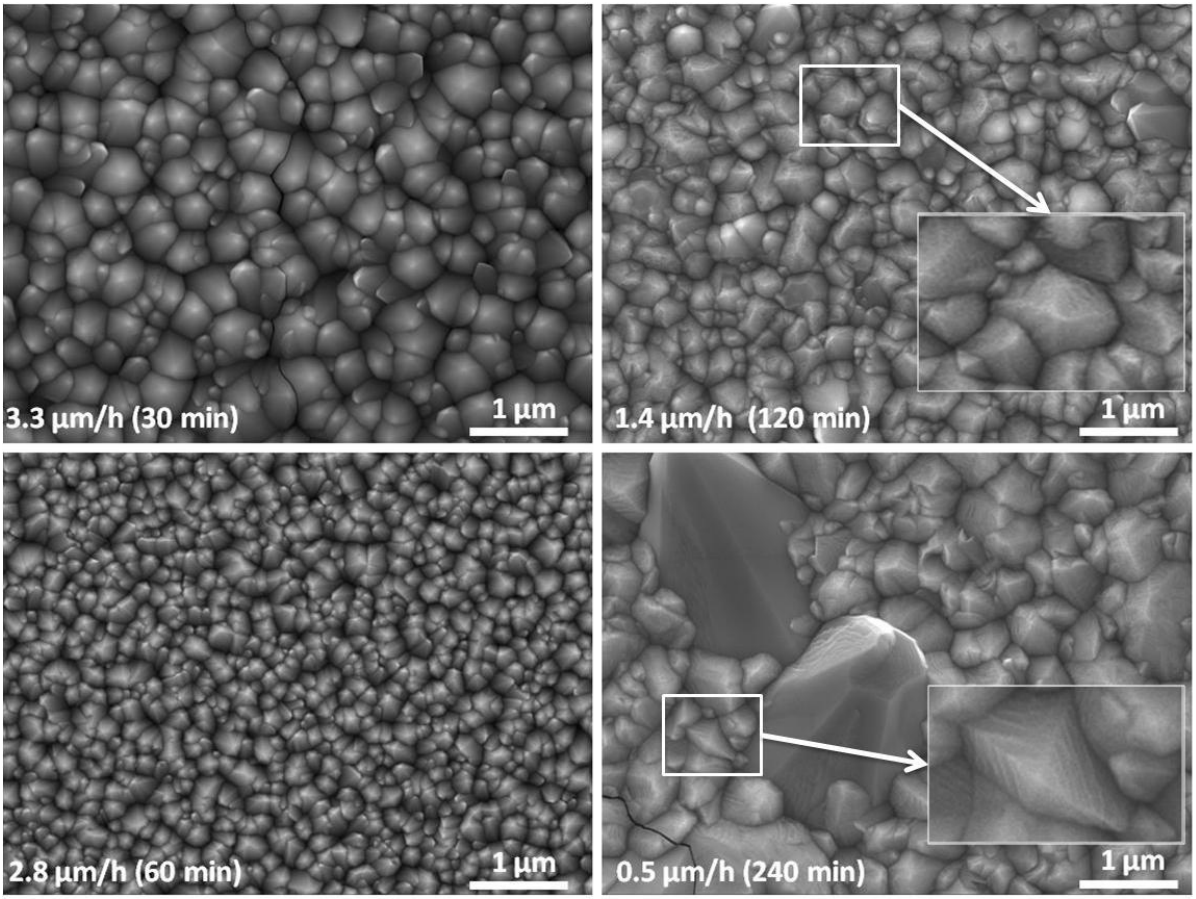

Figure 7-11 SEM images of $Mg_xZn_{1-x}O$ grown on c-Al_2O_3 at different growth rates using TBOH at 420 ˚C and VI/II ratio=60.

The lower growth rates possibly enhance the Mg deposition at the interface, causing the formation of a MgO rich layer/region, which has been observed by AES measurements on other films. The same effect was seen when growing higher Mg content films. Low growth rates seem to favour the cubic structure instead of the wurtzite structure. This is supported by the XRD spectra in Figure 7-12, which show the presence of MgO (111) peaks for films grown at lower growth rates. One can suggest that lower growth rates enhance phase segregation in the films.

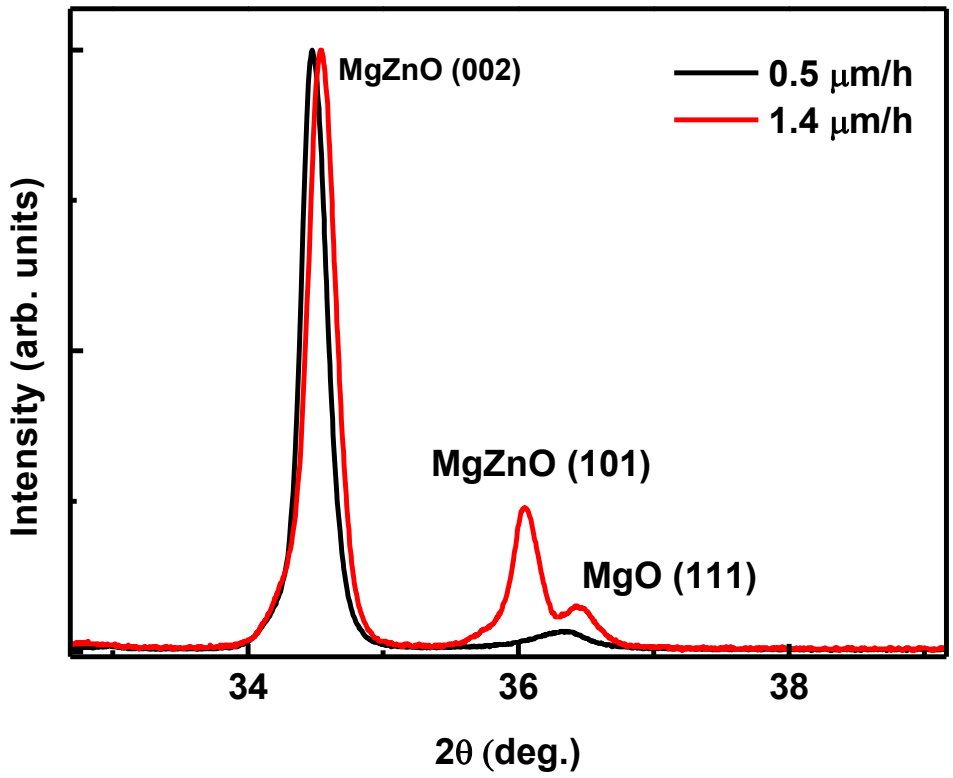

Figure 7-12 Normalized XRD spectra of $Mg_xZn_{1-x}O$ grown on c-Al_2O_3 at growth rates of 1.4 μm/h and 0.5 μm/h using TBOH, a growth temperature of 420 ˚C and VI/II ratio of 60

Photoluminescence

Figure 7-13 shows low temperature (4.2 K) normalized PL spectra of the films. It seems reasonable to assume that the dominating peak in each spectrum is the stacking fault- related transition (e, A^0) based on the results reported in sections 6.3 and 6.4. D^oX transitions appear as shoulders on the high energy side of the stacking fault PL. The sample grown at a growth rate of 0.5 μm/h seems to have two D^oX bands. For the sample grown at a rate of 1.4 μm/h, a shoulder on the lower energy side of the stacking fault PL is observed. This line is suggested to be another D^oX transition. For all samples ZnO is present in small amounts as illustrated by the presence of NBE emission at ~3.36 eV. The sample grown with the lowest growth rate (0.5 μm/h) shows the lowest Mg incorporation. This is confirmed by EDX measurements (included in Figure 7-10). The presence of two D^oX bands for the two lowest growth rates would indicate the existence of two band gaps in the films. This would correlate with the deduction made from the morphologies in Figure 7-11.

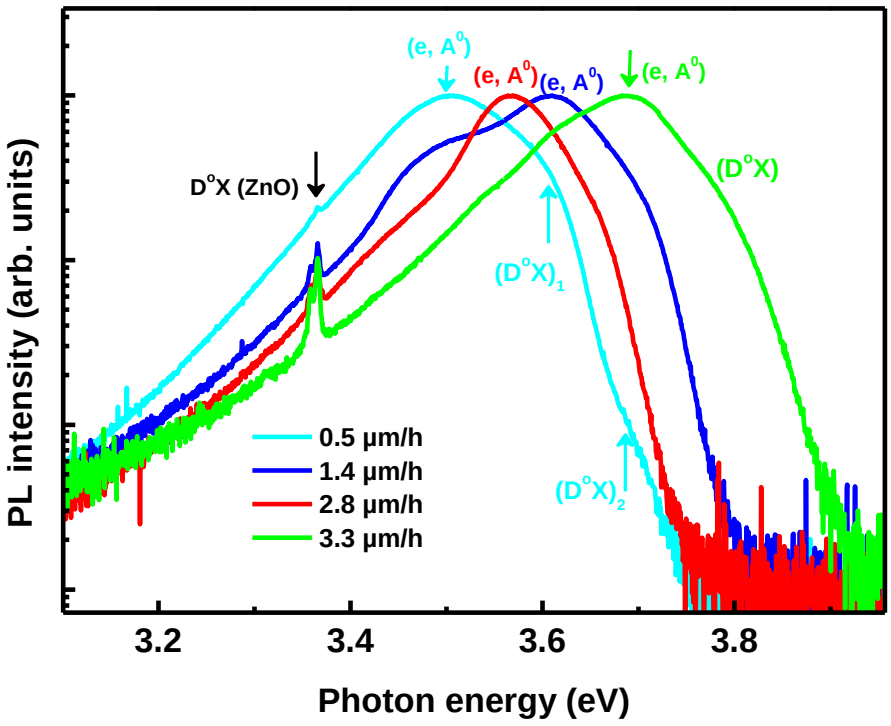

Figure 7-13 Normalized low temperature PL spectra (4.2 K) of $Mg_xZn_{1-x}O$ grown on c-Al_2O_3 at different growth rate (3.3 µm/h, 2.8 µm/h, 1.4 µm/h and 0.5 µm/h) with VI/II ratio of 60 and at substrate temperature of 420 ˚C

In MOCVD the growth rate is proportional to the flux of atoms being transported, usually by diffusion, in the gas phase to the interface, which is identical to the flux of atoms crossing the interface into the solid [107]. The growth rate is mainly mass transport limited. Since the growth rate depends on the flow rates of group II species, then the type of source will strongly influence the growth process. For example, Leys *et al.* [238] explained the cause of the lower incorporation efficiency of P in $GaAs_xP_{1-x}$ to be dependent on growth rate, which influences the dwell time of As and P species on the surface. They attributed the lower incorporation efficiency of P to differences in the adsorption/desorption rate constants of the As and P species on the surface. For InGaN, because of the higher desorption rate of indium, its incorporation efficiency is relatively low at low growth rates. As the growth rate increases, the desorption rate of indium is significantly reduced, due to the faster completion of the next layer, and consequently a higher indium incorporation efficiency will be obtained [239]. Similar behaviour for Mg is suspected. From the results there is a trend of increased efficiency of Mg incorporation for higher DEZn flow rates. It is believed that during the growth of $Mg_xZn_{1-x}O$ the transport of $(MeCp)_2Mg$ to the growth front depends strongly on the presence of DEZn. This observation is based on the fact that $(MeCp)_2Mg$ and TBOH does

not produce any MgO deposition on the substrate for the entire range of growth parameters studied. Due to the lower flow rate of DEZn at low growth rates, the availability of Mg is significantly decreased on the growth front.

7.5 Buffer layer

Morphology

Figure 7-14 (a) shows top view and cross sectional SEM images of $Mg_xZn_{1-x}O$ (x_v=0.2) layers grown on c-Al_2O_3 without a buffer layer (i), with a 5 min ZnO buffer layer (ii), and with a 10 min ZnO buffer layer (iii). The buffer layers were grown at 280 ˚C and a VI/II ratio at 60 using TBOH as oxidant. The $Mg_xZn_{1-x}O$ films were grown at 420 ˚C with the same VI/II ratio and oxidant. The thicknesses of the buffer layers are ≤200 nm. All films exhibit columnar structures with cone shaped ends. The columns are larger for the samples where a buffer layer was included. This is often observed for $Mg_xZn_{1-x}O$ grown on a ZnO buffer layer. Muthukumar *et al.* [136] showed that the ZnO buffer layer induces smoother and denser $Mg_xZn_{1-x}O$ film, while films without a buffer layer grow in columnar fashion. The low temperature ZnO buffer layer provides a high-density of growth sites, which recrystallize when the final film is grown. This causes an enhancement in lateral growth. Our results confirm the reported behaviour of $Mg_xZn_{1-x}O$ on a ZnO buffer layer, since the buffer layer is seen to enhance lateral growth more than vertical growth. Heitsch *et al*. [203] showed that the deposition of $Mg_xZn_{1-x}O$ thin films on an approximately 30 nm thick ZnO buffer layer does not improve the surface morphology. Compared with $Mg_xZn_{1-x}O$ films grown directly on Al_2O_3, the deposition of $Mg_xZn_{1-x}O$ films on ZnO yielded higher Mg concentrations in the final films in the present. This indicates that ZnO increases the availability of sites, where $(MeCp)_2Mg$ can attach. The six faces at the ends of the columns are more pronounced for the samples which include a buffer layer, indicating the retention of the wurtzite structure. This is in good agreement with the findings of Tanaka *et al.* [240], who observed that a ZnO buffer layer forces the wurtzite structure of the subsequent films.

Figure 7-14 (b) shows the cross sectional and top view SEM images of a $Mg_xZn_{1-x}O$ thin film (x_v=0.5) grown directly on Al_2O_3 substrate (i), grown on a 5 min $Mg_xZn_{1-x}O$ buffer layer (x_v=0.5) (ii) and on a 5 min ZnO buffer layer (iii). For the film grown on the ZnO buffer layer (cross sectional view) the buffer is clearly distinguished from the final film. As for the sample with lower Mg content (x_v=0.2), the column width increases when a buffer is included due to

enhanced lateral growth in the final film. The morphology is typical for high Mg content films

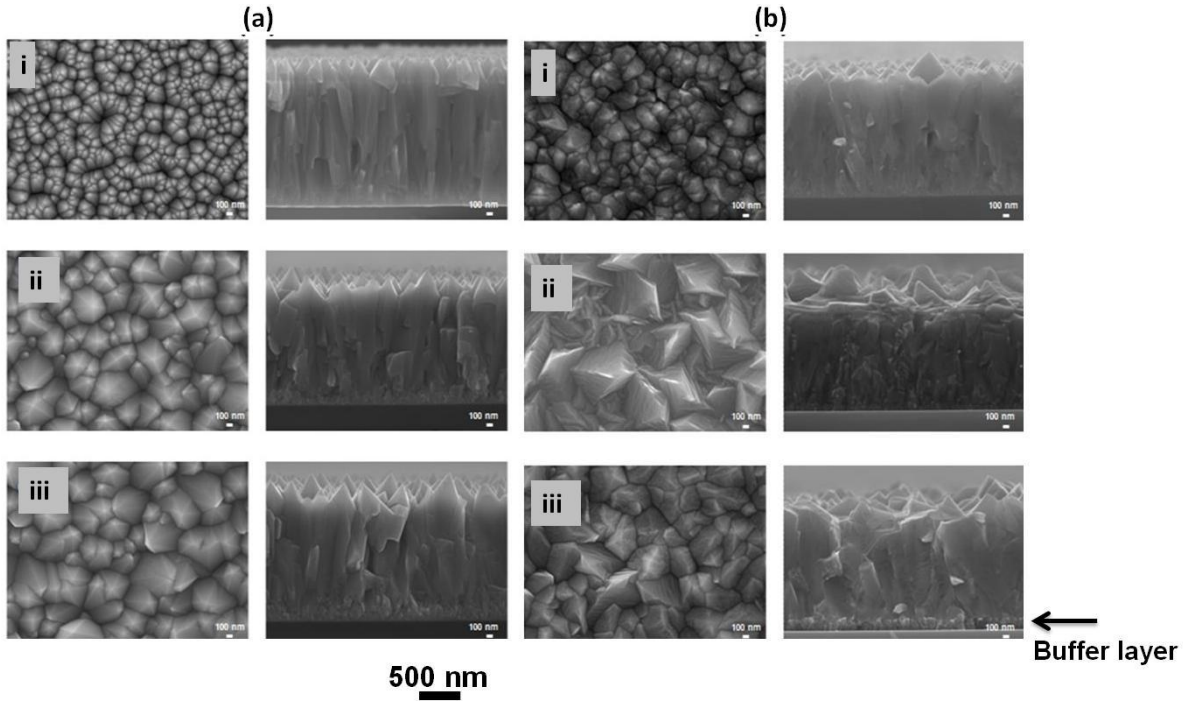

Figure 7-14 (a) Top view and cross sectional SEM images of $Mg_xZn_{1-x}O$ (x_v=0.2) at 420 ˚C for 1h, without a buffer layer (i) with a 5 min ZnO buffer layer grown at 280 ˚C (ii) and with a 10 min ZnO buffer layer grown at 280 ˚C (iii). (b) Top view and cross sectional SEM images of $Mg_xZn_{1-x}O$ (x_v=0.5) grown at 420 ˚C without buffer layer (i) on a 5 min $Mg_xZn_{1-x}O$ buffer layer (x_v=0.5, at 280 ˚C) (ii), and on a 5 min ZnO buffer layer (iii)

with a tendency for pyramidal shaped crystals, which could indicate the presence of cubic material. The buffer layer seems to lead to rougher surfaces with small steps seen on the crystallites. These small steps are created by successive stacking of (11.0) planes, which are vertically oriented and (0001) planes which are horizontally oriented. Due to the relatively thick buffer layer the surface morphology of the $Mg_xZn_{1-x}O$ films are rough, which is caused by a decrease in the density of nuclei on the buffer surface [241]. It is known that higher densities of small nuclei promote grain coalescence, yielding flat and smooth surfaces of the final layer. The above results, especially the increase in column size, are in agreement with the results of Kim *et al.* [237] who showed an increase in surface roughness and column size of $Mg_xZn_{1-x}O$ films (for x=0.5) grown on a MgO buffer.

The use of a ZnO buffer layer is to overcome phase segregation occurring for high Mg content. Several reports on MBE material [237, 240, 242] have shown the possibility to

maintain the wurtzite structure up to x=0.5. This is done by using a very high quality buffer layer, which acts as a wurtzite template. In our case, the buffer does not seem to improve the crystal quality or to maintain the wurtzite structure, probably due to poor quality of the buffer layer. The thickness of the buffer is also critical to the final film. In our case the thickness is ~200 nm, which is believed to be too thick for an efficient result. Fujita *et al.* [243] claimed that the first 15-25 nm $Mg_xZn_{1-x}O$ (x>0.5) remains wurtzite before changing to the rocksalt structure. Similar results were found by Muthukumar *et al.* [136], showing the importance of the thickness of the buffer layer.

7.6 Effect of annealing on $Mg_xZn_{1-x}O$ thin films

The crystal quality of ZnO and $Mg_xZn_{1-x}O$ depends not only on the growth process but also on the post growth heat treatments, which play a significant role in the improvement of the quality of the films. Annealing is mainly used because the compositional homogeneity of the material can be improved and the concentration of the non-radiative defects decreased [244]. Despite numerous investigations of the effects of annealing on various properties of ZnO, little attention has been paid to $Mg_xZn_{1-x}O$ thin films and only a few papers have been published [245-248]. Annealing of $Mg_xZn_{1-x}O$ is useful to improve the morphological, crystalline an optical qualities for the fabrication of optoelectronic devices.

In this section, the effects of annealing in oxygen ambient on the optical properties of $Mg_xZn_{1-x}O$ films are briefly investigated. The behaviour of the free to bound transition related to stacking faults has been carefully examined, since this band (for ZnO) has been reported to be very unstable when annealing is performed [249]. The donor bound exciton attributed to Al incorporation into the films, either through diffusion from the substrate and/or from precursors, is also studied.

$Mg_xZn_{1-x}O$ films were deposited on c-Al_2O_3 substrates using oxygen as oxidant. The VI/II ratio was fixed at 60 (optimum for ZnO growth in our reactor). The Mg/Zn ratio was varied in order to change the Mg content in the vapour phase. Films were deposited at 420 ˚C for 45 min (yielding films ~1-2 µm in thickness). The samples were annealed in oxygen ambient at various temperatures (420 ˚C, 520 ˚C, 620 ˚C, 720 ˚C and 820 ˚C) for 2 hrs. The use of oxygen is dictated by the fact that oxygen ambient seems to be more promising for improving the luminescent efficiency [49].

NBE emission

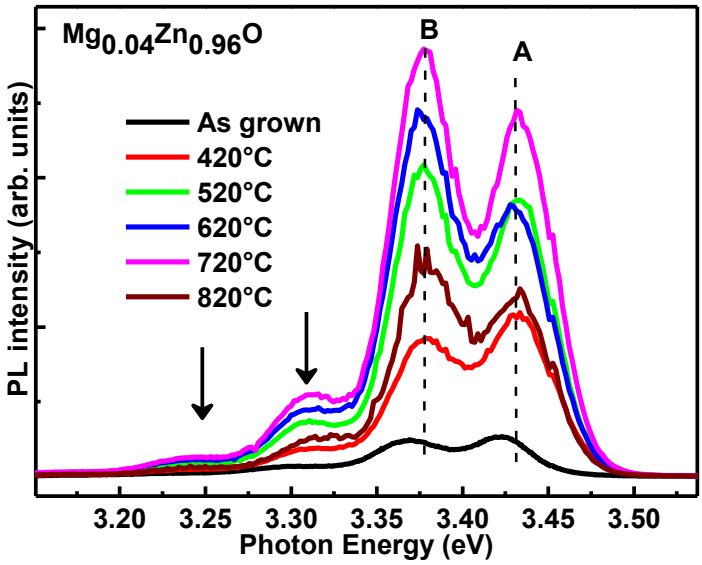

Figure 7-15 PL spectra (85 K) of $Mg_{0.04}Zn_{0.96}O$ grown on c-Al_2O_3 and annealed for 2 hours at 420 ˚C, 520 ˚C, 620 ˚C, 720 ˚C and 820 ˚C in O_2 gas

Figure 7-15 shows 85 K PL spectra of $Mg_{0.04}Zn_{0.96}O$ before and after annealing. The spectra contain two main peaks, labelled A and B, ascribed to D^oX (A) and stacking fault-related (e, A^0) transitions (B). The two smaller peaks (indicated by arrows) are phonon replicas of the free to bound (e, A^0) transition. The PL intensity increases upon annealing (up to 720 ˚C) and then drops after annealing at 820 ˚C, suggesting that non-radiative recombination increases in the sample. The FWHM of the D^0X line slightly decreases (from 41 meV to 34 meV) with increasing temperature, which implies that the crystalline quality improves with temperature. The same was observed for the (e, A^o) transition (FWHM decreases from 38 meV to 35 meV). These values were extracted from Gaussian curve fitting. After annealing at 420 ˚C a slight shift (~10 meV) of the entire spectrum to higher energies is observed. This might be due to several reasons: out-diffusion of Zn atoms which will increase the Mg concentration in the group II sublattice, a release of tensile strain, which will increase the band gap energy, etc. A further increase in the annealing temperature does not affect the energy positions. In ZnO, the NBE emission depends strongly on the crystal quality. However, annealing does not affect the band gap. Ju *et al.* [245] have reported that annealing decreases the amount of Zn in $Mg_xZn_{1-x}O$ due to the fact that redundant Zn, originally at interstitial sites in the as-grown material, is removed upon annealing at 550 ˚C. This yields a relatively stable composition. Jiang *et al.* [250] observed that the band gap increases with

annealing temperature up to 720 ˚C, and then decreases. They assigned this behaviour to the displacement (at lower T) and the effusion of Mg atoms from the films (at higher T).

The stacking fault-related PL slightly increases relative to the D^oX line with increasing annealing temperature (up to 620 ˚C) and decreases upon a further increase in temperature. Wurtzite stacking fault energies are known to drastically reduce when increasing the unit cell c/a ratio. At lower temperature, the relief of in plane tensile strain by annealing will cause an increase in the c/a ratio and subsequently the stacking fault density. In addition, it has been shown that ZnO epi-films exhibit significant improvement upon thermal annealing and intrinsic types of basal plane stacking faults are the predominant structural defects in the ZnO after thermal treatment [251].

Deep level emission

Figure 7-16 shows the complete PL spectra (85 K) of the samples annealed at different temperatures, illustrating an increase in the deep level emission (DLE) with increasing annealing temperature. Several LO phonon replicas of the (e, A^0) transition are indicated by arrows. The DLE of the as-grown film has been fitted with two Gaussian peaks, one at ~2.22 eV and another one at ~2.48 eV. If one considers the spectrum to be blue-shifted by ~65 meV due to Mg incorporation (extracted from the shift in the D^oX line) the peak at 2.22 eV will correspond to a peak at ~2.15 eV in ZnO. This peak at ~2.15 eV in ZnO has been ascribed to Li-related band [252, 253]. The peak at ~2.48 eV for $Mg_{0.04}Zn_{0.96}O$ corresponds approximately to 2.415 eV for ZnO, which is believed to arise from a substitutional Cu_{Zn}-related acceptor [254, 255]. The Cu_{Zn}-related transition increases in intensity as the annealing temperature is increased. Reshchikov *et al.* [254] showed that annealing at temperatures above 600 ˚C resulted in a strong enhancement of the Cu-related green luminescence band due to a notable increase in the concentration of Cu_{Zn} acceptors. The Cu mainly originates from the annealing furnace. A transition at around ~2.4 eV in ZnO was also reported to increase with annealing temperature (400 ˚C to 950 ˚C) [256].

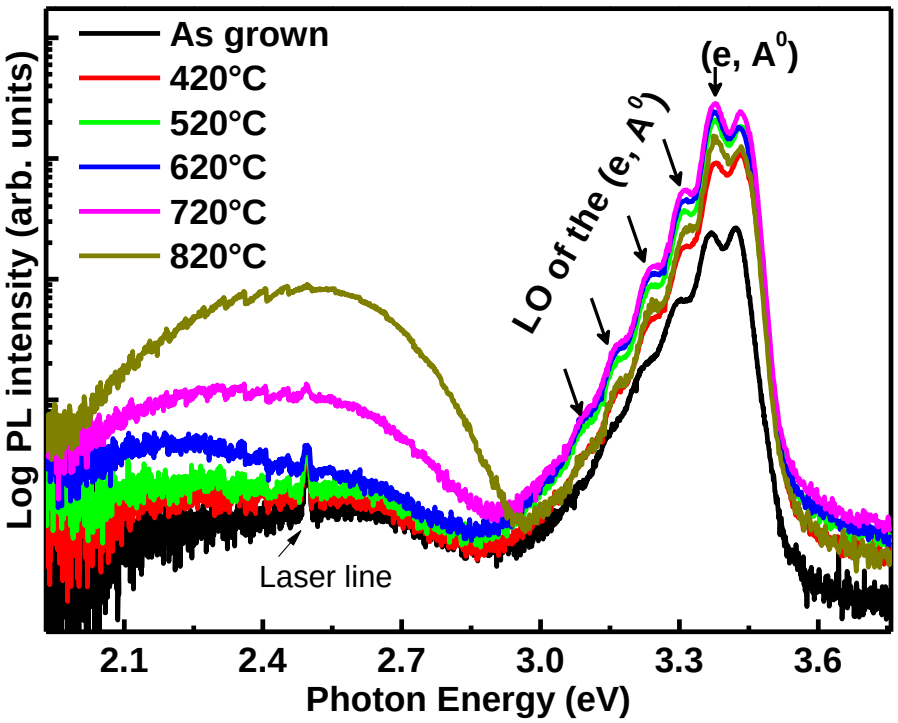

Figure 7-16 PL spectra (85 K) of $Mg_{0.04}Zn_{0.96}O$ grown on c-Al_2O_3 and annealed for 2 hours at 420 ˚C, 520 ˚C, 620 ˚C, 720 ˚C, and 820 ˚C using O_2 gas

7.7 Conclusions

The effects of various growth parameters (growth temperature, VI/II ratio, growth rate, buffer layer and annealing temperature) on the properties of $Mg_xZn_{1-x}O$ films have been studied.

Lower growth temperatures (≤280 ˚C) resulted in a lower decomposition rate of the metalorganic precursors and a low surface mobility of adsorbed reactant species, leading to poor quality films. The Mg incorporation at these temperatures was slightly reduced, possibly due to incomplete decomposition of $(MeCp)_2Mg$. Also, the surface was almost featureless and the material appeared amorphous with small crystallites. Higher temperatures (480 ˚C) improved the surface morphology and yielded uniform columnar structures with strong c-axis orientation. The optimum temperature for the growth of $Mg_xZn_{1-x}O$ in our reactor is between 380 ˚C and 480 ˚C.

High VI/II ratios decreased the Mg incorporation, possibly due to a stronger premature reaction between $(MeCp)_2Mg$ and the oxidant, or a preferential heterogeneous interaction between the Mg and oxygen species on the growth front. Also, the stacking fault density was deduced to increase. The surface morphology was independent on the VI/II ratio. A site blocking mechanism was suggested to result in reduced growth rates of $Mg_xZn_{1-x}O$ grown at

high VI/II ratios (≥240). For VI/II ratios between 15 and 120, no major effect has been observed on the incorporation of magnesium.

Films grown with either TBOH or O_2 had similar optical quality, but the use of TBOH as oxygen precursor led to a slightly more efficient Mg incorporation.

$Mg_xZn_{1-x}O$ grown on a ZnO buffer layer (at 280 ˚C) had slightly higher levels of Mg but smaller crystallites. The Mg incorporation depended strongly on the DEZn flow rate and higher growth rates increased the incorporation of Mg. The buffer did not seem to improve the crystal quality or to maintain the wurtzite structure, probably due to poor quality.

For all growth rates, the films revealed columnar structures with cone shaped ends. The size of the columns varied depending on the growth rate. For the lowest growth rate (0.5 μm/h), the film appeared denser compared to the highest growth rate (3.3 μm/h). The low temperature PL spectrum of the sample grown at a growth rate of 0.5 μm/h contained what appeared to be two D^oX bands, possibly indicating non-uniform composition, i.e. the existence of two band gaps in the film. The incorporation of Mg increased with growth rate.

The effect of annealing on $Mg_xZn_{1-x}O$ films deposited on Al_2O_3 substrate was investigated. The film quality was found to degrade at annealing temperature >720 ˚C. In addition, thermal treatment at a temperature >400 ˚C enhanced the overall emission intensity.

Chapter 8 Conclusions and future work

8.1 Conclusions

This thesis presents a comprehensive growth study of ZnO and $Mg_xZn_{1-x}O$ thin films by metal organic chemical vapour deposition (MOCVD).

$Mg_xZn_{1-x}O$ thin films were grown on c-sapphire Al_2O_3 and silicon (100) substrate at a reactor pressure of 20 Torr. For the group II element, diethylzinc (DEZn) and bis-(methylcyclopentadienyl)-magnesium ($(MeCp)_2Mg$) were used as Zn and Mg sources, respectively. For the group VI element, tertiary butanol (TBOH) and oxygen gas (O_2) were used as oxygen sources. Characterization by XRD, SEM, PL, AES and TEM provided valuable information regarding the structural and optical properties, as well as the distribution of Mg in $Mg_xZn_{1-x}O$ thin films. The main purpose of this work was to gain a better understanding of Mg incorporation into ZnO, as well as to study the effect of growth parameters such as growth temperature, growth rate, VI/II ratio and the inclusion of a buffer layer on the above-mentioned properties of the material.

Before proceeding with the study of $Mg_xZn_{1-x}O$, it was necessary to optimize certain parameters related to the growth of ZnO thin films. It is essential to be able to have optimum growth parameters for the binary before attempting to incorporate Mg. Thus, the effect of different substrates on the properties of ZnO thin films using oxygen gas as oxidizing agent was studied. It was found that increasing the growth temperature from 380 ˚C to 680 ˚C led to morphological changes, with the films composed of nanostructures ranging from narrow columnar crystallites to nanorods (width ~200 nm). A concomitant increase in density of structural defects was observed. An increase in the VI/II ratio from 60 to 960 promoted lateral growth, which caused an increase in the size of the columnar crystallites. DEZn was found to react more efficiently with oxygen as the growth temperature increased. The optimum growth parameters were found to be a VI/II ratio of 60 and a temperature of 480 ˚C, which gave denser and more uniform ZnO films. The effect of various substrates (Si, glass, ZnO and Al_2O_3) was also investigated prior to $Mg_xZn_{1-x}O$ growth. All the substrates yielded a strong degree of c-axis orientation, with grain sizes being largest for growth on ZnO, sapphire (c- and r-plane) and Si (100) substrate. The surface morphologies were observed to be qualitatively similar, with GaAs yielding the largest hexagonal columns. Furthermore, the

low temperature PL spectra were qualitatively similar, with glass and silicon (both (100) and (111)) yielding higher stacking fault densities in the ZnO films.

This preliminary study provided the necessary background to the growth of $Mg_xZn_{1-x}O$. Mg was successfully incorporated into ZnO. The results confirmed the substitution of Mg on the group II sub-lattice. It was found that the incorporation of Mg slightly reduced the c-axis lattice parameter of ZnO films: a reduction from 5.205 Å (x=0) to 5.17 Å (x=0.39) was determined.

For both oxygen sources, the surface morphology was found to be affected by the incorporation of Mg atoms. The morphologies for layers with low Mg content were typified by columnar structures with cone shaped ends. For higher Mg content, cubic faceted crystallites were observed, revealing the presence of the segregation of cubic and hexagonal phases occurring during growth. PL showed a blue-shift of the FX line, corroborating the widening of the ZnO band gap. The spectral positions of the room temperature PL peak and optical band gap were successfully tuned from 3.3 eV to 4 eV by adjusting the Mg content. Both the FWHM of the (0002) XRD peak and of the PL lines were seen to increase with Mg content. This was ascribed to alloy broadening, inhomogeneous strain, dislocations and finite domain size effects. An important phenomenon to note in this work regarding the optical properties, is the presence of emission assigned to stacking faults. These stacking faults have been seen to increase with increased Mg incorporation in the films. TEM substantiated this result. Another very interesting phenomenon is the formation at the interface of a Mg enriched layer. This layer, for the growth on sapphire (0001), was found to be a mixture of Mg, Al and O, which probably indicates the formation of the spinel $MgAl_2O_4$. Growth on silicon (100) led to the formation of a thin MgO layer (~2 nm) at the interface. Compositional mapping (in cross section) revealed strong non-uniformity of the distribution of the Mg atoms with depth. Compositional line scans using TEM showed a decrease in the Mg content as the film thickness evolves.

The effect of growth temperature was studied in the range of 280 ˚C to 620 ˚C, for both oxygen sources, namely TBOH and O_2. The growth temperature study demonstrated the importance of temperature on the growth of $Mg_xZn_{1-x}O$. A temperature of 420 ˚C was found to be optimal for both oxygen sources, as lower temperatures were found to be inefficient for Mg incorporation and higher temperatures led to inferior structural and optical quality.

The influence of the VI/II ratio in the reactor on the properties of $Mg_xZn_{1-x}O$ thin films was also investigated. No major effect was observed at low VI/II ratio (≤120). For high VI/II ratios (≥480) a reduction in Mg content and reduction in the growth rate was observed. In addition, an increase in the VI/II ratio increased the stacking fault-related PL emission. For both oxidizing agents, the surface morphology was not severely affected by the VI/II ratio. The optimum VI/II ratio, for the growth of $Mg_xZn_{1-x}O$ thin films in our reactor is 60, yielding reasonably good quality films with fewer stacking faults.

One of the most critical parameters for the growth of $Mg_xZn_{1-x}O$ thin films encountered during this study was the effect of the reactor pressure. Indeed, $(CpMe)_2Mg$, DEZn and $TBOH/O_2$ at high pressure (≥250Torr) reacted strongly in the vapour phase, yielding $Mg(OH)_2$ only.

The effect of including a buffer layer was studied in order to try and improve the quality of the films. A ZnO buffer (≤200 nm) grown at 280 ˚C increased the Mg incorporation efficiency. However, the buffer layer did not reduce the stacking fault density, nor did it change the morphology of the final film. Finally, the growth rate was investigated. Low growth rates led to a reduction in Mg incorporation and rougher, but denser films. The PL spectra of the films also showed the presence of two D^oX lines, indicating the existence of two band gaps in the films

The effect of annealing on $Mg_xZn_{1-x}O$ films deposited on sapphire substrate was investigated. The film quality was found to degrade at annealing temperatures above 720 ˚C. In addition, the UV emission intensity as well the intensity ratio of the deep level/UV emission was enhanced. Annealing above 400 ˚C also slightly increased the Mg content in the film due to out-diffusion of Zn and to tensile strain relief.

The temperature dependent PL of ZnO and $Mg_{0.05}Zn_{0.95}O$ was investigated. The temperature dependence of the D^oX PL line was described within the context of localization in a disordered alloy potential. $Mg_xZn_{1-x}O$ films appeared to have high densities of stacking faults, with spectra significantly broadened upon an increase in the Mg content. It was found that a random distribution of cations cannot explain the line broadening, while clustering overestimated the PL line broadening. It has been suggested that the presence of stacking faults could be one of factors that contribute to line broadening. HRTEM was used to confirm the presence of type I basal plane stacking faults in the $Mg_xZn_{1-x}O$ films.

8.2 Future work

A number of questions regarding $Mg_xZn_{1-x}O$ grown by MOCVD and its characterization have been addressed in this thesis. However, several topics remain unsolved and further investigations need to be completed in order to produce device quality material. Future work should include:

- ✓ Further studies of the formation of the interfacial layer.
- ✓ Better control of the thickness and optimization of the ZnO buffer layer in order to improve the surface quality of the final films.
- ✓ Detailed understanding of the underlying mechanism controlling the observed morphology.
- ✓ Studies to establish the formation mechanism of the stacking faults in order to reduce their density.

Appendix

Problems encountered with Mg incorporation

Initial experiments in the current reactor focused on the growth of MgO, in order to establish whether Mg reaches the substrate. At the start of the project the $(MgCp)_2Mg$ line and fast switching manifold were not heated, and a single inlet reactor tube was used. The reactor pressure was ~250 Torr and TBOH was used as group VI source. The growth temperature was varied between 200 ˚C and 600 ˚C, the VI/II ratio between 30 and 120 and the growth time from 30 min to 2h per growth run. No deposition was observed on the substrate or on the reactor wall (quite unlike the case of ZnO growth in the same reactor). Several problems were encountered during these attempts to deposit MgO. These were primarily related to the absence of line heating, causing blockages due to the condensation of the precursor.

To avoid condensation in the $(MgCp)_2Mg$ line and the fast switching manifold, these parts of the system were heated between 40 ˚C to 80 ˚C and the same experiments were repeated as above. Still no deposition on the substrate was observed.

Another oxidant namely oxygen gas was used for the first time in our rector. No deposition was observed. It was concluded that the Mg precursor was not reaching the substrate when using a single inlet reactor tube due to pre-reactions between $TBOH/O_2$ and $(MgCp)_2Mg$, either inside the manifold or the line leading from there to the quartz tube.

One possible solution was to dissolve the $(MgCp)_2Mg$ in a suitable solvent, then force the mixture through a liquid flow controller (using an inert gas to pressurize the stainless steel container holding the mixture) and then subsequently vaporize the liquid in a heated mixing chamber prior to introducing it into the reactor. An easier and cheaper option, given the gas delivery system on our MOCVD, was use a so-called “pusher gas”, which joins the line downstream from the Mg source. The function of this line would be to dilute the Mg vapour and transport it at high velocity (using a small diameter stainless steel tube) to the manifold. This modification, together with a considerable increase in the line temperature and reduction in length of all the stainless steel tubing transporting Mg vapour to the fast switching manifold could lead to an increase in the vapour pressure arriving to the substrate.

Subsequent to the above changes (see figure 1), deposition was finally observed on the substrates, albeit very thin. The VI/II ratio strongly influenced deposition (high VI/II ratios

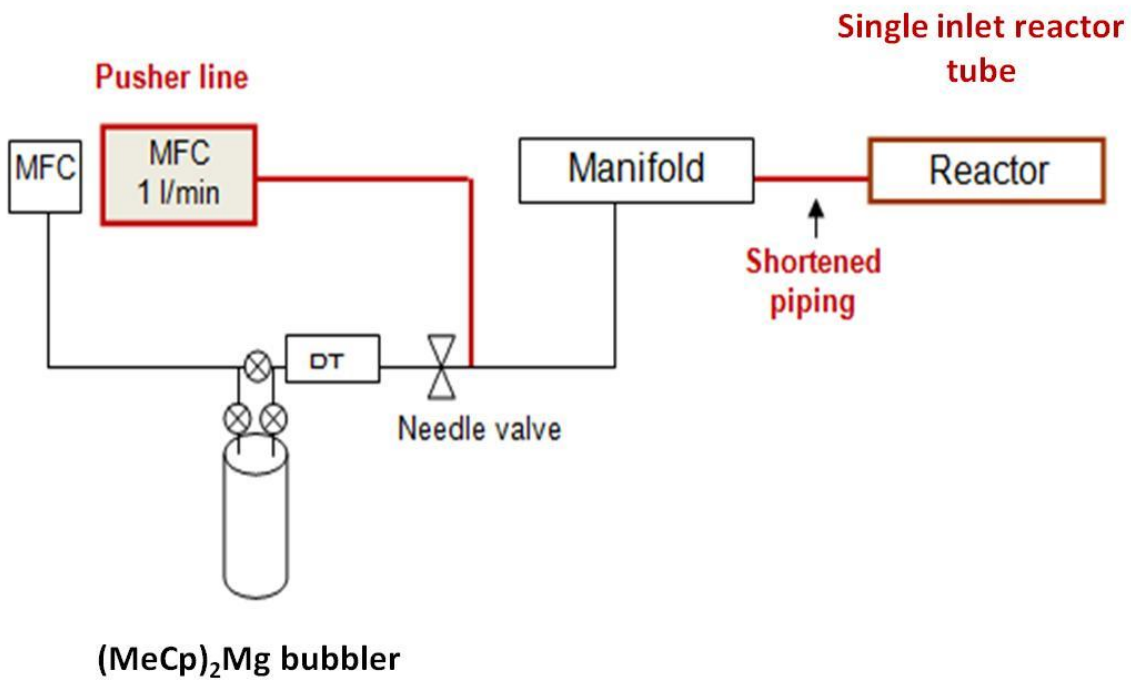

Figure 1 Schematic showing the modified status of the Mg line on our reactor

led to NO deposition, possibly due to gas phase reactions). Further experiments on the influence of temperature and VI-II ratio on the growth of MgO yielded no success in terms of MgO deposition at high pressure (250 Torr). However, a powder deposit in the tube between the fast switching manifold and reactor inlet as well as in the fast switching manifold hampered progress. This powder was confirmed by XRD to be $Mg(OH)_2$. The main problem was the premature reaction the TBOH and $(MeCp)_2Mg$.

To avoid this strong pre-reaction, a dual inlet reactor tube (side by side) (figure 2) was tested. In this reactor a flat susceptor (2x2 cm) was used. No efficient MgO deposition was achieved, although a thin film was observed on the substrate. All oxidants (O_2, NO and TBOH) yielded similar results. Figure 3 shows deposition on Si (100) substrate of "MgO" at a substrate temperature of 380 ˚C. Flow patterns arising from thickness variation can be seen. No MgO peak was detected b XRD. The deposition appeared to be amorphous.

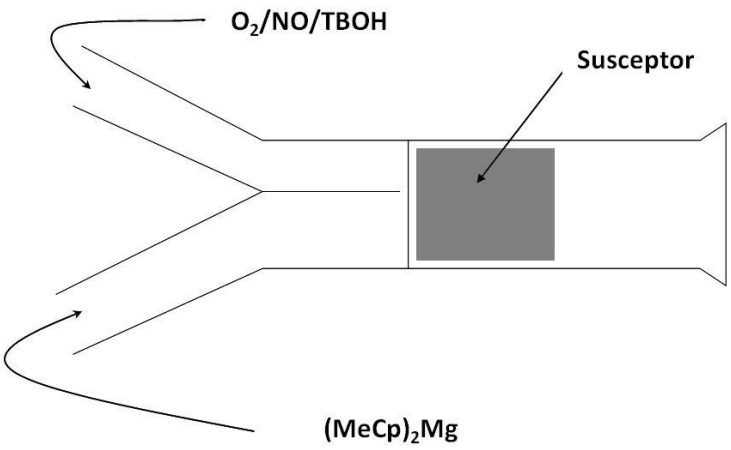

Figure 2 Schematic top view of two inlet reactor (side by side)

Using another reactor (illustrated in figure 4), similar results were obtained as with the reactor in figure 2. However, this reactor yielded improved growth rate of ZnO thin films. This was ascribed to a reduction in premature reactions and the use of an inclined susceptor.

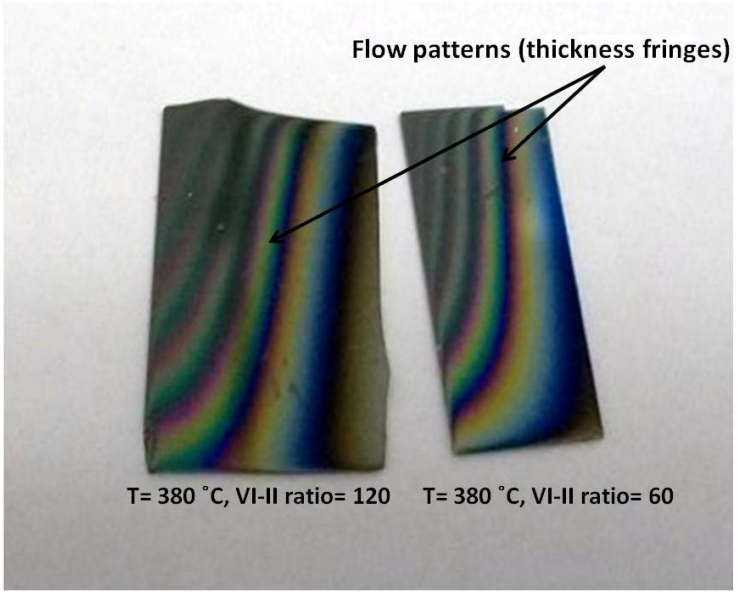

Figure 3 Deposition of MgO on Si (100) substrate using the two inlet reactor tube in figure 2

Final configuration

First, the Mg line temperature was fixed at 60 ˚C, resistive heaters were placed on the needle valve and the 3 way pneumatic valves on the Mg bubbler in order to unsure proper heating of compounds which might be cold spots due to their large thermal mass.

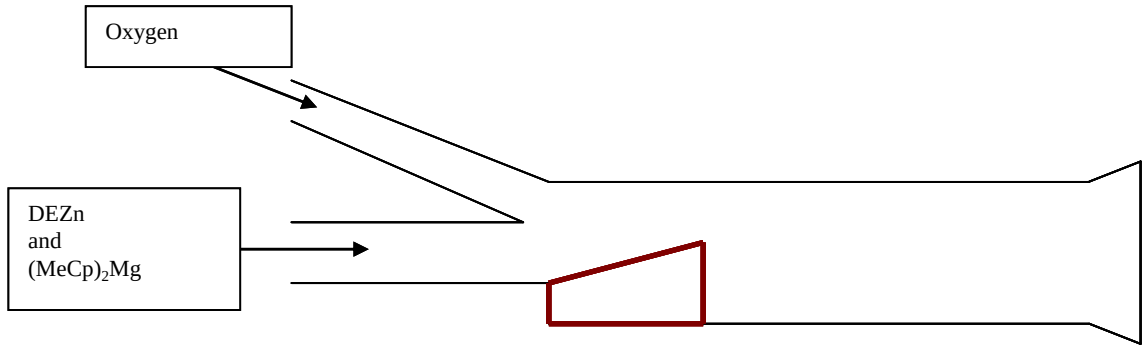

Figure 4 Schematic of the two inlet reactor tube (inlet on top)

Secondly, the fast switching manifold was removed. DEZn line and $(MgCp)_2Mg$ line were fitted with manual valves just upstream from the reactor tube. These valves were also heated resistively.

Thirdly, the reactor pressure was reduced from 250 to 20 Torr. This is believed to be the most important factor that contributed to the Mg incorporation into ZnO. In fact from various publications it found $(MgCp)_2Mg$ used at very low pressure, the highest were 6 Torr.

Fourthly, the growth of MgO using $(MgCp)_2Mg$ and any others oxidant is almost impossible at high pressure. The presence of DEZn contributes strongly to the incorporation of Mg in ZnO, which act as catalyst for $(MgCp)_2Mg$.

Figure 5 shows the configuration under which the growth of $Mg_xZn_{1-x}O$ was possible screening the resistive heaters, manual valves and the decrease in pressure from 250 Torr to 20 Tor of the reactor pressure. This configuration has permitted 60% of Mg incorporation into ZnO. All samples grown in this thesis have performed under this configuration.

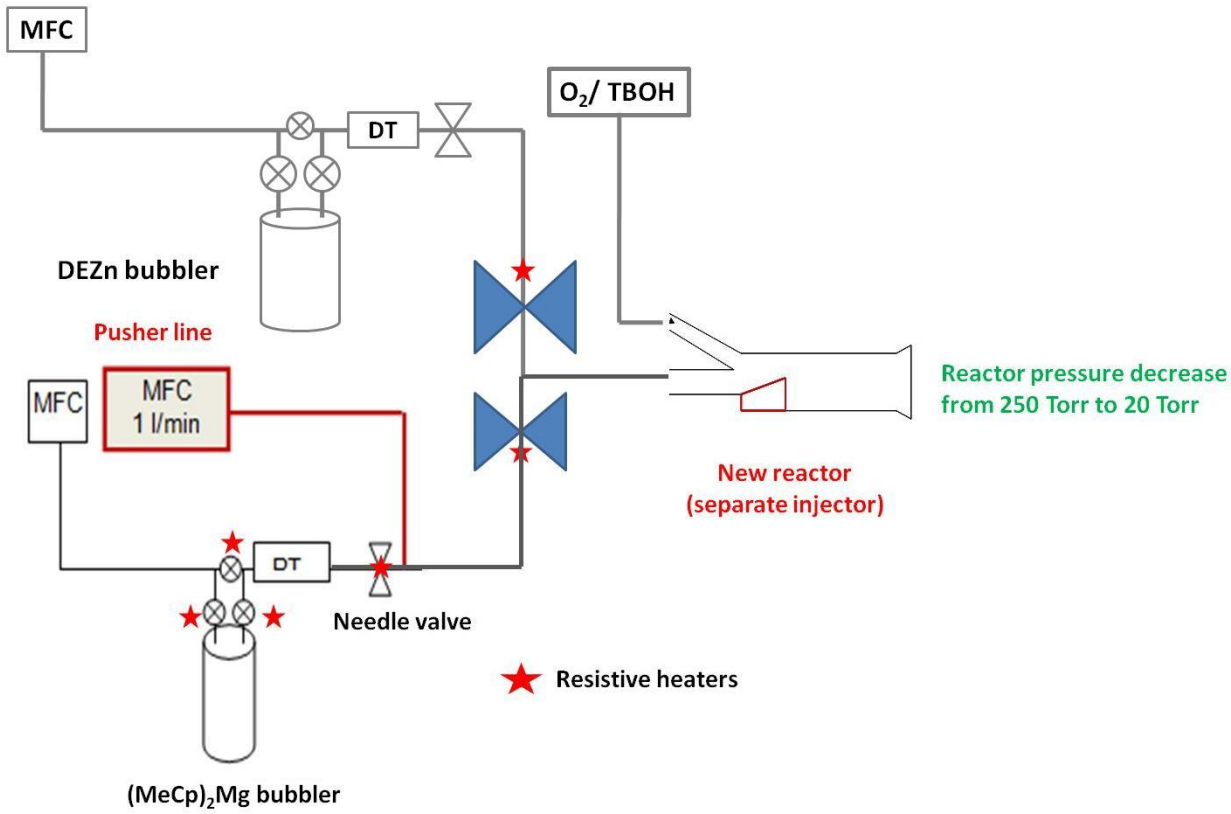

Figure 5 Current status of the Mg line on the MOCVD system

List of publications

"Effect of growth parameters on $Mg_xZn_{1-x}O$ films grown by metalorganic chemical vapour deposition" **K. Talla**, J. K. Dangbégnon, M. C. Wagener, J. R. Botha, Journal of Crystal Growth 315 (2011) 297–300

"ZnO grown by MOCVD: effect of substrate on optical and structural properties" **K. Talla**, J. K. Dangbégnon, M.C. Wagener and J.R. Botha, South African Institute of electrical engineers, Vol.101(1), Pages 37-41, 2010

"Effect of annealing and hydrogen plasma treatment on the luminescence of hydrothermally grown bulk ZnO" J.K. Dangbégnon, K**.** Talla, J.R. Botha, Optical Materials, In Press, Corrected Proof, Available online 12 January 2012

*"Effect of the annealing environment on the optical properties of ZnO/GaAs grown by MOCVD "*J.K. Dangbégnon, K**.** Talla, J.R. Botha, Journal of Luminescence, Volume 131, Issue 12, December 2011, Pages 2457-2462

"Thermal activation of nitrogen acceptors in ZnO thin films grown by MOCVD" J. K. Dangbégnon, **K. Talla**, J. R. Botha, Physica Status Solidi (c), Volume 7 Issue 6, Pages 1545–1549, 2010

"Metalorganic chemical vapor deposition of ZnO:N using NO as dopant" J.K. Dangbégnon, **K. Talla**, K.T. Roro and J.R. Botha, Physica B: Condensed Matter Volume 404, Issue 22, Pages 4419-4421, 2009

In preparation

"Study of $Mg_xZn_{1-x}O$ ($0 \leq x \leq 0.39$) films grown by metalorganic cchemical vapour deposition: structural and optical poperties" **K. Talla**, J. K. Dangbégnon, E. J. Olivier, J. H. Neethling, M. C. Wagener, H. C. Swart, J. Weber, J. R. Botha will be submitted in J. Appl. Phys.

Papers in peer-reviewed conference proceedings

"ZnO grown by Metal Organic Chemical Vapor Deposition: Effect of substrate on optical and structural properties" **K Talla**, JK Dangbegnon, MC Wagener, JR Botha, SMEOS Proceedings 2009, pp95-99 (ISBN 978-0-620-45648-7)

Contributions at international conferences / workshops

"Effect of growth rate and ZnO buffer layer on the structural and optical properties of MgZnO film" **K. Talla**, J. K. Dangbégnon, M. C. Wagener, J. R. Botha, 56th Annual conference of the SAIP, Pretoria, Unisa, 12-15 Jul 2011

"*Effect of growth temperature and annealing treatment on the activation of nitrogen in ZnO:N grown by MOCVD"* J. K. Dangbégnon, **K. Talla**, J. R. Botha, Int Conf on the Physics of Semiconductors, Seoul, South Korea, 25-30 July 2010

"Thermal activation of nitrogen acceptors in ZnO thin films grown by MOCVD" J.K. Dangbegnon, **K. Talla**, and J.R. Botha, 14th Int. Conf on II-VI Compounds, St Petersburg, Russia, Aug 2009

''ZnO grown by Metal Organic Chemical Vapor Deposition: effect of substrate on optical and structural properties'' **K. Talla**, J. K. Dangbegnon, M. C. Wagener and J. R. Botha, SMEOS 2009, Skukuza, 7-9 September 2009

"ZnO grown by Metal Organic Chemical Vapor Deposition: Comparison of Si(100), Si(111), csapphire, r-sapphire, glass, GaAs, ZnO as substrate" **K. Talla**, K. T. Roro, J. K. Dangbegnon, M. C. Wagener and J. R. Botha, 54th Annual conference of the SAIP, UKZN, Durban-Westville, July 2009

"Metalorganic Chemical Vapour Deposition of ZnO:N using NO as dopant" JK Dangbegnon, **K Talla**, KT Roro, A Venter, MC Wagener, JR Botha, Mabula Conference on Photonic Materials, Mabula Game Reserve, SA, 23-27 March 2009

References

[1] **G. Brauer, W. Anwand, W. Skorupa, J. Kuriplach, O. Melikhova, C. Moisson, H. von Wenckstern, M. Lorenz, and M. Grundmann.** 2006, Phys. Rev. B, Vol. 74, p. 045208.

[2] **Kaldis, E.** *In "Current Topics in Materials Science".* s.l. : North-Holland Publishing, 1981.

[3] **D. C. Look.** Mater. Sci. Eng. B, Vol. 802001, p. 383.

[4] **Jin, C.** *Growth and Characterization of ZnO and ZnO-Based Alloys $Mg_xZn_{1-x}O$ and $Mn_xZn_{1-x}O$.* Faculty of North Carolina State University. 2003. Thesis.

[5] **Ü. Özgür, Ya. I. Alivov, C. Liu, A. Teke, M. A. Reshchikov, S. Doğan,V. Avrutin, S. J. Cho, and H. Morkoç.** 2005, J. Appl. Phys., Vol. 98, p. 041301.

[6] **N. H. Nickel and E.Terukov.** *Zinc Oxide - A Material for Micro- and Optoelectronic Applications.* Dordrecht : Springer, 2005.

[7] **Y. S. Choi, J. W. Kang, D. K. Hwang, and S. J. Park.** 2010, IEEE transactions on electronics devices, Vol. 57, pp. 26-41.

[8] **E. V. Kalinina, A. E. Cherenkov, G. A. Onushkin, Ya. I. Alivov, D. C.Look, B. M. Ataev, A. K. Omaev, and C. M. Chukichev.** *ZnO/AlGaN ultraviolet light emitting diodes.* [book auth.] **N. H. Nickel and E. Terukov**. *Zinc Oxide as a Material for Micro- and Optoelectronic Applications.* s.l. : Springer, 2005, p. 216.

[9] **Y. I. Alivov, J. E. Van Nostrand, D. C. Look, M. V. Chukichev, and B. M. Ataev.** 2003, Appl. Phys. Lett., Vol. 83, p. 2943.

[10] **Y. Ryu, T. S. Lee, J. A. Lubguban, H. W. White, B. J. Kim, Y. S. Park, and C. J. Youn.** 2006, Appl. Phys. Lett., Vol. 88, p. 241108.

[11] **S. F. Dinga, G. H. Fana, S. T. Lia, K. Chena, and B. Xiao.** 2007, Physica B, Vol. 394, pp. 127-131.

[12] **J. M. Khoshman, D. C. Ingram, and M. E. Kordesch.** 2008, App. Phys. Lett., Vol. 92, p. 091902.

[13] **S. Shigemori, A. Nakamura, J. Ishihara, T. Aoki, and J. Temmyo.** 2004, Jpn. J. Appl. Phys, Vol. 43, pp. L1088-L1090.

[14] **K. Talla, J. K.Dangbegnon, M. C. Wagener, J. Weber, and J. R. Botha.** 2011, J. Cryst. Growth, Vol. 315, pp. 297–300.

[15] **A. Ohtomo, M. Kawasaki, Y. Sakurai, I. Ohkubo, R. Shiroki, Y. Yoshida, T. Yasuda, Y. Segawa, and H. Koinuma.** 1998, Mat. Sci. Eng. B, Vol. 56, pp. 263-266.

[16] **A. Ashrafi and Y. Segawa.** 2008, J. Appl. Phys., Vol. 104, p. 123528.

[17] **Y. R. Ryu, T. S. Lee, J. A. Lubguban, A. B. Corman, H. W. White, J. H.Leem, M. S. Han, Y. S. Park, C. J. Youn, and W. J. Kim.** 2006, Appl. Phys. Lett., Vol. 88, p. 052103.

[18] **P. Sharma, S. Johri, and S. Shukla.** 2000, J. Appl. Toxicol., Vol. 20, p. 313.

[19] **C. Yang, X. M. Li, Y. F. Gu, W. D. Yu, X. D. Gao, and Y. W. Zhang.** 2008, Appl. Phys. Lett., Vol. 93, p. 112114.

[20] **A. Schleife, M. Eisenacher, C. Rödl, F. Fuchs, J. Furthmüller, and F. Bechstedt.** 2010, Phys. Rev. B, Vol. 81, p. 245210.

[21] **T. Makino, Y. Segawa, M. Kawasaki, A. Ohtomo, R. Shiroki, K. Tamura, T. Yasuda, and H. Koinuma.** 2001, Appl. Phys. Lett., Vol. 78, p. 1237.

[22] **A. Ohtomo, R. Shiroki, I. Ohkubo, H. Koinuma, and M. Kawasaki.** 1999, Appl. Phys. Lett., Vol. 75, p. 4088.

[23] **B. P. Zhang, N. T. Bihn, K. Wakatsuki, C. Y. Liu, Y. Segawa, and N. Usami.** 2005, Appl. Phys. Lett., Vol. 86, p. 032105.

[24] **M. Lange, C. P. Dietrich, C. Czekalla, J. Zippel, G. Benndorf, M. Lorenz, J. Zúñiga-Pérez, and M. Grundmann.** 2010, J. Appl. Phys., Vol. 107, p. 093530.

[25] **F. Bertram and J. Christen.** 2006, Acta Phys. Pol. A, Vol. 110, pp. 103-110.

[26] **C. Klingshirn.** 2007, Phys. Stat. Sol. B, Vol. 244, pp. 3027–3073.

[27] **I. V. Maznichenko, A. Ernst, M. Bouhassoune, J. Henk, M. Däne, M. Lüders, P. Bruno, W. Hergert, I. Mertig, Z. Szotek, and W. M. Temmerman.** 2009, Phys. Rev. B, Vol. 80, p. 144101.

[28] **S. Muthukumar, J. Zhong, Y. Chen, T. Siegrist, and Y. Lu.** 2003, Appl. Phys. Lett., Vol. 85, p. 742.

[29] **M. Jaros.** 1985, Rep. Prog. Phys., Vol. 48, pp. 1091-1154.

[30] **W. Walukiewicz.** 1996, J. Cryst. Growth, Vol. 159, pp. 244-247.

[31] **K. T. Roro, G. H. Kassier, J. K. Dangbegnon, S. Sivaraya, J. E. Westraadt, J. H. Neethling, A. W. R. Leitch, and J. R. Botha.** 2008, Semicond. Sci. Technol., Vol. 23, p. 055021.

[32] **S. Choopun, R. D. Vispute, W. Noch, A. Balsamo, R. P. Sharma, T. Venkatesan, A. Lliadis, and D. C. Look,.** 1999, Appl. Phys. Lett., Vol. 75, p. 3947.

[33] **S. Li, F. X. Wang, G. Fu, Y. J. Ji, and J. Qi. Zhao.** 2010, Vols. 663-665, pp. 215-218.

[34] **A. J. C. Fiddes, K. Durose, A. W. Brinkman, J. Woods, P. D. Coates, and A. J. Banister.** 1996, J. Cryst. Growth, Vol. 159, p. 210.

[35] **Z. Yan, X. Zhang, Y. Liu, X. Zhou, and J. Liang.** 2011, J. Mater. Sci., Vol. 46, pp. 2392-2396.

[36] **S. Julia, B. Yuliarto, and Nugraha.** 2010, AIP conf. Proc., Vol. 1284, pp. 102-108.

[37] **P. Fons, K. Iwata, S. Niki, A. Yamada, and K. Matsubara.** 1999, J. Cryst. Growth, Vols. 201-202, p. 627.

[38] **H. Kashani.** 1998, J. Electron. Mater., Vol. 27, p. 876.

[39] **B. Y. Oh, Y. H. Kim, H. J. Lee, B. Y. Kim, H. G. Park, J. WooHan, G. S. Heo, T. W. Kim, K. Y. Kim, and D. S. Seo.** 2011, Semicond. Sci. Technol., Vol. 26, p. 085007.

[40] **A. K. Sharma, J. Narayan, J. F. Muth, C. W. Teng, C. Jin, A. Kvit, R. M. Kolbas, and O. W. Holland.** 1999, App. Phys. Lett., Vol. 75, p. 3327.

[41] **T. Minemoto, T. Negami, S. Nishiwaki, H. Takakru, and Y. Hamakawa.** 2000, thin Solid Fiilms, Vol. 372, pp. 173-176.

[42] **G. Shukla.** 2009, J. Phys. D: Appl. Phys., Vol. 42, p. 075105.

[43] **S. Choopun, R. D. Vispute, W. Yang, R. P. Sharma, T. Venkatesan and H. Shen.** 2002, Appl. Phys. Lett., Vol. 80, p. 1529.

[44] **L. K. Wang, Z. G. Ju, J. Y. Zhnag, J. Zheng, D. Z. Shen, B. Yao, D. X. Zhao, Z. Z. Zhang, B. H. Li, and C. X. Shan.** 2009, Appl. Phys. Lett., Vol. 95, p. 131113.

[45] **S. S. Hullavarad, S. Dhar, B. Varughese, I. Takeuchi, T. Venkatesan and R. D. Vispute.** 2005, J. Vac. Sci. Technol. A, Vol. 23, pp. 982-985.

[46] **Y. Chen, D. M. Bagnall, H. J. Koh, K. T. Park, K. Hiraga, Z. Q. Zhu, and T. Yao.** 1998, J. Appl. Phys., Vol. 84, p. 3912.

[47] **W. Y. Liang, and A. D. Yoffe.** 1968, Phys. Rev. Lett., Vol. 20, p. 59.

[48] **H. L. Hartnagel, A. L. Dawar, A. K. Jain, and C. Jagadish.** *Semiconducting transparent Thin Films*. Philadelphia : Institute of Physics Publishing, 1995.

[49] **Dangbegnon, J. K.** *Photoluminescence study of ZnO doped with nitrogen and arsenic.* Physics, Nelson Mandela Metropolitan University. 2010. Thesis

[50] **A. B. M. A. Ashrafi, I. Suemune, H. Kumano, and S. Tanaka.** 2002, Jpn. J. Appl. Phys., Vol. 41, pp. L1281-L1284.

[51] **Z. Y. Xiao, Y. C. liu, B. H. Li, J. Y. Zhang, D. X. Zhao, Y. M. Lu, D. Z. Shen, and X. W. Fan.** 2006, Semicond. Sci. Technol., Vol. 21, p. 1522.

[52] **M. L. Tu, Y. K. Su, and C. Y. Ma.** 2006, J. Appl. Phys., Vol. 100, p. 053705.

[53] **T. Terasako, S. Yura, S. Azuma, S. Shimomura, and S. Shirakata.** 2009, J. Vac. Sci. Technol. B, Vol. 27, p. 1609.

[54] **R. D. Vispute, S. S. Hullavard, D. E. Pugel, V. N. Kulkami, S. Dhar, I. Takeuchi, and T. Venkatesan.** *Wide band gap ZnO and $Mg_xZn_{1-x}O$ heterostructure for future optoelectronic devices.* Maryland : s.n., 2006.

[55] **S. C. Abrahams and J. L. Beinstein.** 1969, Acta Cryst., Vol. 25, p. 1233.

[56] **A. Janotti, and C. G. Van de Walle.** 2009, Rep. Prog. Phys., Vol. 72, p. 126501.

[57] **J. C. Phillips.** *Bonds and Bands in Semiconductors.* New York : Academic, 1973.

[58] **W. Glück.** 1970, Sol. Stat. Commun., Vol. 8, p. 1831.

[59] **B. K. Meyer, H. Alves, D. M. Hofmann, W. Kriegseis, D. Forster, F. Bertram, J. Christen, A. Hoffmann, M. Straßburg, M. Dworzak, U. Haboeck, and A. V. Rodina.** 2004, Phys. Stat. Sol. B, Vol. 241, pp. 231-260.

[60] **R. Dinges, D. Frohlich, B. Staginnus, and W. Staude.** 1970, Phys. Rev. B, Vol. 25, p. 922.

[61] **R. E. Dietz, J. J. Hopfield, and D. G. Thomas.** 1961, J. Appl. Phys., Vol. 32, p. 2282.

[62] **S. C. Jain, M. Willander, J. Narayan, and R. V. Overstraeten.** 2000, J. Appl. Phys., Vol. 87, p. 965.

[63] **B. P. Zhang, K. Wakatsuki, N. T. Binh, N. Usami, and Y. Segawa.** 2004, Thin Solid Films, Vol. 449, pp. 12-19.

[64] **J. Hu, H. Y. He, and B. C. Pan.** 2008, J. Appl. Phys., Vol. 103, p. 113706.

[65] **E. V. Lavrov, F. Herklotz, and J. Weber.** 2009, Phys. Rev. B, Vol. 79, p. 165210.

[66] **R. Triboulet, and J. Perriere.** 2003, Prog. Cryst. Growth Charac. Mat., Vol. 47, pp. 65-138.

[67] **O. F. Schirmer and D. Zwingel.** 1970, Solid State Commun., Vol. 8, p. 1559.

[68] **S. J. Pearton, D. P. Norton, K. I., Y. W. Heo, and T. Steiner.** 2005, Prog. Mater. Sci., Vol. 50, p. 293.

[69] **S. Limpijumnong, S. B. Zhang, S. H. Wei, and C. H. Park.** 2004, Phys. Rev. Lett., Vol. 92, p. 155504.

[70] **S. Limpijumnong, M. F. Smith, and S. B. Zhang.** 2006, Appl. Phys. Lett., Vol. 89, p. 222113.

[71] **T. Terasako, T. Yamanaka, S. Yura, M. Yagi, and S. Shirakata.** 2010, Thin Solid Films, Vol. 519, pp. 1546-1551.

[72] **S. Shionoya, and W. M. Yen.** *Phosphor Hood book.* [ed.] Boca Raton. Florida : CRC Press, 1999.

[73] **C. Jagadish and S. Pearton.** *Zinc Oxide Bulk, Thin Films and Nanostructures.* s.l. : Elsevier Limited, 2006.

[74] **T. Minami, H. Nanot, and S. Takata.** 1984, Jpn. J. Appl. Phys., Vol. 23, p. L280.

[75] **W. E. Bowen.** *Thin film electronic based on ZnO and ZnO/MgZnO heterojunctions.* Electrical Engineering, University of Michigan. 2010. Thesis.

[76] **H. D. Sun, T. Makino, Y. Segawa, M. Kawasaki, A. Ohtomo, K. Tamura, and H. Koinuma.** 2002, J. Appl. Phys., Vol. 91, p. 1993.

[77] **Y. Y. Kim, C. H. An, H. K. Cho, J. H. Kim, H. S. Lee, E. S. Jung, and H. S. Kim.** 2008, Thin Solid Films, Vol. 516, pp. 5602-5606.

[78] **D. J. Qiu, H. Z. Wu, N. B. Chen, and T. N. Xu.** 2003, Chin. Phys. Lett., Vol. 20, p. 582.

[79] **S. Raghavan, J. P. Hajra, G. N. K. Iycngar, and K. P. Abraham.** 1991, Thermochimica Acta, Vol. 189, pp. 151-158.

[80] **E. R. Segnit and A. R. Holland.** 1965, J. Am. Ceram. Sot., Vol. 49, p. 409.

[81] **Y. D. Kondrashev and Y. A. Omelelchenko.** 1964, Zh. Neog. Khim, Vol. 9, p. 937.

[82] **D. S. Kenny and A. Navrotsky.** 1972, J. Inorg. Nucl. Chem., Vol. 34, p. 2115.

[83] **J. F. Sarver, F. L. Katnack, and F. A. Hummel.** 1959, J. Electrochem. Soc., Vol. 106, p. 960.

[84] **C. H. Ahn, S. K. Mohanta, B. H. Kong, and H. K. Cho.** 2009, J. Phys. D: Appl. Phys., Vol. 42, p. 115106.

[85] **M. Wang, E. J. Kim, S. Kim, J. S. Chung, I-K. Yoo, E. W. Shin, S. H. Hahn, and C. Park.** 2008, Thin Solid Films, Vol. 516, pp. 1124-1129.

[86] **Y. Y. Kim, B. H. Kong, M. K. Choi, and H. K. Cho.** 2009, Mat. Sci. Eng. B, Vol. 165, pp. 80-84.

[87] **A. Y. Polyakov, N. B. Smirnov, A. V. Govorkov, E. A. Kozhukhova, A. I. Belogorokhov, H. S. Kim, D. P. Norton, and S. J. Pearton.** 2008, J. Appl. Phys., Vol. 103, p. 083704.

[88] **Z. Vashaei,T. Minegishi, H. Suzuki, T. Hanad, M. W. Cho, T. Yao, and A. Setiawan.** 2005, J. Appl. Phys., Vol. 98, p. 054911.

[89] **N. B. Chen, and C. H. Sui.** 2006, Mat. Sci. Eng., Vol. 126, pp. 16-21.

[90] **S. Limpijumnong and W. R. L. Lambrecht.** 2001, Phys. Rev. B, Vol. 63.

[91] **Saraf, G.** *Studies of in plane anisotropic physical properties in a-plane MgZnO.* Graduate School-New Brunswick Rutgers, The State University of New Jersey. 2008. Thesis.

[92] **J. W. Chiou, H. M. Tsai, C. W. Pao, F. Z. Chien, W. F. Pong, C. W. Chen, M.-H. Tsai, J. J. Wu, C. H. Ko, H. H. Chiang, H.-J. Lin, J. F. Lee, and J.-H. Guo.** 104, 2008, J. Appl. Phys., p. 013709.

[93] **W. I. Park, G. C. Yi, and H. M. Jang.** 2001, Appl. Phys. Lett., Vol. 79, p. 2022.

[94] **T. Minemoto, T. Negami, S. Nishiwaki, H. Takakura, and Y. Hamakawa.** 2000, Thin Solid Films, Vol. 173, p. 372.

[95] **C. Y. Liu, B. P. Zhang, N. T. Binh, K. Wakatsuki, and Y. Segawa.** 2005, J. Lumin., Vol. 112, pp. 186-190.

[96] **C. C. Wu, D.S. Wuu, P. R. Lin, T. N. Chen, R. H. Horng, S. L. Ou, Y. L. Tu, C. C. Wei, and Z. C. Feng.** 2011, Thin Solid Films, Vol. 519, pp. 1966-1970.

[97] **C. Jin, and R. J. Narayan.** 2006, J. Elect. Mat., Vol. 35, pp. 869-876.

[98] **Y. F. Li, B. Yao, Y. M. Lu, Z. P. Wei, Y. Q. Gai, C. J. Zheng, Z. Z. Zhang, B. H. Li, D. Z. Shen, Z. K. Tang, and X. W. Fan.** 2007, Appl. Phys. Lett., Vol. 91, p. 232115.

[99] **Y. W. Heo, Y. W. Kwon, Y. Li, S. J. Pearton, and D. P. Norton.** 2004, Appl. Phys. Lett., Vol. 84, p. 3474.

[100] **X. Zhang, X. M. Li, T. L. Chen, C. Y. Zhang, and W. D. Yu.** 2005, Appl. Phys. Lett., Vol. 87, p. 092101.

[101] **Y. Q. Gai, B. Yao, Z. P. Wei, Y. F. Li, Y. M. Lu, D. Z. Shen, J. Y. Zhang, D. X. Zhao, X. W. Fan, Jingbo Li, and J. B. Xia.** 2008, Appl. Phys. Lett., Vol. 92, p. 062110.

[102] **Z. P. Wei, B. Yao, Z. Z. Zhang, Y. M. Lu, D. Z. Shen, B. H. Li, X. H. Wang, J. Y. Zhang, D. X. Zhao, Z. K. Tang, and X. W. Fan.** 2006, Appl. Phys. Lett., Vol. 89, p. 102104.

[103] **J. Liang, H.Z. Wu, Y.F. Lao, D.J. Qiu, N.B. Chen, and T.N. Xu.** 2004, Chin. Phys. Lett., Vol. 21, p. 1135.

[104] **Manasevit, H. M.** 1968, Appl. Phys. Lett., Vol. 12, pp. 156–159.

[105] **A. C. Jones and M. L. Hitchman.** *Chemical vapor Deposition Precursors, Process and Application.* Cambridge : Royal Society of Chemistry, 2009. p. 313. 978-0-85404-465-8.

106] **J. Dai, H.Su, Li Wang, Y. Pu, W. Fang, and F. Jiang.** 2006, J. Cryst. Growth, Vol. 290, pp. 426-430.

[107] **Stringfellow, G. B.** *Organometallic Vapor-Phase Epitaxy: Theory and Practice.* San Diego : Academic Press, Inc., 1989.

[108] **C. Li, F. Y. Meng, S. Zhang, and J. Q. Wang.** 2010, J. Cryst. Growth, Vol. 312, pp. 1929–1934.

[109] **F. Y. Meng, Y. Chiba, A. Yamada, and M. Konagai.** 2007, Solar Ener. Mat. Solar Cells, Vol. 91, pp. 1887-1891.

[110] **C. Y. Liu, Y. C. Liu, B. P. Zhang, and R. Mu.** 2006, Phys. Stat. Sol. C, Vol. 3, pp. 3508–3511.

[111] **P. Kuznetsov, V. Lusanov, G. Yakushcheva, V. Jitov, L. Zakharov, I. Kotelyanskii, and V. Kozlovsky.**2010, Mat. Sci. Eng., Vol. 8, p. 012040.

[112] **Maury, F.** 1995, J. Phys. IV, Vol. 5, pp. 449-463.

[113] **A. Yamada and M. Konagai.** 1999, Solid Stat. Phenom., Vol. 67, p. 237.

[114] **P. Y. Lin, J. R. Gong, P. C. Li, T. Y. Lin, D. Y. Lyu, D. Y. Lin, H. J. Lin, T. C. Li, K. J. Chang, and W. J. Lin.** 2008, J. Cryst. Growth, Vol. 310, pp. 3024– 3028.

[115] **B. Vogele, C. Morhain, B. Urbaszek, S.A. Telfer, K.A. Prior, B.C. Cavenett.** 1999, J. Cryst. Growth, Vols. 201-202, pp. 950-953.

[116] **M. T. Litz, K. Watanabe, M. Korn, H. Ress, U. Lunz, W. Ossau, A. Waag, G. Landwehr, T. Walter, B. Neubauer, D. Gerthsen, and U. Schiissler.** 1996, J. Cryst. Growth, Vol. 159, pp. 54-57.

[117] **T. Shiozaki, T. Yamamoto, M. Yagi, and A. Kawabata.** 1981, Appl. Phys. Lett., Vol. 39, p. 399.

[118] **T. M. Barnes, J. Leaf, C. Fry, and C. A. Wolden.** 2005, J. Cryst. Growth, Vol. 274, pp. 412–417.

[119] **S. W. Xue, X. T. Zu, W. L. Zhou, H. X. Deng, X. Xiang, L. Zhang, and H. Deng.** 2008, J. All. Comp., Vol. 448, pp. 21-26.

[120] **L. K. Wang, Z.G. Ju, C. X. Shan, J. Zheng, D. Z. Shen, B. Yao, D. X. Zhao, Z. Z. Zhang, B. H. Li, and J. Y. Zhang.** 2009, Sol. Stat. Comm., Vol. 149, pp. 2021-2023.

[121] **K. Yamamoto, K. Enomoto, A. Nakamura, T. Aoki, and J. Temmyo.** 2007, J. Cryst. Growth, Vol. 298, pp. 468–471.

[122] **J. Ye, S. Gu, S. Zhu, S. Liu, W. Liu, X. Zhou,L. Hu, R. Zhang, Y. Shi, and Y. Zheng.** 2005, J. Cryst. Growth, Vol. 274, pp. 489–494.

[123] **Roro, K. T.** *MOCVD growth and characterization of ZnO thin films.* Physics, Nelson Mandela Metropolitan University. 2008.Thesis

[124] **S. Shirakata, K. Saeki, and T. Terasako.** 2002, J. Cryst. Growth, Vols. 237–239, pp. 528-532.

[125] **C. Thiandoume, V. Sallet, R. Triboulet, and O. Gorochov.** 2009, J. Cryst. Growth, Vol. 311, pp. 1411-1415.

[126] **O. Pagni, G. R. James, and A. W. R. Leitch.** 2004, Phys. Stat. Sol. C, Vol. 1, pp. 864-867.

[127] **W. Xu, Z. Ye, T. Zhou, B. Zhao, and L. Zhu.** 2004, J. Cryst. Growth, Vol. 265, pp. 133-136.

[128] **J. Zhu, R. Yao, H. Song, Z. Fu, A. Y. Kuznetsov, and I. H. Lee.** 2008, J. Vac. Sci. Technol. A, Vol. 26, pp. 224-227.

[129] **T. Gruber, C. Kirchner, and A. Waag.** 2002, Phys. Stat. Sol. B, Vol. 229, pp. 841-844.

[130] **C. Blaauw, R. A. Bruce, C. J. Miner, A. J. Howard, B. Emmerstorfer and A. J. Springthorpe.** 1989, J. Elect. Mat., Vol. 18, pp. 567-572.

[131] **L. Eckey, U. Von Gfug, J. Holst, A. Hoffmann, B. Schineller, K. Heime, M. heuken, O. Schon, and R. Beccard.** 1998, J. Cryst. Growth, Vols. 189-190, pp. 523-527.

[132] **A. V. Pogrebnyakov, X. X. Xi, J. M. Redwing, V. Vaithyanathan, D. G. Schlom, A. Soukiassian, S. B. Mi, C. L. Jia, J. E. Giencke, C. B. Eom, J. Chen, Y. F. Hu, Y. Cui, and Q. Li.** 2004, Appl. Phys. Lett., Vol. 85, pp. 2017-2019.

[133] **L. Konczewicz, P. Bigenwald, T. Cloitre, M. Chibane, R. Ricou, P. Testud, O. Briot, and R.L. Aulombard.** 1996, J. Cryst. Growth, Vol. 159, pp. 117-120.

[134] **G. Carta, N. El Habra, L. Crociani, G. Rossetto, P. Zanella, A. Zanella, G. Paolucci, D. Barreca, and E. Tondello.** 2007, Chem. Vap. Deposition, Vol. 13, pp. 185-189.

[135] **G. Saraf, T. Siegrist, and Y. Lu.** 2009, J. Vac. Sci. Technol. B, Vol. 27, pp. 1620-1624.

[136] **S. Muthukumar, Y. Chen, J. Zhong, F. Cosandey, Y. Lu, and T. Siegrist.** 2004, J. Cryst. Growth, Vol. 261, pp. 316-323.

[137] **Z. Shi, D. Liu, X. Yan, Z. Gao, and S. Bai.** 2008, Microelectron. J., Vol. 1, pp. 1583-1586.

[138] **T. Gruber, C. Kirchner, R. Kling, F. Reuss, and A. Waag.** 2004, Appl. Phys. Lett., Vol. 84, p. 5359.

[139. **C. Thiandoume, A. Lusson, P. Galtier, and V. Sallet.** 2010, J. Cryst. Growth, Vol. 312, pp. 1529-1533.

[140] **J. Wang, V. Sallet, G. Amiri, J.-F. Rommeluère, A. Lusson, E. Rzepka, J. E. Lewis, P. Galtier, and O. Gorochov.** 2005, Phys. Stat. Sol. A, Vol. 202, pp. 1967-1972.

[141] **S. Agouram, J. A. B. Segura, and V. M. Sanjose.** 2007, Super. Microstr., Vol. 42, pp. 140-144.

[142] **K. H. Bang, D. K. Hwang, S. W. Lim, and J. M. Myoung.** 2003, J. Cryst. Growth, Vol. 250, p. 437.

[143] **C. G. Van de Walle.** 2001, Phys. Rev. Lett., Vol. 85, p. 1012.

[144] **C. Kirchner, Th. Gruber, F. Reuss, K. Thonke, A. Waag, Ch. Giessen, and M. Heuken.** 2003, J. Cryst. Growth, Vol. 248, p. 20.

[145] **Ohring, M.** The Materials science of Thin films. 1. London : Academic London, 1992.

[146] **B. H. Kong, D. C. Kim, S. K. Mohanta, and H. K. Cho.** 2010, Thin Solid Films, Vol. 518, pp. 2975-2979.

[147] **A. Kamata, H. Yoshida, S. Chichibu, and H. Nakanishi.** 1997, J. Cryst. Growth, Vol. 170, pp. 518-522.

[148] **M. Kumar, H. P. Modak, S. Hardikarb, and S.B. Krupanidhi.** 1997, Solid State Comm., Vol. 103, pp. 411-416.

[149] **J. A. Venables, G. D. T. Spiller, and M. Hanbucken.** 1984, Rep. Prog. Phys., Vol. 47, pp. 399-459.

[150] **J. Palisaitis, R. Vasiliauskas and G. Ferro.** 2008, Physics of Advanced Materials Winter School, pp. 1-16.

[151] **Markov, l. V.** *Crystal growth for beginners : fundamentals of nucleation, crystal growth, and epitaxy.* London : World Scientific Publishing Co. Pte. Ltd., 2003. 981-238-245-3.

[152] **Yacobi, B. G.** *Semiconductor Materials: An Introduction to Basic Principles.* 2003.

[153] **J. P. Kwok and H. S. Zheng.** 1993, Thin Solid Films, Vol. 232, p. 99.

[154] **A. Asadov, W. Gao, Z. Li, and M. Hodgson.** 2005, Thin Films Solid, Vol. 476, p. 201.

[155] **P. W. Hawkes and J. C. H. Spence.***Science of Microscopy.* New York : Springer, 2007. Vol. 1. 10: 0-387-25296-7.

[156] **Behera, J. K.** *Synthesis and Characterization of ZnO nano-particles.* physics, National Institute of Physics. 2005. Thesis.

[157] **L. Zhu, M. Zhi, Z. Ye, and B. Zhao.** 2006, Appl. Phys. Lett., Vol. 88, p. 113106.

[158] **Pankove, J. I.** *Optical Processes in Semiconductors.* New York : General Publishing Company, 1971.

[159] **R. Schmidt-Grund, A. Carstens, B. Rheinlander, D. Spermann, H. Hochmut, G. Zimmermann, M. Lorenz, M. Grundmann, C. M. Herzinger, and M. Schubert.** 2006, J. Appl. Phys., Vol. 99, p. 123701.

[160] **Klingshirn, C. F.** *Semiconductor optics.* Berlin : Springer, 1995.

[161] **L. Pavesi and M. Guzzi.** 1994, J. Appl. Phys., Vol. 75, pp. 4779- 4841.

[162] **A. Teke, U. Ozgur, S. Dogan, X. Gu, H. Morkac, B. Nemeth, J. Nause, and H. O. Everitt.** 2004, Phys. Rev. B, Vol. 70, p. 195207.

[163] **Schubert, E. F.** *Doping in III-V semiconductors.* Cambridge : University of Cambridge, 1993.

[164] **S. Agouram, J. Z. Perez, and V. M. Sanjose.** 2007, Appl. Phys. A, Vol. 88, pp. 83-87.

[165] **M. Nishio, K. Hayashida, Q. Guo, and H. Ogawa.** 2001, Appl. Surf. Sci., Vols. 169-170, pp. 227-230.

[166] **K. T. Roro, J. K. Dangbegnon, S. Sivaraya, A. W. R. Leitch, J. R. Botha.** 2008, J. Appl. Phys., Vol. 103, p. 53516.

[167] **J. Zhu, R. Yao, H. Song, Z. Fu, A. Y. Kuznetsov, and I. H. Lee.** 2008, J. Vac. Sci. Technol. A, Vol. 26, p. 224.

[168] **Y. J. Chen, Y. Y. Shih, C. H. Ho, J. H. Du, and Y. P. Fu.** 2010, Ceramics International, Vol. 36, pp. 69-73.

[169] **Y. J. Chen, Y. Y. Shih, C. H. Ho, J. H. Du, and Y. P. Fu.** 2009, Ceram. Inter., Vol. 36, pp. 69-73.

[170] **B. H. Kong, and H. K. Cho.** 2006, J. Cryst. Growth, Vol. 289, p. 370.

[171] **Y. J. Zeng, Z. Z. Ye, and W. Z. Xu.** 2005, Appl. Surf. Sci., Vol. 250, p. 280.

[172] **X. L. X. Wu, H. Cao, and R. P. H. Chang.** 2004, J. Appl. Phys., Vol. 95, p. 3141.

[173] **B. P. Zhang, N. T. Binh, Y. Segawa, Y. Kashiwaba, K. Haga.** 2004, Appl. Phys. Lett., Vol. 84, pp. 586-588.

[174] **B. K. Meyer, H. Alves, D. M. Hofmann, W. Kriegseis, D. Forster, F. Bertram, J. Christen, A. Hoffmann, M. Straßburg, M. Dworzak, U. Haboeck, and A. V. Rodina.** 2006, Mat. Sci. Eng. B, Vol. 127, pp. 280-284.

[175] **W. Hamby, D. A. Lucca, J. K. Lee, M. Nastasi, H. S. Kang, and S. Y. Lee.** 2006, Nuc. Instr. Method. Phys. Res., Vol. 249, pp. 196-199.

[176] **M. Schirra, R. Schneider, A. Reiser, G. M. Prinz, M. Feneberg, J. Biskupek, U. Kaiser, C. E. Krill, K. Thonke, and R. Sauer.** 2008, Phys. Rev. B, Vol. 77, p. 125215.

[177] **M. Schirra, R. Schneider, A. Reiser, G.M. Prinz, M. Feneberg, J. Biskupek, U. Kaiser, C.E. Krill, R. Sauer, and K. Thonke.** 2007, Physica B, Vols. 401-402, pp. 362-365.

[178] **A. L. Yadouni, A. Boudrioua, J. C. Loulergue, V. Sallet, and R. Triboulet.** 2005, Opt. Mat., Vol. 27, pp. 1391-1395.

[179] **Z. Fu, B. Lin, and J. Zu.** 2002, Thin Solid Films, Vol. 402, pp. 302-306.

[180] **K. H. Bang, D. K. Hwang, S. W. Lim, and J. M. Myoung.** 2003, J. Cryst. Growth, Vol. 210, pp. 177-182.

[181] **H. Liu, H. Qiu, X.i Chen, M. Yu, and M. Wang.** 2009, Cur. Appl. Phys., Vol. 9, pp. 1217-1222.

[182] **C. Munuera, J. Z. Perez, J. F. Rommeluere, V. Sallet, R. Triboulet, F. Soria, V. M. Sanjose, and C. Ocal.** 2004, J. Cryst. Growth, Vol. 264, pp. 70-78.

[183] **W. Göpel, J. Pollmann, I. Ivanov, and B. Reihl.** 1982, Phys. Rev. B, Vol. 26, p. 3144.

[184] **M. Losurdo, M. M. Giangregorio, A. Sacchetti, P. Capezzuto, G. Bruno, G. Malandrino, I. L. Fragala.** 2007, Super. Micro., Vol. 42, pp. 40-46.

[185] **X. Jiang, C. L. Jia, and R. J. Hong.** 2006, J. Cryst. Growth, Vol. 289, pp. 464-471.

[186] **Muthukumar, S.** *MOCVD growth and characterizations of $Mg_xZn_{1-x}O$ films on r-sapphire.* Rutgers University. 2003. thesis.

[187] **H. P. Sun and X. Q. Pan, X. L. Du, Z. X. Mei, Z. Q. Zeng, and Q. K. Xue.** 2004, Appl. Phys. Lett., pp. 4385-4387.

[188] **Drift, A. Van.** 1967, Philips Research Reports, Vol. 22, p. 267.

[189] **J. Sann, J. Stehr, A. Hofstaetter, D. M. Hofmann, A. Neumann, M. Lerch, U. Haboeck, A. Hoffmann, and C. Thomsen.** 2007, Phys. Rev B, Vol. 76, p. 195203.

[190] **W. J. Li, E. W. Shi, W. Z. Zhong, and Z. W. Yin.** 1999, J. Cryst. Growth, Vol. 203, pp. 186-196.

[191] **J. Chen, W. Z. Shen, N. B. Chen, D. J. Qiu, and H. Z. Wu.** 2003, J. Phys. Condens. Matter, Vol. 15, pp. L475-L482.

[192] **N. B. Chen, H. Z. Wu, D. J. Qiu, T. N. Xu, J. Chen, and W. Z. Shen.** 2004, J. Phys. Condens. Matter., Vol. 16, pp. 2973-2980.

[193] **Y. Matsumoto, M. Murakami, Z. Jin, A. Ohtomo, M. Lippmaa, M. Kawasaki, and H. Koimun.** 1999, Jpn. J. Appl. Phys., Vol. 38, p. L603.

[194] **Pierson, H. O.** *Handbook of chemical deposition (CVD) Principles, Technology, and Applications.* 2. s.l. : Noyes Publications / William Andrew Publishing, LLC, 1999. p. 53. 0-8155-1432-8.

[195] **S. Han, D. Z. Shen, J. Y. Zhang, Y. M. Zhao, D. Y. Jiang, Z. G. Ju, D. X. Zhao, and B. Yao.** 2010, Vacuum, Vol. 84, pp. 1149-1153.

[196] **H. Tampo, H. Shibata, K. Maejima, A. Yamada, K. Matsubara, P. Fons, S. Niki, T. Tainaka, Y. Chiba, and H. Kanie.** 2007, Appl. Phys. Lett., Vol. 91, p. 261907.

[197] **C. J. Pan, K. F. Lin, W. T. Hsu, and W. F. Hsieh.** 2007, J. Appl. Phys., Vol. 102, p. 123504.

[198] **Y. Ma, G. Du, J. Yin, T. Yang, and Y. Zhang.**2005, Semicond. Sci. Technol., Vol. 20, pp. 1198-1202.

[199] **A. B. M. A. Ashrafi, and Y. Segawa.** 2005, J. Vac. Sci. Technol. B, Vol. 23, pp. 2030-2033.

[200] **H. Li, X. Pan, M. Qiao, Y. Zhang, T. Wang, and E. Xie.** 2008, Vacuum, Vol. 82, pp. 459-462.

[201] **B. P. Zhang, B. L. Liu, J. Z. Yu, Q. M. Wang, C. Y. Liu, Y. C. Liu, and Y. Segawa.** 2007, Appl. Phys. Lett., Vol. 90, p. 123113.

[202] **X. Zhang, F. Herklotz, E. Hieckmann, P. Schmidt, and J. Weber.** 2011, J. Vac. Sci. Technol. A, Vol. 29, p. 03A107.

[203] **S. Heitsch, G. Zimmermann, D. Fritsch, C. Sturm, R. Schmidt-Grund, C. Schulz, H. Hochmuth, D. Spemann, G. Benndorf, B. Rheinländer, Th. Nobis, M. Lorenz, and M. Grundmann.** 2007, J. Appl. Phys., Vol. 101, p. 083521.

[204] **R. Singh, D. Doppalapudi, and T. D. Moustakas.** 1997, Appl. Phys. Lett., Vol. 90, p. 1089.

[205] **M. Grundmann and C. P. Dietrich.** 2009, J. Appl. Phys., Vol. 106, p. 123521.

[206] **C. Y. Zhao, X. H. Wang, J. Y. Zhang, Z. G. Ju, C. X. Shan, B. Yao, D. X. Zhao, D. Z. Shen, and X. W. Fan.** 2011, Thin Solid Films, Vol. 519, pp. 1976-1979.

[207] **T. A. Wassner, B. Laumer, S. Maier, A. Laufer, B. K. Meye, M. Stutzmann, and M. Eickhoff.** 2009, J. Appl. Phys., Vol. 105, p. 023505.

[208] **B. K. Sonawane, M. P. Bhole, and D. S. Patil.** 2009, Mat. Sci. Semicon. Proc., Vol. 41, pp. 17-26.

[209] **R. Ghosh, and D. Basak.** 2009, Appl. Surf. Sci., Vol. 255, pp. 7238-7242.

[210] **Mares, J. W.** *Epitaxial growth, charachterization and application of novel wide bandgap oxide semiconductors.* College of Optics / CREOL & FPCE, B.S. University of Central Florida. 2003. p. 84, thesis.

[211] **A. Muller, M. Stolzel, C. Dietrich, G. Benndorf, M. Lorenz, and M. Grundmann.** 2010, J. Appl. Phys., Vol. 107, p. 013704.

[212] **Z. Vashaei, T. Minegishi, H. Suzuki, M.W. Cho, and T. Yao.** 2006, Phys. Stat. Sol. C, Vol. 3, pp. 1042-1045.

[213] **C. H. Lei. G. V. Tendeloo, J. G. Lisoni, M. Siegert, and J. Schubert.** 2001, J. Cryst. Growth, Vol. 226, pp. 419-429.

[214] **H. Matsui, H.Tabata, N. Hasuike and H. Harima.** 2006, J. Appl. Phys., Vol. 99, p. 024902.

[215] **M. Shimizu, Y. Kawaguchi, K. Hiramatsu, and N. Sawaki,.** 1997, Jpn. J. Appl. Phys., Vol. 36, p. 3381.

[216] **V. Srikant, and D. R. Clarke.** 1997, J. Appl. Phys., Vol. 81, pp. 6357-6364.

[217] **J. F. Rommeluere, L. Svob, F. Jomard, J. Mimila-arroyo, A. Lusson, V. Sallet, and Y. Marfaing.** 2003, Appl. Phys. Lett., Vol. 83, p. 287.

[218] **Madelung, O.** *Data in Science and Technology: Semiconductors.* Berlin : Springer, 1992.

[219] **F. Wang, D. Masugata, C. B. Oh, A. Omino, S. Seto, and M. Isshiki.** 2002, Phys. Stat. Sol. A, Vol. 193, p. 251.

[220] **M. Bosi, and R. Fornari.** 2004, J. Cryst. Growth, Vol. 265, pp. 434-439.

[221] **Yang, Z.** *Doping in ZnO thin films*. Electrical engineering, University of California Riverside. California : s.n., 2009. Theses.

[222] **K. Thonke, M. Schirra, R. Schneider, A. Reiser, G. M. Prinz, M. Feneberg, R. Sauer, J. Biskupek, and U. Kaiser.** 2010, Phys. Stat. Sol. B, Vol. 247, pp. 1464–1468.

[223] **X. H. Pan, W. Guo, Z. Z. ye, B. Liu, Y. Che, W. Tian, D. G. Schlom, and X. Q. Pan.** 2009, Appl. Phys. Lett., Vol. 95, p. 152105.

[224] **C. X. Shan, Z. Liu, and S. K. Hark.** 2008, Appl. Phys. Lett., Vol. 92, p. 073103.

[225] **X. Chen and J. Kang.** 2008, Semicond. Sci. Technol., Vol. 23, p. 025008.

[225] **C. P. Dietrich, M. Lange, G. Benndorf, J. Lenzner, M. Lorentz, and M. Grundmann.** 2010, New J. Phys., Vol. 12, p. 033030.

[226] **A. L. Yang, H. P. Song, D. C. Liang, H. Y. Wei, X. L. Liu, P. Jin, X. B. Qin, S. Y. Yang, Q. S. Zhu, and Z. G. Wang.** 2010, Appl. Phys. Lett., Vol. 96, p. 1519044.

[227] **K. Yamamoto, T. Tsuboi, T. Ohashi, T. Tawara, H. Gotoh, A. Nakamura, and J. Temmyo.** 2010, J. Cryst. Growth, Vol. 312, pp. 1703-1708.

[228] **A. Bell, S. Srinivasan, C. Plumlee, H. Omiya, F. A. Ponce, J. Christen, S. Tanaka, A. Fujioka and Y. Nakagawa.** 2004, J. Appl. Phys., Vol. 95, p. 4670.

[229] **J. D. Ye, K. W. Teoh, X. W. Sun, G.. Q. Lo, D. L. Kwong, H. Zhao, S. L. Gu, R. Zhang, Y. D. Zheng, S. A. Oh, X. H. Zhang, and S. Tripathy.** 2007, Appl. Phys. Rev., Vol. 91, p. 091901.

[230] **E. F. Schubert, E. O. Gobel, Y. Horikoshi, K. Ploog, and H. J. Queisser.** 1984, Phys. Rev. B, Vol. 30, p. 813.

[231] **R. Zimmermann.** 1990, J. Cryst. Growth, Vol. 101, p. 346.

[232] **W. Shan, W. Walukiewicz, E. E. Haller, B. D. Little, J. J. Song, M. D. McCluskey, N. M. johnson, Z. C. Feng, and R. A. Stall.** 1998, J. Appl. Phys., Vol. 84, p. 4452.

[233] **M. Trunk, V. Venkatachalapathy, A. Galeckas, and A. Y. Kuzetsov.** 2010, Appl. Phys. Lett., Vol. 97, p. 211901.

[234] **T. M. Borseth, B. G. Svensson, A. Y. Kuznetsov, P. Klason, Q. X. Zhao, and M. Willander.** 2006, Appl. Phys. Lett., Vol. 89, p. 262112.

[235] **Oleyik, N.** *MOVPE Growth and Characterization of ZnO Properties for Optoelectronic Applications.* Univ. Maddeburg, Institut fur Experimentelle Physik. 2007. Thesis.

[236] **A. Lusson, N. Hanèche, C. Thiandoume, V. Sallet, and P. Galtier.** 2009, J. Vac. Sci. Technol. B, Vol. 23, pp. 1755-1759.

[237] **D. C. Kim, B.H. Kong, S. K. Mohanta, and H. K. Cho.** 2010, Thin Solid Films, Vol. 518, pp. 2975-2979.

[238] **M. R. Leys, H. Titze, L. Samuelson, and J. Petruzzello.** 1988, J. Cryst. Growth, Vol. 93, p. 504.

[239] **J. Ou, W. K. Chhen, H. C. Lin, Y. C. Pan and M. C. Lee.** 1998, Jnp. J. Appl. Phys., Vol. 37, pp. L633-L636.

[240] **H. Tanaka, S. Fujita, and Sh. Fujita.** 2005, Appl. Phys. Lett., Vol. 86, p. 192911.

[241] **K. Hiramatsu, S. Itoh, H. Amano, I. Akasaki, N. Kuwano, T. Shiraishi, and K. Oki.** 1991, J. Cryst. Growth, Vol. 115, p. 628.

[242] **T. Takagi, H. Tanaka, S. Fujita, and S. Fujita.** 2003, Jpn. J. Appl. Phys., Vol. 42, pp. L401-L403.

[243] **S. Fujita, T. Takagi, H. Tanaka, and S. Fujita.** 2004, Phys. Stat. Sol. B, Vol. 241, pp. 599-602.

[244] **L.F. Bian, D.S. Jiang, and S.L. Lu.** 2003, J. Cryst. Growth, Vol. 253, pp. 155–160.

[245] **Z. G. Ju, C. X. Shan, C. L. Yang, J. Y. Zhang, B. Yao, D. X. Zhao, D. Z. Shen, and X. W. Fan.** 2009, Appl. Phys. Lett., Vol. 94, p. 101902.

[246] **Y. Y. Kim, C. H. An, H. K. cho, J. H. Kim, H. S. Lee, E. S. Jung, and H. S. Kim.** 2008, Thin Solid Films, Vol. 516, pp. 5602-5606.

[247] **X. Zhang, H. Ma, J. Ma, F. Zong, H. Xiao, and F. Ji.** 2005, Physica B, Vol. 357, pp. 428-432.

[248] **W. Liu, B. Yao, Y. Li, B. Li, C. Zheng, B. Zhang, C. Shan, Z. Zhang, J. Zhang, and D. Shen.** 2009, Appl. Surf. Sci., Vol. 255, pp. 6745-6749.

[249] **K. Thonke, M. Schirra, R. Schneider, A. Reiser, G. M. Prinz, M. Feneberg, R. Sauer, J. Biskupek, and U. Kaiser.** 2010, Phys. Stat. Sol. B, Vol. 247, pp. 1464–1468.

[250] **D. Y. Jiang, D. Z. Shen, K. W. Liu, C. X. Shan, Y. M. Zhao, T. Yang, B. Yao, Y. M. Lu, and J. Y. Zhang.** 2008, Semicond. Sci. Technol., Vol. 23, p. 035002.

[251] **S. Yang, B. H. Lin, W. R. Liu, J. H. Li, C. S. Chang, C. H. Hsu, and W. F. Hsieh.** 2009, Cryst. Growth Des., Vol. 9, pp. 5184–5189.

[252] **H. Von Wenckstern, H. Schmidt, M. Grundmann, M. W. Allen, P. Miller, R. J. Reeves, and S. M. Durbin.** 2007, Appl. Phys. Lett., Vol. 91.

[253] **H. Schrey, and C. Klingshrin.** 1980, Solid Stat. Commun., Vol. 33, pp. 485-488.

[254] **M. A. Reshchikov, V. Avrutin, N. Izyumskaya, R. Shimada, H. Morkoç, and S. W. Novak.** 2009, J. Vac. Sci. Technol. B, Vol. 23, pp. 1749-1754.

[255] **R. Dingle.** 1969, Phys. Rev. Lett., Vol. 23, p. 579.

[256] **Y. G. Wang, S. P. Lau, X. H. Zhang, H. W. Lee, S. F. Yu, B. K. Tay, and H. H. Hang.** 2003, Chem. Phys. Lett., Vol. 375, pp. 113-118.